Fall 12-2022

Evaluation of Swelling Pressure and Shear Strength of Inorganic Microfiber-Reinforced Bentonite for the Engineered Barrier System

Jose Maria Ferdinand Victoria Calaunan
University of Nebraska-Lincoln, calaunan.ferdinand@gmail.com

EVALUATION OF SWELLING PRESSURE AND SHEAR STRENGTH OF INORGANIC MICROFIBER-REINFORCED BENTONITE FOR THE ENGINEERED BARRIER SYSTEM

by

Jose Maria Ferdinand V. Calaunan

A THESIS

Presented to the Faculty of

The Graduate College at the University of Nebraska

In Partial Fulfillment of Requirements

For the Degree of Master of Science

Major: Civil Engineering

Under the Supervision of Professors Jongwan Eun and Seunghee Kim

Lincoln, Nebraska

December, 2022

EVALUATION OF SWELLING PRESSURE AND SHEAR STRENGTH OF INORGANIC MICROFIBER-REINFORCED BENTONITE FOR THE ENGINEERED BARRIER SYSTEM

Jose Maria Ferdinand V. Calaunan, M.S.

University of Nebraska, 2022

Advisors: Jongwan Eun and Seunghee Kim

Nowadays, the permanent disposal of high-level radioactive waste materials has been a primary concern in several countries. The deep geological repository, being the preferred disposal method across the globe, utilizes a network of engineered barriers to prevent the radioactive material from spreading throughout the facility and harming the natural environment. Part of this engineered barrier system (EBS) is the buffer material, which essential function is holding the radioactive waste-containing canister in place. However, the potential generation of desiccation cracks in this buffer material is imminent due to the heat emitted from the radioactive waste. Knowing the capability of inorganic fibers to help mitigate such a situation, glass microfiber is proposed as a reinforcement material to bentonite, owing to its high heat resistance. This research aims to evaluate the effect of fiber content on bentonite in terms of swelling pressure and shear strength. Using the one-dimensional consolidation test setup, the swelling pressure test was conducted at both ambient and elevated temperatures to obtain the swelling pressure and compressibility characteristics of the inorganic-microfiber reinforced bentonite. Moreover, the shearing behavior of the bentonite sample was observed through the direct simple shear test. Lastly, the specimen's behavior under the critical state was predicted using the Modified Cam Clay

Model. The results obtained from this study would be a valuable tool for the baseline assessment of the effectiveness of the fiber reinforcement to potentially improve the engineering performance of the deep geological repository for the safe storage of high-level radioactive waste materials.

Keywords: Bentonite, fiber reinforcement, temperature elevation, swelling pressure, compressibility, shearing, Modified Cam Clay Model

ACKNOWLEDGMENTS

I would like to express my deepest gratitude to my dearest advisors, Dr. Jongwan Eun and Dr. Seunghee Kim, for their continuous guidance and patience during my graduate studies. Without their unwavering support, I would not have been able to finish this remarkable academic journey.

I am also extremely grateful to my thesis committee members, Dr. Jiong Hu and Dr. Jamilla Teixeira, for their insightful comments and invaluable feedback. I would also like to thank Dr. Yong-Rak Kim for providing his inputs as a co-principal investigator of this project. Likewise, I am grateful to the members of the Texas A&M University (Julia Grasley and Mohammad Rahmani) and Sandia National Laboratories (Dr. Carlos Jove-Colon, Dr. Yifeng Wang, and Amanda Sanchez) for contributing their ideas to improve this research.

I am very thankful to the members of the Geotechnical and Materials Engineering Research Group at the University of Nebraska–Lincoln: Dr. Yuan Feng, Dr. Sina Mousavi, Hung Van, Arafat Alam, Basil Abualshar, Yusuf Alhowaidi, Daniel Robertson, and Akbota Aitbayeva. These people have been my workmates turned to lifetime friends.

My heartfelt appreciation goes to Dr. Donghwa Noh, whom I have the pleasure of working with. Thank you for being my confidant, my number one supporter, and the best friend I could ever ask for. All the memories and experiences we shared together for the past two years will forever be treasured.

To my family, friends, and my dearest country, the Philippines, I hope this academic effort will make you proud. *Lagi't Lagi, Para sa Bayan.*

GRANT INFORMATION

This research is being performed using funding received from the U.S. Department of Energy (DOE) Office of Nuclear Energy's Nuclear Energy University Program (NEUP) (Grant ID: DE-NE0008954).

TABLE OF CONTENTS

LIST OF FIGURES

LIST OF TABLES

CHAPTER 1. INTRODUCTION

1.1 BACKGROUND OF THE STUDY

Bentonite has a high swelling capacity due to its high montmorillonite content and low hydraulic conductivity through water adsorption. Because of these benefits, bentonite has been used in many engineering applications, such as drilling fluid in the oil and gas sector (Abdou et al., 2013; Afolabi et al., 2017; Azeez et al., 2018) and barrier material for landfills (Dutta & Mishra, 2017; He et al., 2022; Kumar & Yong, 2002). Another potential application of the bentonite is for the deep geological disposal of high-level radioactive waste (HLRW) materials such as spent fuel (Organisation for Economic Co-operation and Development, 2003; World Nuclear Association, 2021), where it acts as a buffer material in the engineered barrier system (EBS). A typical buffer material between the canister and the host rock in the EBS is compacted bentonite (Sun et al., 2021). With the bentonite possessing low permeability, large swelling capacity, and retention properties (Villar & Lloret, 2008), these essential characteristics make the bentonite a suitable buffer material for the safe storage of HLRW (Sellin & Leupin, 2014).

However, recent studies have shown that the saturation of EBS in the HLRW repository can be a prolonged process due to the heat generation and thermo-osmosis from spent fuel (Villar et al., 2012; Sánchez et al., 2016). Associated with this slow saturation, heat-induced dry-out near the canister and subsequent generation of desiccation cracks in the buffer could lead to preferential pathways in the EBS. One of the methods to address these key issues is to add fibers in the bentonite as a mechanical reinforcement for soil. On the other hand, several types of organic and inorganic fiber reinforcement, including

polymers, minerals, glass, and synthetic materials, have been used to enhance clay properties in other geotechnical and geoenvironmental applications. These include utilizing sand-bentonite-carbon fiber mixtures as borehole backfilling material, polypropylene fiber with sand for the enhancement of bearing capacity, and polypropylene fiber and lime admixture for ground improvement (Joshi et al., 2004; Yetimoglu et al., 2005; Cai et al., 2006; Chaduvula et al., 2017; Liu et al., 2019). Although in saturated condition, desiccation cracks might not be present in the bentonite; hence, resulting mainly in the reduction of swelling pressure of the material. On another note, microfibers can increase the tensile force to improve the shear strength of the soil. Particularly, inorganic fibers such as glass, carbon, and basalt fibers are proven to be useful, especially for situations with exposure to high temperatures, due to their heat resistance (Ishikawa, 2014).

Swelling is one of the critical design parameters to be considered to generate excellent intact conditions between the buffer and host rock. Several authors studied the effect of fiber in varying lengths and content on the swelling pressure of bentonite. It showed that an increase in fiber content leads to a decrease in swelling pressure (Viswanadham et al., 2009; Phanikumar & Singla, 2016; Mukherjee & Mishra, 2019). In terms of its performance under high temperatures, it was found that elevating the temperature (25°, 50°, 70°, and 90°C) would cause an increase in the swelling pressure of the bentonite (Ye et al., 2013; Bag & Rabbani, 2017). Essentially, the swelling behavior with respect to the elevated temperature and fiber addition can be considered to be distinct from each other. However, there is a lack of studies associated with the combined effect of the fiber content and temperature elevation on the swelling characteristics and shearing behavior of bentonite for various applications such as grouting, geothermal heat exchange,

EBS, etc. With that, a more comprehensive study is needed to fill the knowledge gap in the swelling pressure and shear strength of such inorganic fiber-reinforced bentonite.

1.2 RESEARCH SIGNIFICANCE

The U.S. Environmental Protection Agency (2022a) states that fossil fuel contributes to 65% of the world's greenhouse gas emissions. However, nuclear energy translates to more than 50% of the national low-carbon electricity generation and 30% of the global low-carbon electricity (Hsu, 2021). Having this, nuclear energy gains traction because of its insignificant greenhouse gas emission during operation (International Atomic Energy Agency, 2020). Therefore, the national and global reliance on this energy source entails a vast amount of nuclear waste after production.

Along with this waste are the problem of its disposal and associated processes. Currently, deep geological disposal is the preferred method for high-level radioactive waste. Although its current design standards are still applicable, exploring a further improved engineered barrier system in this geological repository is the main driving force of this study.

1.3 THESIS OBJECTIVES

Bentonite is a standard buffer material for radioactive waste repositories. This conventional material is prevalent due to its swelling properties caused by the montmorillonite clay mineral. Because of its excessively hydrated swelling and the

possibility of heat-induced desiccation cracks, there is a need to explore the potential of improved engineered barrier materials, using inorganic microfibers, to withstand the pressure and temperature for long timescales. When the microfiber is mixed with the bentonite, the desired performance in terms of swelling and strength of the material can be varied.

Thus, this research aims to achieve several objectives. Firstly, this study investigates the combined effect of fiber reinforcement and temperature elevation on the swelling pressure of bentonite. Secondly, the compressibility behavior of the bentonite is evaluated in terms of fiber inclusion and temperature application. Thirdly, this research analyzes the shearing behavior of the bentonite with respect to different fiber contents and its behavior in the critical state. Lastly, its effectiveness as a potential engineered barrier material is assessed to safely store high-level radioactive waste.

1.4 THESIS ORGANIZATION

The study consists of five main chapters discussing the essential information regarding this research work. Chapter 1 provides the background of the study, its significance, and the main objectives. Chapter 2 presents an extensive review of related literature, especially the fundamental concepts needed to understand the phenomena observed in this study. This chapter also provides a review of the current status of the nuclear repository from various countries around the globe. Chapter 3 focuses on the swelling and compressibility characteristics of pure and reinforced bentonite under elevated temperatures. It discusses the methodology of how the swelling pressure test was

conducted, the obtained experimental results, and the corresponding conclusion. Chapter 4 focuses on the shearing behavior of reinforced bentonite. In this chapter, the details of the direct simple shear test are elaborated as well as the observed trends for both peak and residual strengths. It also gives the derivation of the Modified Cam Clay Model and the analysis of the experimental data through the model in the critical state. Chapter 5 summarizes the pertinent findings of this research and the author's suggestions for future work.

CHAPTER 2. REVIEW OF RELATED LITERATURE

2.1 NUCLEAR ENERGY

The United States of America is the second largest energy consumer across the globe, accounting for 17% of the total world's total primary energy consumption in 2019 (U.S. Energy Information Administration, 2021). Along with the extensive energy usage, the country is also considered the world's largest producer of nuclear power, having been responsible for more than 30% of the worldwide nuclear generation of electricity or 809 BkWh of the total annual nuclear electricity (World Nuclear Association, 2022a). Nowadays, 93 nuclear reactors are operating across the country, and 28 states possess several nuclear power plants (U.S. Energy Information Administration, 2022).

In fact, nuclear energy is becoming popular nowadays as compared to fossil fuels. Fossil fuels are considered non-renewable energy sources. When fossil fuels are processed and burned, they produce huge amounts of carbon dioxide. These threaten the atmosphere by trapping heat due to the said greenhouse gas. Figures 1 and 2 present the percentage of greenhouse gas emissions for each gas type from the U.S. and the world, respectively. Whether on a national or global scale, carbon dioxide leads the gas emissions, proving that fossil fuel is a significant factor contributing to the greenhouse gas effect.

Another advantage of nuclear energy is that it produces minimal waste. According to the U.S. Department of Energy (2021), nuclear fuel is extremely dense. Figure 3 shows how much natural gas, oil, and coal are used to produce the same amount of nuclear energy from a single uranium pellet.

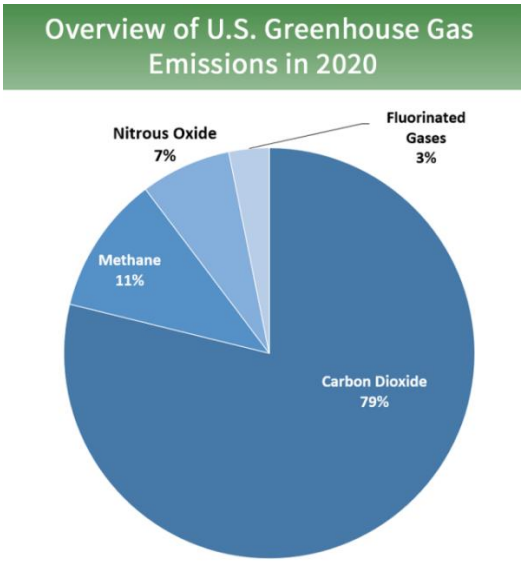

Figure 1. Overview of U.S. greenhouse gas emissions in 2020 with total U.S. emissions of 5,981 million metric tons of CO_2 equivalent (U.S. Environmental Protection Agency, 2022b).

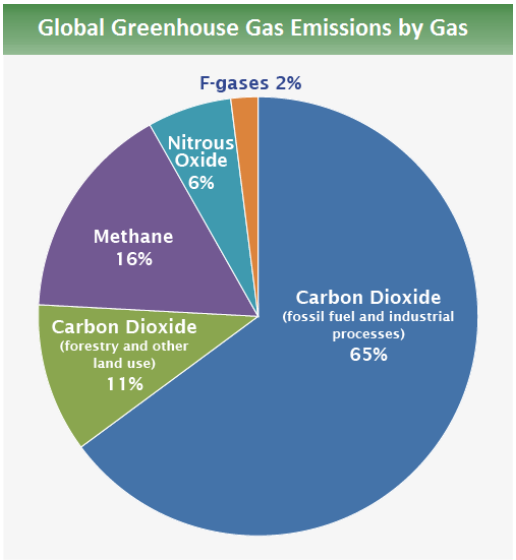

Figure 2. Global greenhouse gas emissions by gas in 2010 (U.S. Environmental Protection Agency, 2022a).

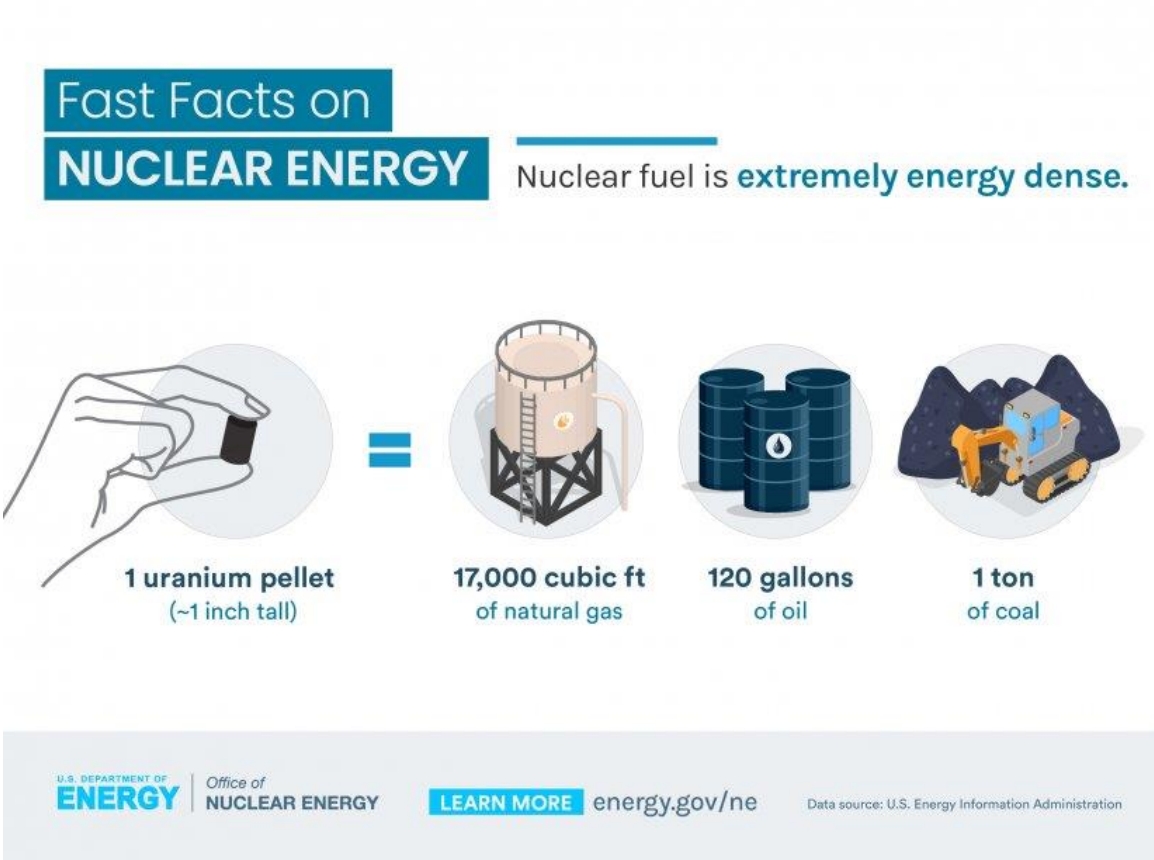

Figure 3. Amount of natural gas, oil, and coal used to produce the same amount of nuclear energy from a uranium pellet (U.S. Department of Energy, 2021).

2.2 TYPES OF RADIOACTIVE WASTE

2.2.1 LOW-LEVEL RADIOACTIVE WASTE

There are different types of radioactive waste, including the low-level radioactive waste. The low-level waste includes items with radioactive material or have become radioactive through exposure to neutron radiation (U.S. Nuclear Regulatory Commission,

2020b). With a half-life of less than 100 days, this waste is typically stored on-site with the following conditions: it must be decayed and possible to be disposed of like an ordinary trash, or if there is a lot of waste enough to send to a low-level waste disposal site. Examples of this waste are wiping rags, mops, filters, medical tubes, swabs, and syringes.

Figure 4. Examples of low-level radioactive waste (Australian Department of Industry, 2015).

2.2.2 INTERMEDIATE-LEVEL RADIOACTIVE WASTE

The second type of nuclear waste is intermediate-level radioactive waste. As stated by Canadian Nuclear Safety Commission (2021), this generally contains long-lived radionuclides in concentrations. With this, the intermediate-level waste would require appropriate isolation and containment capable of holding for more than several hundred

years. Interestingly, intermediate-level waste does not need any provision for heat dissipation during the storage and disposal. Such waste includes chemical sludge, ion-exchange resins, reactor water treatment residues and filters used for purifying reactor's cooling water, and some radioactive sources used in radiation therapy. Its half-life is usually less than 30 years, and this should be disposed of within an on-site near-surface repository.

Figure 5. Damaged barrel at the Waste Isolation Pilot Project showing leakage of radioactive materials (Bryan, 2015).

2.2.3 HIGH-LEVEL RADIOACTIVE WASTE

High-level radioactive waste is the most concerning type of nuclear waste among the mentioned wastes. According to U.S. Nuclear Regulatory Commission (2020a), this is composed of highly radioactive material produced as a byproduct of the reactions

happening within the nuclear reactor. This can be in either spent reactor fuel for disposal or remaining waste materials after reprocessing the spent fuel. Since the spent nuclear fuel is no longer useful for generating electricity, it has a slower fission process. However, it still has a high temperature and high radioactivity, which can be harmful to the environment. Thus, a permanent disposal repository such as a deep geological repository is built for the storage of high-level radioactive waste.

Figure 6. Loading silos with canisters containing vitrified high-level waste in the United Kingdom. Each disc on the floor covers a silo holding ten canisters (World Nuclear Association, 2022b).

Figure 7. Uranium pellets cool after passing through a furnace inside a nuclear plant in Ust-Kamenogorsk, Kazakhstan (Jani-Friend, 2021).

2.3 DEEP GEOLOGICAL REPOSITORY

2.3.1 YUCCA MOUNTAIN (USA)

Powered by the 1982 Nuclear Waste Policy Act, the Yucca Mountain in Nevada has been assigned as the sole U.S. national repository for spent fuel and high-level radioactive waste generated from nuclear power and military defense programs. It is expected that this repository is statutorily limited to contain 70,000 metric tons of spent nuclear fuel and high-level waste (U.S. Environmental Protection Agency, 2022d). The U.S. Department of Energy (DOE) applied for a license for repository construction at the Yucca Mountain to the Nuclear Regulatory Commission (NRC) on June 3, 2008 (Lawrence Berkeley National Laboratory, 2022b). According to the (U.S. Environmental Protection

Agency, 2022c), the Yucca Mountain was selected as the U.S. first geologic repository for high-level radioactive waste disposal because of the following reasons:

1. Yucca Mountain area has a desert climate.
2. Yucca Mountain is a volcanic ridge located 100 miles northwest of Las Vegas, which is considerably far from human settlements.
3. Yucca Mountain is secured 1000 ft under the surface in a closed hydrologic basin
4. The ashes from its volcanic eruptions turned into an igneous rock called ‘tuff.’ Due to regional geologic forces, the movement of the tuff layers formed the crest of the mountain. Below this layer is a carbonate rock formed from the sediments laid down at the bottom of ancient seas existed in the area. Therefore, this location is protected by natural geologic barriers.

Although this location is the only candidate for a nuclear waste disposal site, it faced a negative opinion from the general public and hence, causing excessive project delays. Given that the radioactive waste remains at the nuclear reactor sites for such a long time, this prompted the U.S. Government Accountability Office (2009) to investigate on the site’s attributes, challenges, costs, and potential alternatives. Since its inception in 1998 until 2020, this project has cost around $12.3 billion in damages, and will continue to cost $500 million per year beyond 2020. Two possible alternatives are suggested: centralized and on-site storage. Both suggestions could work to allow more time to find a final candidate for permanent disposal. At present, this project is still halted and there is no sign of reviving the project soon. Meanwhile, the high-level radioactive waste and spent fuel are temporarily stored within the nuclear powerplant site.

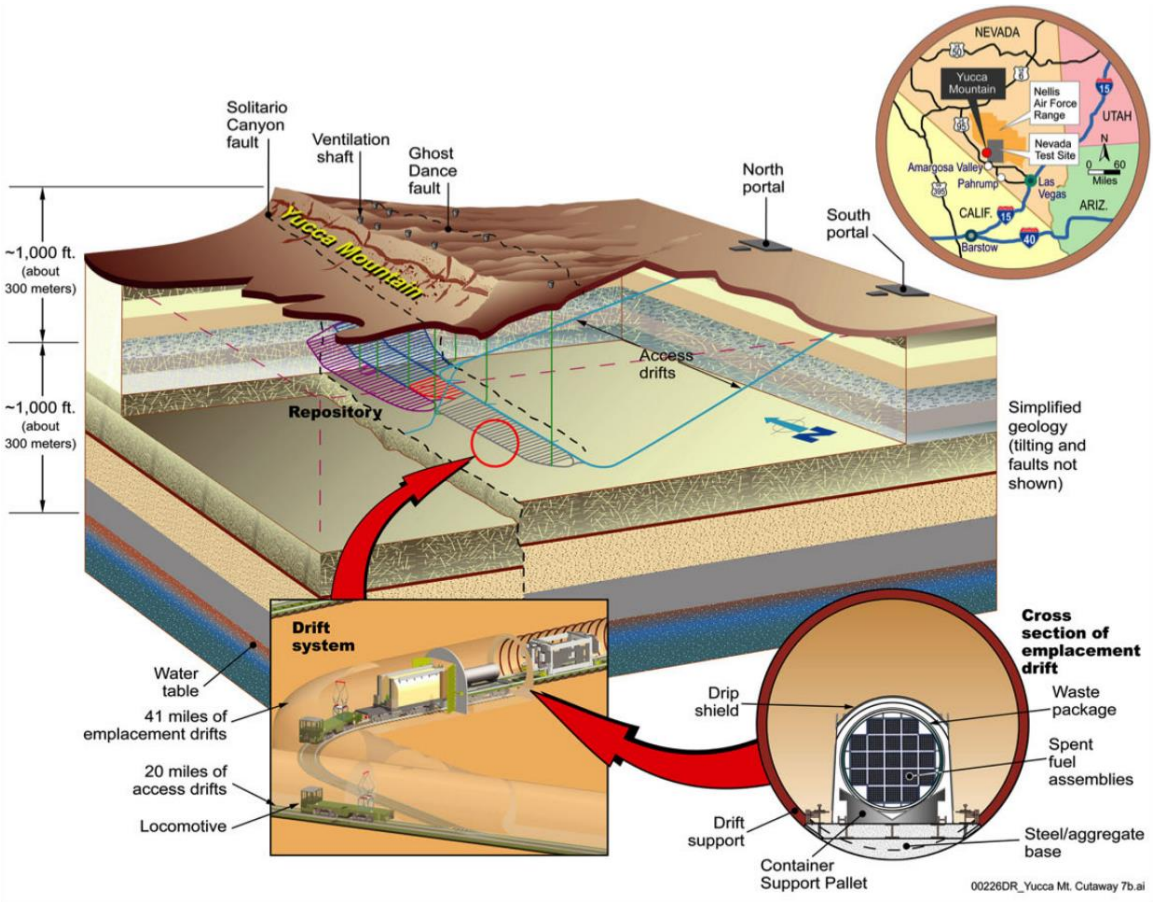

Figure 8. Cutaway image of Yucca Mountain, rock layers, and the planned network of repository tunnels along with cross-sectional view of an emplacement drift (Halecky, 2010).

2.3.2 KBS-3 (SWEDEN)

The Swedish Nuclear Fuel and Waste Management Company, or known as SKB, has established a disposal system that isolates the copper canister from the host rock with the use of highly compacted bentonite blocks. SKB developed the KBS-3V design standard, where the metal canister is oriented in the vertical direction on a bentonite block and enclosed with bentonite rings. The cement block is used to seal the topmost bentonite plug, while the rest of the galleries are filled with backfill material. This whole system is installed at around 500 m depth in granitic host rock saturated with groundwater. The KBS-3 concept for the disposal of spent nuclear fuel is provided in Figure 9. Currently, the Forsmark site at Östhammar, Sweden has been chosen to be the location of the nuclear repository for KBS-3. With an expected amount of 12,000 tons of spent nuclear fuel, this translates to approximately 6,000 canisters in the KBS-3 repository.

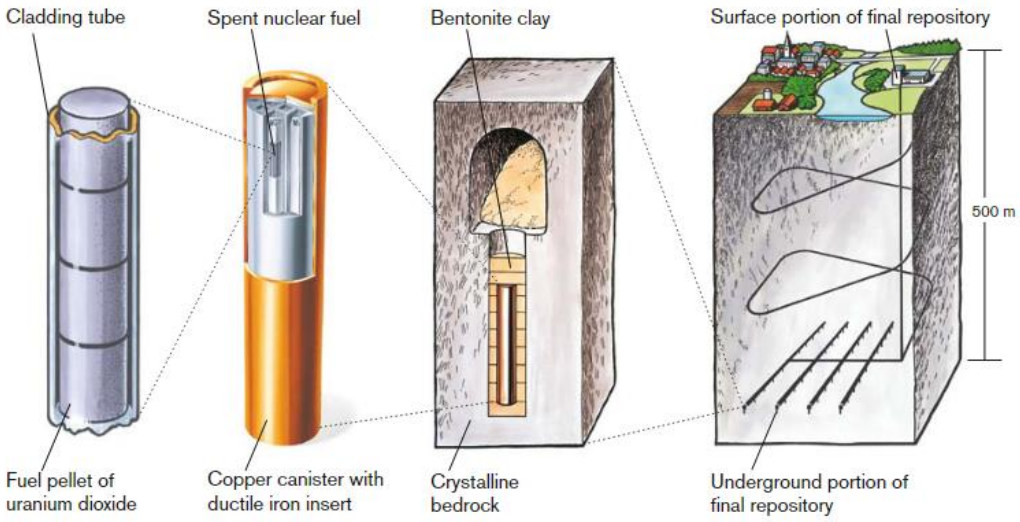

Figure 9. The KBS-3 concept for disposal of spent nuclear fuel (SKB, 2011).

2.3.3 FEBEX (SPAIN)

The Full-scale Engineered Barriers Experiment (FEBEX) is developed by Enresa, the Spanish Radioactive Waste Management Organization. This nuclear waste disposal system follows the Spanish reference design for high-level radioactive waste disposal in crystalline rock. A mock-up test is currently ongoing at CIEMAT in Madrid, Spain. Meanwhile, the actual FEBEX is situated at the Grimsel test site in Switzerland. The current layout of the FEBEX in-situ test is presented in Figure 10. As seen in the figure, the canisters are placed horizontally while a clay barrier consisting of highly compacted bentonite blocks surrounds the canisters.

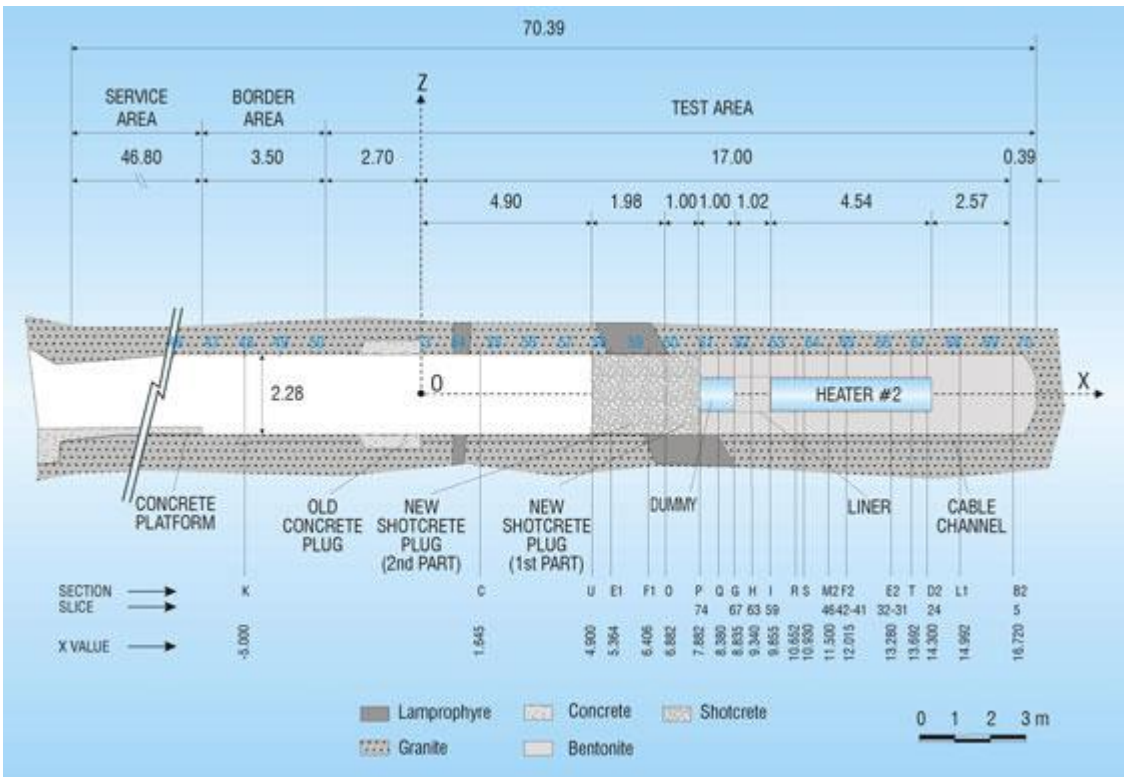

Figure 10. The current layout of the FEBEX in-situ test (Grimsel Test Site, 2022).

This experiment is considered the longest running full-scale experiment in the nuclear repository research field since 1997. By removing heater #1, the system was partially dismantled in 2002 to investigate the behavior of the bentonite and the condition of the instruments during the 5-year heating period of 100°C, while heater #2 is still in place. After 18 years of operation, Villar et al. (2020) reported their findings upon the complete dismantling of the setup. Some of these include that all the gaps between the bentonite blocks were still intact, and the vertical cracks were not the preferential water pathways. Additionally, the water content decreases from the granite towards the axis of the gallery while the density follows the opposite trend. In the rear most part of the gallery, the bentonite possesses the highest water contents and lowest dry densities due to construction gaps, leading to lower installation density. On the other hand, the lowest water contents and the highest dry density were found near the rear half of the heater, where the temperatures were higher than the rest of the gallery.

2.3.4 DECOVALEX PROJECT

The DEvelopment of COupled Models and their VALidation Against EXperiments in Nuclear Waste Isolation (DECOVALEX) is a comprehensive research collaboration within the international community, such as Canada, China, Finland, France, Japan, Germany, Spain, Sweden, Switzerland, United Kingdom, South Korea, Czech Republic, Taiwan, and the USA (Lawrence Berkeley National Laboratory, 2022a). Its main objective is to provide mathematical models in thermo-hydro-mechanical (THM) and thermo-hydro-chemical (THC) coupled processes in the geological repositories. This project was initiated

in 1992, yielding several impactful outputs available for sharing between modeling teams. The project's approach is to initially conduct laboratory and field experiments, followed by collective studies and modeling of their test cases by the DECOVALEX participants. Various large-scale experiments have been performed and modeled through this project, including the FEBEX and the Yucca Mountain drift-scale heater test. Although the DECOVALEX heavily focuses on the modeling part in interpreting the behavior of the repository through time, its system is deeply connected with the experimental data provided by the laboratory and field measurements.

2.4 DIFFUSE DOUBLE LAYER THEORY

Clay is one of the interesting soil types for research due to its behavior change based on the clay mineral it possesses. According to (Das & Sobhan, 2012), there are three important clay minerals: kaolinite, illite, and montmorillonite. These minerals differ in the atomic structure and the arrangement of the silica-gibbsite sheet. Specifically, for montmorillonite, one gibbsite sheet is in between the two silica sheets. Relative to the other layers, there is a considerable space where a large amount of water is attracted. Once the clay is influenced by water, exchangeable cations such as Ca^{2+}, Mg^{2+}, Na^{+}, and K^{+} and some anions float around the clay plates.

With varying cation exchange capacities and isomorphous substitutions, the montmorillonite can demonstrate different swelling extent depending on its type of ion (Lambe & Whitman, 1969). According to van Olphen (1977), the swelling of montmorillonite involves two mechanisms: crystalline swelling and the diffuse double

layer. Due to ion and clay surface hydration, crystalline swelling occurs. On the other hand, because of hydrogen bonding, adsorbed and double-layer water are formed. Double-layer water is the water held to the clay particles due to the force of attraction while adsorbed water is the innermost layer of double-layer water which is held firmly by clay particles. In a typical montmorillonite particle, the montmorillonite crystal is squeezed tightly by the adsorbed water while being surrounded by the double-layer water. This structure explains the high plasticity and high swelling capability of clays with high montmorillonite content, such as bentonite. A good example of the said layer arrangement of montmorillonite along with the adsorbed and diffuse double layer is shown in Figure 13, obtained from Schanz & Tripathy (2009).

Two of the most popular types of bentonite are sodium and calcium bentonites. The swelling mechanism of sodium bentonite consists of both osmotic and crystalline swelling. Meanwhile, calcium bentonite typically undergoes crystalline swelling only. With sodium bentonite possessing a higher cation exchange capacity than calcium bentonite, the sodium bentonite was able to swell more than the calcium bentonite. Through this concept, it will be more beneficial to use sodium bentonite for the purpose of high-level radioactive waste disposal. Aside from this purpose, sodium bentonite is widely used in the U.S. due to its abundant supply especially in Wyoming.

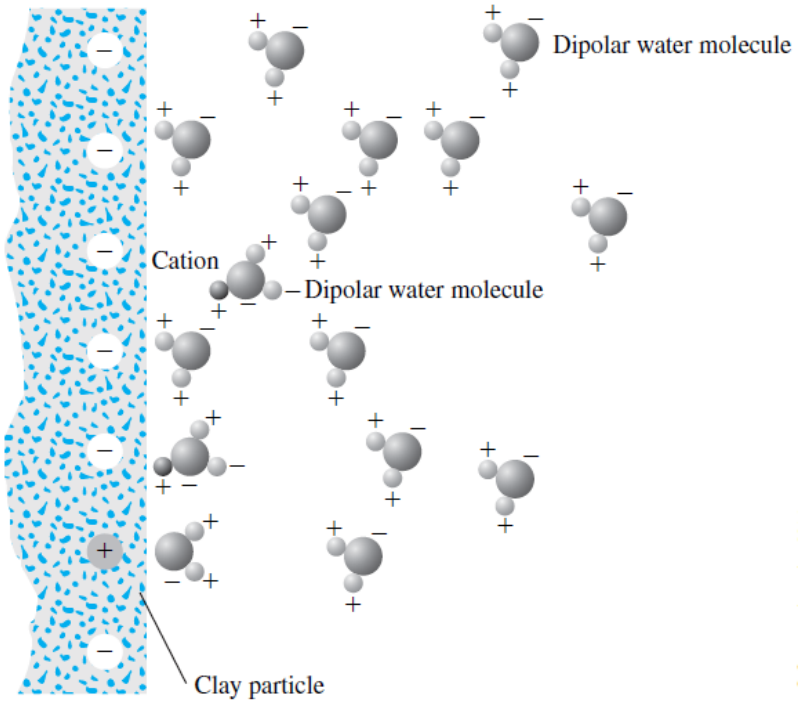

Figure 11. Attraction of dipolar molecules in diffuse double layer (Das & Sobhan, 2012).

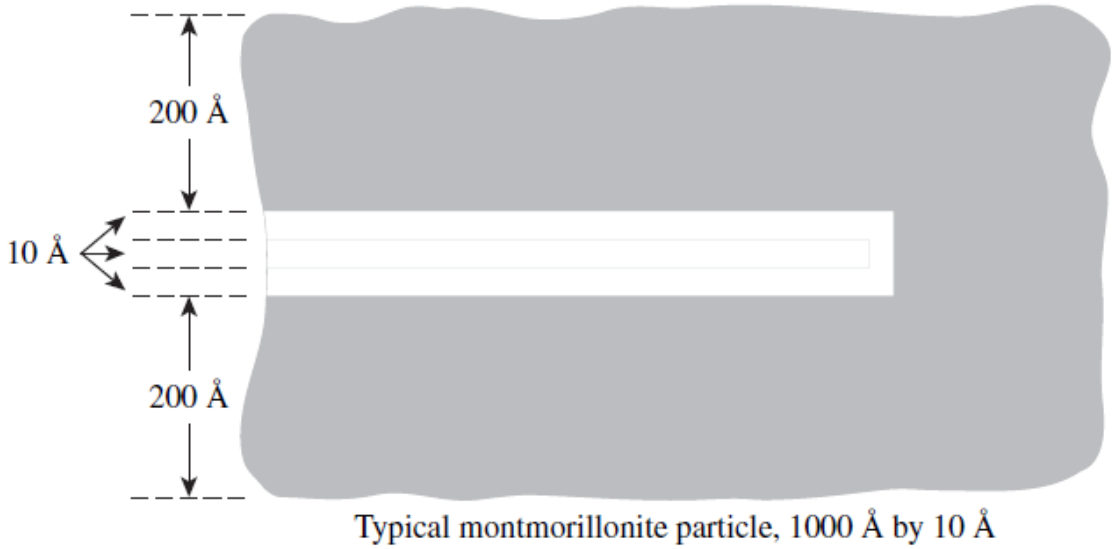

Figure 12. Clay water for a typical montmorillonite particle (Das & Sobhan, 2012).

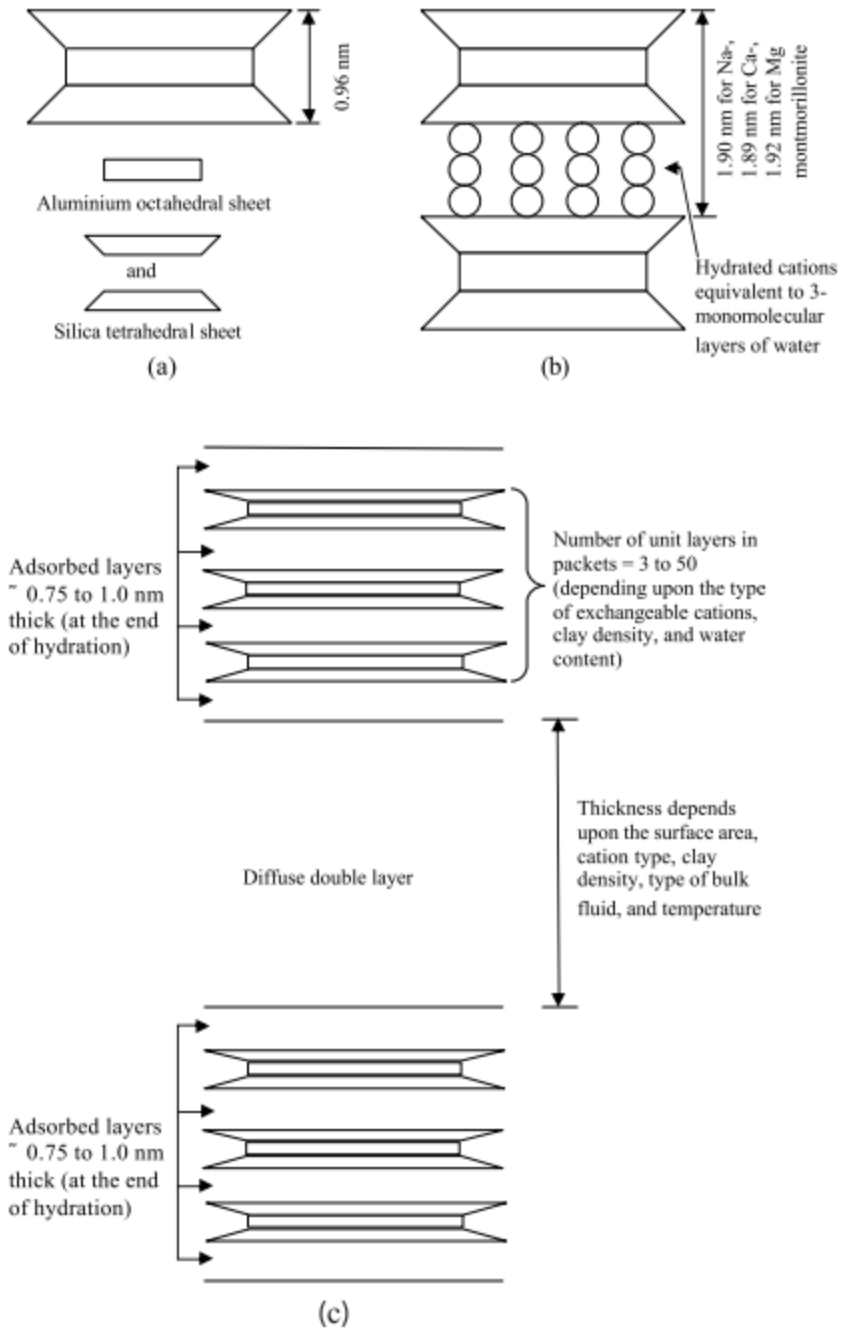

Figure 13. Schematic diagrams of the unit layer arrangement for montmorillonite (a) unit layer without polar molecules and (b) hydrated cations within unit layers, and (c) arrangement of unit layers, adsorbed layer, and diffuse double layer (Schanz & Tripathy, 2009).

2.5 FIBER REINFORCEMENT

One of the widely used mechanical stabilization methods in the field of geotechnical engineering is the fiber reinforcement. Various researchers have used fibers made of polymer in their specimens to investigate their mechanical behavior and how these can alter the different engineering properties of the soil. A number of studies have explored this stabilization method for their respective soil types and purposes (Maher & Woods, 1990; Yetimoglu et al., 2005; Chaduvula et al., 2017; Soltani et al., 2018; Liu et al., 2021).

For example, Chaduvula et al. (2017) utilized polyester fibers to possibly reduce the desiccation cracking of expansive soils for landfill liners. The polyester used has an effective diameter of 40 μm, with varying fiber lengths of 15, 30, and 50 mm and fiber contents of 0.25, 0.5, and 0.75% by weight. The expansive clay used in this research is a high-plasticity clay (CH). The specimen was subjected for desiccation under a 500 W Tungsten Halogen lamp with a constant temperature of 50°C and relative humidity of 20%. It was dried for 450 mins and the weight was measured every 50 mins to monitor the amount of moisture loss. In this study, digital image analysis was done to determine the fiber reinforcement effect on the desiccation cracking behavior of the expansive soil. It has been concluded that the addition of fibers controlled the following: crack width opening, cracked area, and propagation of cracks through the bridging action of fibers.

Another research from Narani et al. (2020) used waste tire textile fibers as reinforcement agents in an expansive soil. The waste tire textile fiber has an equivalent diameter of 0.8 mm, length of 20 mm, tensile strength of 600 MPa, elastic modulus of 2.7 GPa, and melting point of 256°C. This fiber was reinforced to the sodium bentonite in 1%,

2%, 3% 4% fiber contents by weight. A comprehensive set of laboratory experiments, such as standard compaction, Split Tensile Strength, swelling-consolidation, volumetric shrinkage, and desiccation cracking tests, were performed to assess the behavior of the fiber-reinforced specimen. In this study, the fibers completely altered the tensile behavior of the soil, where a double-peaked behavior and an improvement in the post-peak behavior were observed due to the fiber reinforcement. The desiccation cracking test involves a water content of 1.04 times the liquid limit of bentonite (415%), and the specimen was dried at a constant temperature of 60°C for two days and 110°C for another two days. Furthermore, Figure 14 shows the evolution of desiccation cracking with varying fiber contents (f_c), and it is proven that fibers can effectively decrease the cracked area during the drying process.

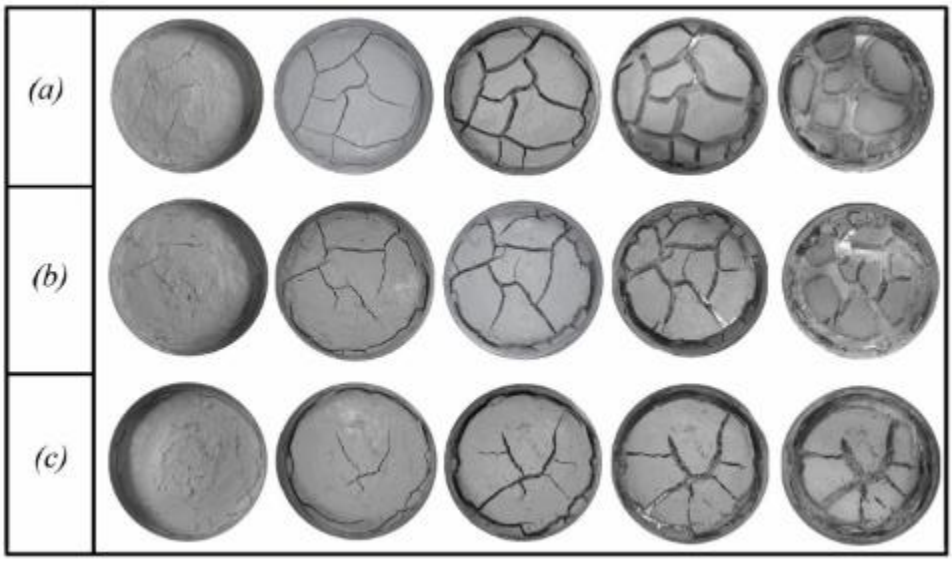

Figure 14. Evolution of desiccation cracking: (a) f_c – 0%, (b) f_c – 2%, and (c) f_c – 4% (Narani et al., 2020).

2.6 SWELLING PRESSURE USED FOR BUFFER MATERIALS

Several researchers have investigated the application of bentonite in deep geological disposal, particularly the material's swelling pressure (Yang et al., 2016; Bian et al., 2019). The swelling pressure is a vital parameter for the long-term performance of the nuclear waste repository. A low swelling pressure may cause the canister to sink while a high swelling pressure may destroy the canister (Dohrmann et al. 2013). Various countries have considered different buffer function indicators in their respective reference designs of the EBS. The acceptable range of swelling pressure for the KBS-3 design is between 0.2 to 15 MPa to satisfy the following functions: to prevent canister sinking, limit the advective transport, and limit the pressure on the canister and host rock (SKB, 2011). Hence, an appropriate swelling pressure in terms of containment and retardation is desired to fulfill the buffer functions. However, pure bentonite offers a limited capability for the EBS. Having a low thermal conductivity, the heat from the nuclear waste accumulates in the repository and increases its overall temperature. Furthermore, shrinkage and cracking of the pure bentonite are imminent near the location of the canister. Inorganic microfibers are known to mitigate such a situation and are proposed as a reinforcement material to the bentonite to address the potential generation of desiccation cracks in the EBS due to the heat emitted from the radioactive waste.

Table 1. Summary of the buffer function indicators and the criteria they should fulfill based on the KBS-3 disposal system (Dohrmann et al., 2013).

Buffer Function Indicator	**Criterion**	**Rationale**
Bulk Hydraulic Conductivity	$<10^{-12}$ m/s	Limit advective transport (containment, retardation)
Swelling Pressure	>1 MPa	Limit advective transport (containment, retardation)
Density	2050 kg/m^3	Damp rock shear (containment)
Maximum Temperature	<100°C	Resist transformation (containment, retardation)
Swelling Pressure	>0.2 MPa	Prevent canister sinking (retardation)
Swelling Pressure	<15 MPa	Limit pressure on canister and rock (containment)
Minimum Temperature	>-4°C	Limit pressure on the canister and rock by avoiding freezing (containment)

2.7 SWELLING PRESSURE TESTING APPARATUS

Recent studies have been conducted to incorporate the temperature effect on the consolidation properties of soil. While they may vary from method to method, researchers have been creative in conducting these tests regardless of some challenges encountered with the available laboratory devices. For example, Ye et al. (2013) measured the temperature effects on the swelling pressure and saturated hydraulic conductivity of the compacted bentonite by utilizing a stainless-steel cell with porous stones, a stainless piston with a load transducer on top with a screw cap affixed, mimicking the typical one-dimensional consolidation device. To apply the temperature (20°, 40°, 50°, and 60°C), the whole apparatus was put inside a digital oven. Although this might be an interesting setup, one limitation that this might give is the accuracy of the temperature being directly applied to the actual submerged bentonite sample during the test.

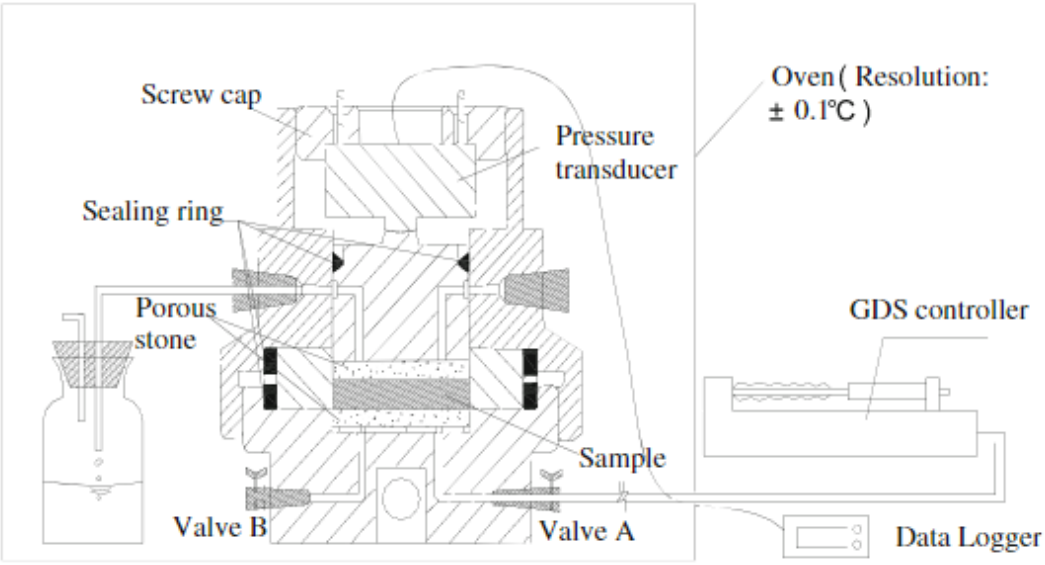

Figure 15. Experimental setup for swelling pressure and saturated hydraulic conductivity test with temperature control (Ye et al., 2013).

Another test setup that can resolve this limitation, in some way, is provided by Bag & Rabbani (2017), where they manufactured a new oedometer with inner and outer cells. The inner cell is considered the specimen chamber while the outer cell is the oil chamber. An electric coil is used to transfer the heat to the outer cell and the oil temperature was monitored using a thermocouple. In this way, only a secondary heat transfer was done to the water and soil specimen.

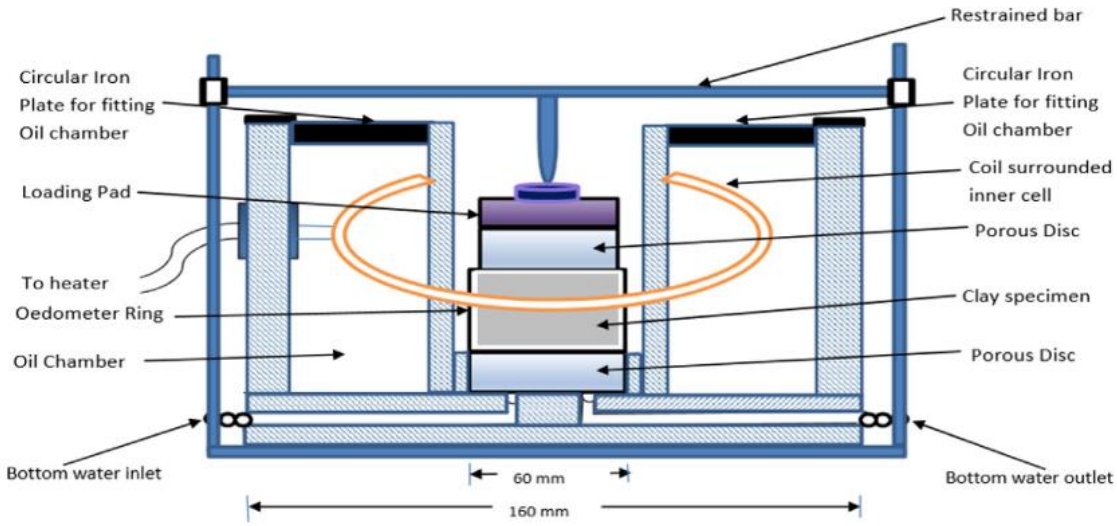

Figure 16. Schematic diagram of the new oedometer (Bag & Rabbani, 2017).

To fully address the abovementioned drawbacks, Shirasb et al. (2020) used a temperature-controlled triaxial cell by surrounding the soil sample with a spiral heater. This has been by far the most effective technique to apply the temperature. While most studies employ this particular type of triaxial device capable of varying the temperature of interest, this is not the case for a one-dimensional consolidation apparatus. Therefore, a modified one-dimensional consolidation device is suggested to obtain the soil's consolidation properties under elevated temperatures.

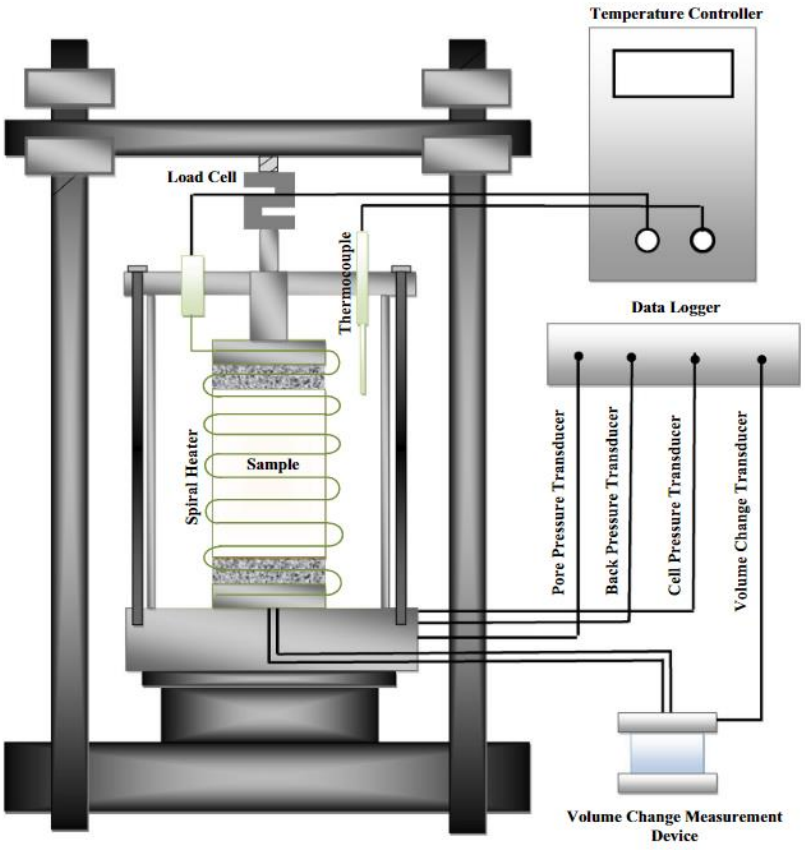

Figure 17. Schematics of the thermal triaxial cell (Shirasb et al., 2020).

2.8 SHEAR STRENGTH PROPERTIES

In the geotechnical engineering practice, the shear strength is an important parameter in assessing how workable the soil is with respect to failure. Various factors may affect the soil shear strength, but it mainly depends on the soil type. Given that an expansive clay like bentonite can be used in different engineering applications, it is important to understand its shearing behavior first.

The main consideration for most projects is to improve the soil strength, and this can be achieved by introducing several reinforcing materials. A number of studies have shown that fibers can significantly affect the shear strength of the soil (Casagrande et al., 2006; Mirzababaei et al., 2017; Mukherjee & Mishra, 2019; Abbaspour et al., 2020; Bojnourdi et al., 2020).

Mukherjee & Mishra (2019) investigated on the hydro-mechanical behavior of the sand-bentonite-glass fiber composite for landfill application. By performing consolidated undrained (CU) triaxial tests, the shear strength parameters were obtained. The inclusion of 1.0% glass fiber with different aspect ratios enhanced the deviatoric stress for each confining pressure. The increase in the ratio between the areas of reinforced and unreinforced soil of the soil-fiber interface can be a possible explanation of this said observation in the deviatoric stress. Additionally, higher fiber aspect ratios within the same fiber content resulted in increasing internal friction angle. However, the cohesion value was almost constant for all aspect ratios. For the unreinforced soil, the specimen showed a sharp horizontal wrinkle during the shearing stage. Furthermore, large deformation with low effective stress was observed in the unreinforced sample. Meanwhile, the reinforced specimens showed slight bulging with mild rupture, signifying higher resistance against volume expansion.

Another interesting finding from Bojnourdi et al. (2020) showed that the polypropylene fibers could affect the shearing behavior of the used motor oil (UMO)-contaminated sand-bentonite mixture. In this study, the randomly-distributed fibers increased the peak strength of the mixture. Post-peak behavior showed a clear sudden drop in the stress-strain curve of the unreinforced mixture. On the other hand, the fiber-

reinforced mixture presented strain-softening behavior regardless of the fiber content. The occurrence of strain softening for the fiber-reinforced samples can be attributed to the fibers holding the shear plates together, even at large shear displacements.

2.9 MODIFIED CAM CLAY MODEL

The Critical State Soil Mechanics, or commonly known as Modified Cam Clay (MCC) Model, is a type of plasticity theory-based soil model used to determine the behavior of the soil at the critical state. In this model, it follows a conventional triaxial test that uses the following general quantities of stress and strain according to Roscoe & Burland (1970):

$$p' = \frac{\sigma_1' + 2\sigma_3'}{3} \tag{1}$$

$$q = \sigma_1' - \sigma_3' \tag{2}$$

$$\eta = \frac{q}{p'} \tag{3}$$

where p' is the mean effective normal stress, q is the deviatoric stress, η is the stress ratio, σ_1' is the effective major principal stress, and σ_3' is the effective minor principal stress.

This soil model consists of three axes: specific volume (v), normal stress (p), and deviatoric stress (q). The specific volume is equal to the void ratio (e) plus 1.0. Combining these axes generates two different planes, which are the $v - \ln p$ and $p - q$ planes. Figures 18 and 19 show both the 3D schematic and 2D planes of the MCC model, respectively.

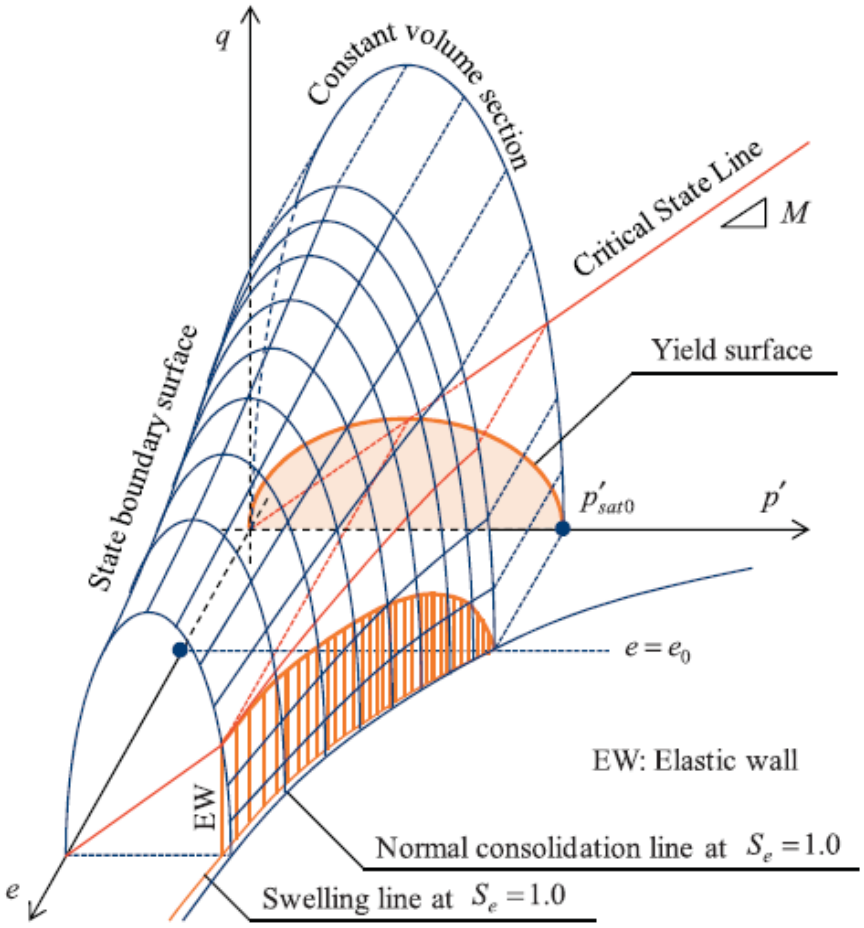

Figure 18. Conceptual schematic of state surfaces and swelling walls in the three-dimensional Modified Cam Clay Model (Takayama et al., 2017).

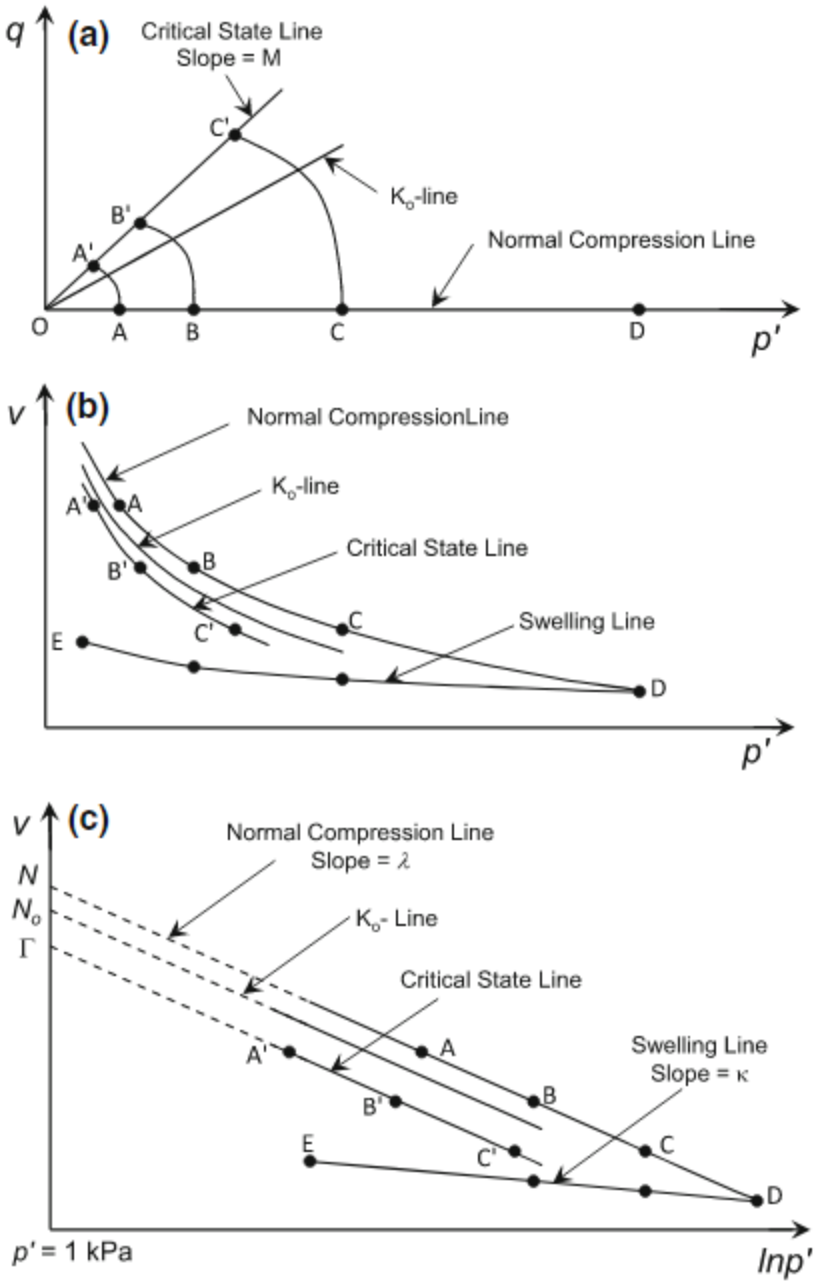

Figure 19. Positions of Normal Compression Line (NCL), K_0 Line, and Critical State Line (CSL) in (a) $p' - q$ plane, (b) $v - p'$ plane, and (c) $v - \ln p'$ plane (Dev et al., 2013).

There are five parameters that are crucial in the analysis of Critical State Soil Mechanics. These include the following:

1. Slope of the Normal Compression Line (NCL) in the $v - \ln p'$ plane (λ)
2. Slope of the swelling line in the $v - \ln p'$ plane (κ)
3. Specific volume at the unit pressure $p = 1\ kPa$ on the NCL (N)
4. Slope of the Critical State Line (CSL) in the $p' - q$ plane (M)
5. Specific volume at the unit pressure $p = 1\ kPa$ on the CSL (Γ)

With the triaxial and consolidation tests, the soil parameters in the $v - \ln p'$ plane can be obtained by processing the data from void ratio to specific volume and calculating the compressibility parameters such as compression index (C_c) and swelling index (C_s). These indices can be converted to the MCC Model in the form of λ and κ, respectively. On the other hand, the triaxial and direct shear tests can provide the shear strength parameters cohesion (c') and friction angle (ϕ') of the soil and in turn, providing the value of M from the friction angle. Therefore, the combination of the consolidation and direct shear tests can be considered a simplified version of the triaxial test in such a way that the important parameters in the MCC Model can still be obtained as well.

CHAPTER 3. SWELLING AND COMPRESSIBILITY BEHAVIOR OF INORGANIC MICROFIBER-REINFORCED BENTONITE UNDER ELEVATED TEMPERATURE

This chapter of the thesis is subject for journal submission.

3.1 OBJECTIVES

In this chapter, the swelling and compressible behavior of glass fiber-reinforced bentonite is investigated to confirm its applicability as a mechanical reinforcement for a buffer material. To evaluate the combined effect of the fiber content and temperature elevation on the swelling pressure, a modified one-dimensional consolidation device was set up and the tests were conducted in triplicates. The apparatus was tailored to apply the elevated temperature to the test specimen via the heated circulating bath. Therefore, this study offers an alternative setup to obtain the thermally induced consolidation properties of the soil specimen through the one-dimensional consolidation test. Lastly, the compressibility parameters were evaluated, and based on these, the hydraulic conductivity was estimated and comparably evaluated.

3.2 MATERIALS

The experimental study used a commercially available granular (2.36 mm) Na-bentonite (BENSEAL®, Houston, Texas). Na-bentonite is the most widely available type of bentonite in the U.S. The index properties of the Na-bentonite are tabulated in Table 2.

For the fiber reinforcement, glass fibers (158B Type 30™, Toledo, Ohio) were added to the bentonite samples in varying contents, specifically 1.0% and 3.0% by weight. The physical properties of the glass fibers are provided in Table 3. The cut glass fibers that were used in this study are shown in Figure 20.

Table 2. Index properties of the bentonite used in this study.

Property	Value
Specific Gravity*	2.6
Liquid Limit (%)	400
Plastic Limit (%)	95
Plasticity Index (%)	305
Optimum Moisture Content (%)	35.0
Maximum Dry Density (kg/m^3)**	1200

*From Baroid Industrial Drilling Products (2011)

**Determined at OMC based on ASTM D698-12

Table 3. Physical properties of the glass fibers used in this study (Owens Corning, 2022).

Property	Value
Length (mm)	12
Diameter (μm)	7-10
Specific Gravity	2.55
Melting Point	1725°C
Thermal Conductivity	1.3 W/m-K
Tensile Strength (MPa)	2410

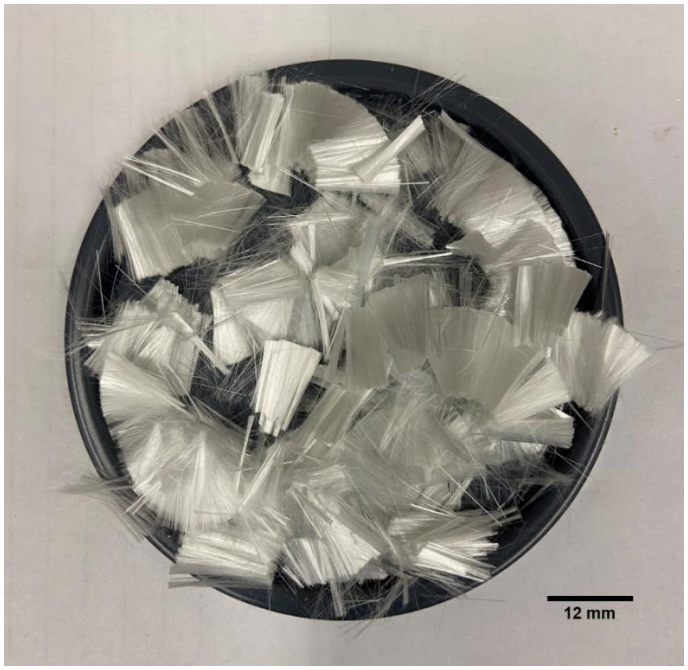

Figure 20. Glass fibers cut into 12-mm lengths are used in the sample preparation. These fibers are mixed with bentonite in 1.0% and 3.0% fiber contents by weight.

3.3 METHODOLOGY

3.3.1 SPECIMEN PREPARATION

The glass fibers were initially in the form of long strands upon acquisition. Prior to reinforcing these fibers with the bentonite, the long microfiber strands were cut into 12-mm lengths, as adapted from Mukherjee & Mishra (2019). To eliminate the randomness of fiber condition and ensure that the specified fiber length was kept constant throughout the cutting process, the fiber lengths were manually measured after cutting and before mixing.

The Na-bentonite is originally in granular form, with an average grain size of 2.36 mm. To minimize the pore spaces within the mixture and enhance the mixing process, the bentonite was then subjected to grinding using an H-4199 soil grinder manufactured by Humboldt Mfg. Co. from Elgin, Illinois. The particle size distribution curve is presented in Figure 21. The particle size of the ground bentonite ranged from 0.075 to 0.85 mm, characterized by a mean diameter (D_{50}) of 0.32 mm, coefficient of uniformity (C_u) of 12.57, coefficient of curvature (C_c) of 1.21, and effective diameter (D_{10}) of 0.04 mm.

Since the bentonite was initially exposed to room temperature and certain humidity, the material had an air-dry moisture content of 8.0 to 10.0%. With this, the ground bentonite was oven-dried for a period of 24 h under 110°C prior to mixing. For the mixing process, the oven-dried bentonite was placed in the mortar mixer along with the cut glass fibers. For the control group, only the bentonite was placed inside the mortar mixer to represent the unreinforced condition. On the other hand, the experimental group, which denotes the reinforced condition, consists of two subgroups considering different fiber

contents: 1.0% and 3.0% by weight. The fibers were then added to the bentonite in the mortar mixer at the dry condition before the mixing process starts.

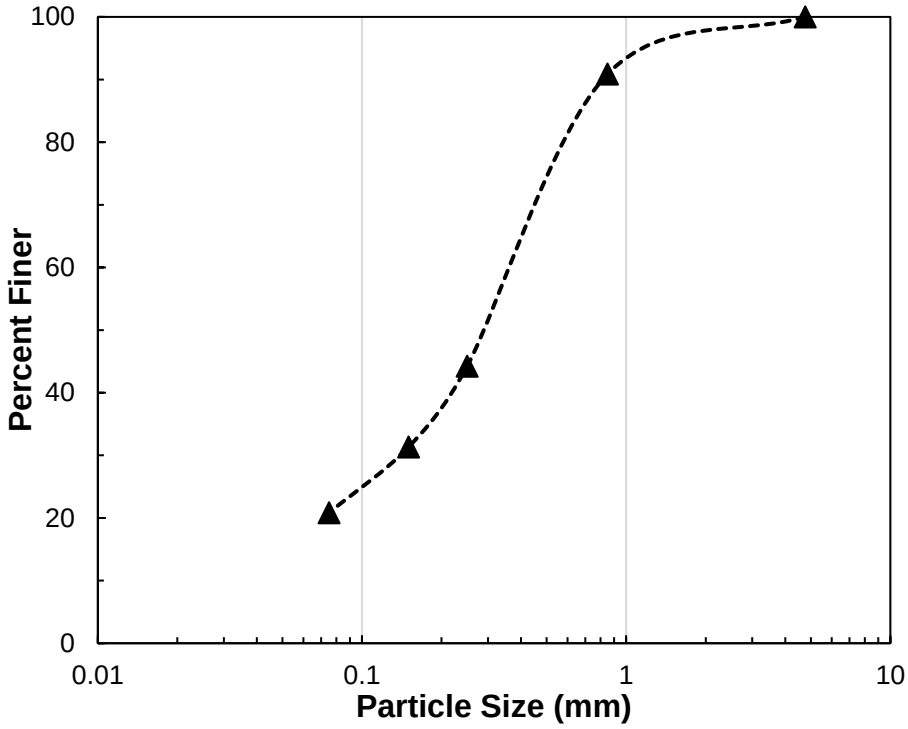

Figure 21. Particle size distribution of the ground bentonite.

As the mixing process started in the mortar mixer, a certain amount of deionized (DI) water corresponding to the optimum moisture content (OMC) of 35.0% by weight was gradually added to the entire mixture. The water content used for all specimens corresponds to the OMC of the pure bentonite sample, obtained from the compaction test. After completing the mixing, the mixture was put in a 101.6-mm diameter compaction mold. Following the ASTM D698-12, Standard Test Methods for Laboratory Compaction

Characteristics of Soil Using Standard Effort (12,400 ft-lbf/ft3 (600 kN-m/m3)), or commonly known as the Standard Proctor Test, the aforementioned test was performed to obtain the dry density of each sample. Using the OMC for all the mixtures, the resulting dry density is 1214 kg/m^3. The whole mixing process and compaction are demonstrated in Figure 22.

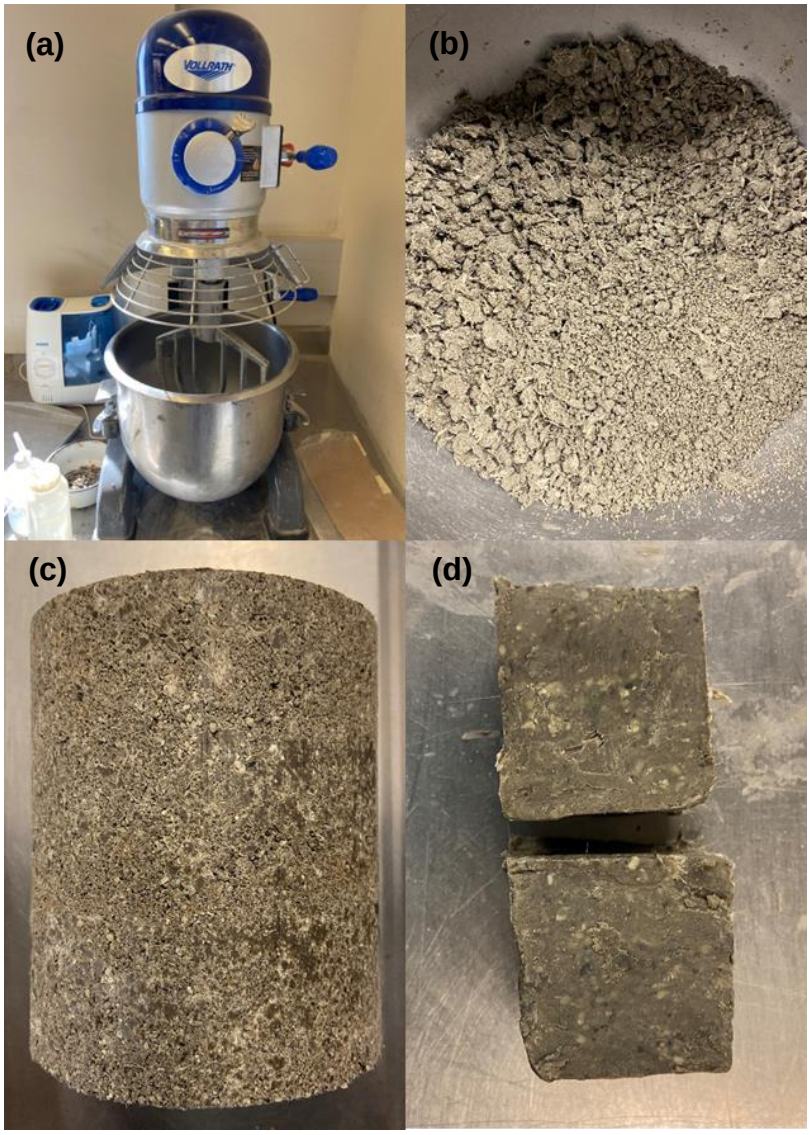

Figure 22. Bentonite-fiber mixing procedure starts with the (a) mortar mixer where the ground bentonite and glass fiber are mixed. After several minutes of mixing with deionized water, (b) the mixed product is shown. To achieve a uniform dry density, the mixed product is compacted, following the Standard Proctor Test. (c) The compacted sample is extruded from the compaction mold. Lastly, to show how the fibers are reinforced in the specimen, (d) cross section of a post-consolidation test sample is presented.

3.3.2 SWELLING PRESSURE TEST

The swelling pressure tests conducted in this research were in accordance with ASTM D4546-21, Standard Test Methods for One-Dimensional Swell or Collapse of Soils, Test Method C or known as the loading-after-wetting test or the swell-consolidation test. As stated by this standard, the selected test method mainly follows the ASTM D2435-11, Standard Test Methods for One-Dimensional Consolidation Properties of Soils Using Incremental Loading, commonly known as the conventional one-dimensional consolidation test. The device used in this test is the GeoJac Digital Load Actuator for consolidation manufactured by GeoTAC of Trautwein (Houston, Texas). The consolidation ring containing the compacted sample was placed in the consolidation cell in this test. Initially subjecting the sample to a seating pressure of 100 kPa and inundating the specimen with the DI water, the sample was allowed to swell for 48 h. The sample was observed with no further volume change relative to its previous readings; hence, the swelling period was restricted to this time interval as the specimen achieved its equilibrium condition. Following the swelling period was the application of subsequent vertical loads for 24 h at each applied load to establish consolidation. With a load increment ratio of unity, the sample was loaded to a maximum vertical pressure of 3000 kPa. The deformation readings were taken at time intervals of 0.5 min, 1 min, 2 min, 4 min, 8 min, 15 min, 30 min, 1 h, 2 h, 4 h, 8 h, and 24 h for each applied load. The induced strain corresponding to each loading step was measured to plot the vertical stress vs. vertical strain curve. In this test, the swelling pressure is defined as the vertical pressure required to revert the test specimen to its original height (i.e., zero strain). Using the mentioned graph, the pressure corresponding to the zero strain would be determined as the swelling pressure. The

swelling pressure test was done in triplicates per testing group to ensure data accuracy and the vertical stress vs. vertical strain data were averaged.

3.3.3 APPLICATION OF ELEVATED TEMPERATURE

Swelling pressure tests were conducted under both ambient (22°C) and elevated (50°C) temperatures to investigate the effect of temperature elevation to the swelling pressure and compressibility behavior of the unreinforced and reinforced bentonite. Illustrated in Figure 23 is the test setup for the application of elevated temperature. A VWR 89202-966 circulating bath (Radnor, Pennsylvania) capable of generating a temperature range of -20° to 135°C was used for this purpose. Silicone tubing surrounds the bentonite sample and the deionized water, and directly transfers the heat from the water bath. Through the silicone tubing covered with insulation, the heated liquid circulated in the system. A portion of the silicone tubing was inundated with the DI water in the consolidation cell to transfer the heat from the circulating bath to the consolidation assembly, demonstrating the application of elevated temperature. An aluminum foil cover was placed on top of the consolidation cell to minimize the evaporation from the assembly as well. To ensure that the elevated temperature in the system was kept constant, temperature monitoring was simultaneously performed at various time periods.

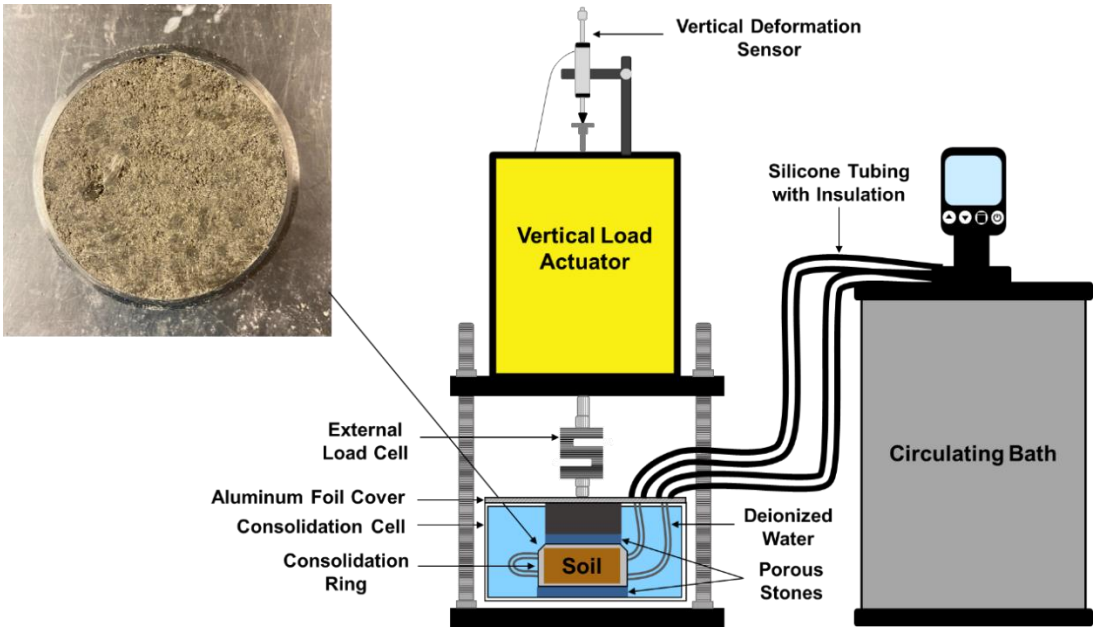

Figure 23. Swelling pressure test setup consisting of the oedometer and circulating bath for the application of elevated temperature.

3.3.4 DETERMINATION OF COMPRESSIBILITY CHARACTERISTICS AND HYDRAULIC CONDUCTIVITY

Aside from the vertical stress vs. vertical strain graph, the void ratio vs. pressure in the logarithmic scale (e-log p) graph is also one of the expected outputs of the swelling pressure test. From this plot, various compressibility characteristics can be derived. First, the initial and succeeding void ratios are calculated based on the consolidation test data using the following equations:

$$e_0 = \frac{H_0 - H_s}{H_s} \tag{4}$$

$$e_{n+1} = e_n - \frac{\Delta H_{n+1}}{H_s} \tag{5}$$

where e_0 is known as the initial void ratio, H_0 is the initial height of the sample, H_s is the height of solids in the specimen, e_{n+1} is considered the succeeding void ratio brought by the initial incremental loading, and ΔH_{n+1} is the specimen deformation from the initial and final dial readings for the current applied loading. The abovementioned Eqs. (4) and (5) were derived from the detailed procedure discussed in (Das & Sobhan, 2012).

After performing the necessary calculations, the e-log p graph consists of two parts: the loading and unloading portions, which are better described as the compression and decompression paths. These loading and unloading steps are performed during the consolidation test to determine the compression and swelling indices (C_c and C_s), respectively. Once the maximum vertical pressure of 3000 kPa has been applied through

compression, the decompression shall take place afterward. The slope of the compression path is considered the C_c while the decompression path corresponds to the C_s.

On another note, the coefficients of volume compressibility and consolidation (m_v and c_v) also describe the compressibility behavior of the soil. In this study, the calculation of m_v follows the formula:

$$m_v = \frac{\Delta e}{\Delta \sigma'(1 + e_0)} \tag{6}$$

where Δe is the change in void ratio, $\Delta \sigma'$ is the change in applied vertical pressure, and e_0 is the initial void ratio of the bentonite sample. Meanwhile, calculation of c_v utilizes the hyperbola method suggested by Sridharan & Prakash (1985). The coefficient of consolidation is calculated as:

$$c_v = 0.3\left(\frac{mH_{dr}^2}{D}\right) \tag{7}$$

where m is the slope of the linear portion of $t/\Delta H$ vs. time t graph, ΔH is the specimen deformation, H_{dr} is the average longest drainage path during consolidation, and D is the intercept of the linear portion of $t/\Delta H$ vs. time graph on the $t/\Delta H$ axis.

Hydraulic conductivity (k) is also an important parameter that this study aims to evaluate. This parameter refers to the ability of the fluid to flow through the pore space and is better described using the Darcy's Law. To establish its connection with the compressibility properties, Terzaghi's consolidation theory is used for this purpose. The derived equation of the hydraulic conductivity is as follows:

$$k = c_v \gamma_w m_v \quad (8)$$

where γ_w is the unit weight of water (9.81 kN/m^3 or 62.4 lb/ft^3).

3.4 RESULTS AND DISCUSSION

3.4.1 SWELLING PRESSURE

From the swelling pressure test, the vertical stress vs. vertical strain plot at various fiber contents and temperature conditions is shown in Figure 24. The swelling pressure values are tabulated in Table 4. In this research, both fiber content and temperature are considered as dependent variables. From these values, the combined effect of the abovementioned variables on the swelling pressure is further discussed in the following subsections.

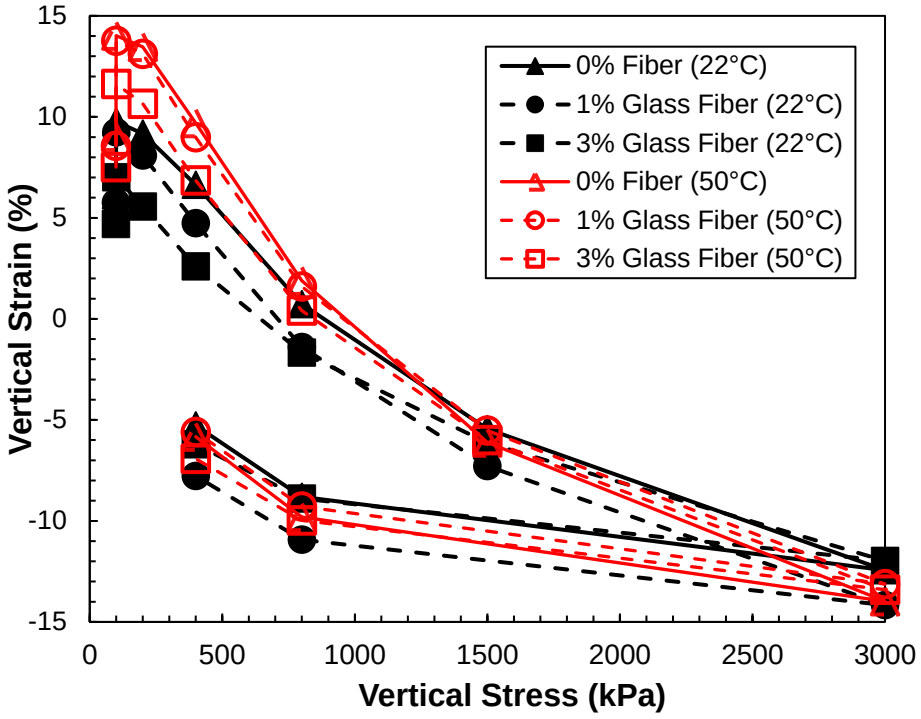

Figure 24. Vertical stress vs. vertical strain to determine the swelling pressure for 0.0%, 1.0%, and 3.0% glass fiber under room temperature (22°C) and elevated temperature (50°C).

Table 4. Swelling pressure values obtained from the consolidation tests.

Swelling Pressure		
Fiber Content	Temperature	
	22°C	50°C
0.0%	**883 kPa**	**966 kPa**
1.0%	**709 kPa**	**957 kPa**
3.0%	**644 kPa**	**845 kPa**

3.4.2 EFFECT OF FIBER CONTENT ON THE SWELLING PRESSURE

The swelling pressure changes with respect to the fiber content. The measured swelling pressures at 0.0%, 1.0%, and 3.0% fiber contents for 22°C room temperature are the following: 883, 709, and 644 kPa, respectively. It can be inferred that as the fiber content increases, the swelling pressure decreases. In addition to that, the reduction in swelling pressure is more pronounced at 3.0% fiber content, corresponding to a 27.1% decrease as compared to the unreinforced bentonite.

Meanwhile, the swelling pressures for the same set of fiber contents (0.0%, 1.0%, and 3.0%) for 50°C elevated temperature are as follows: 966, 957, and 845 kPa, respectively. Clearly, a similar decreasing trend in the swelling pressure has been observed once the fibers had been added. It can be seen in Figure 25 that the inclusion of 3.0% fiber content by weight had vastly affected the swelling pressure, resulting in a decrease of 12.5% in this dataset.

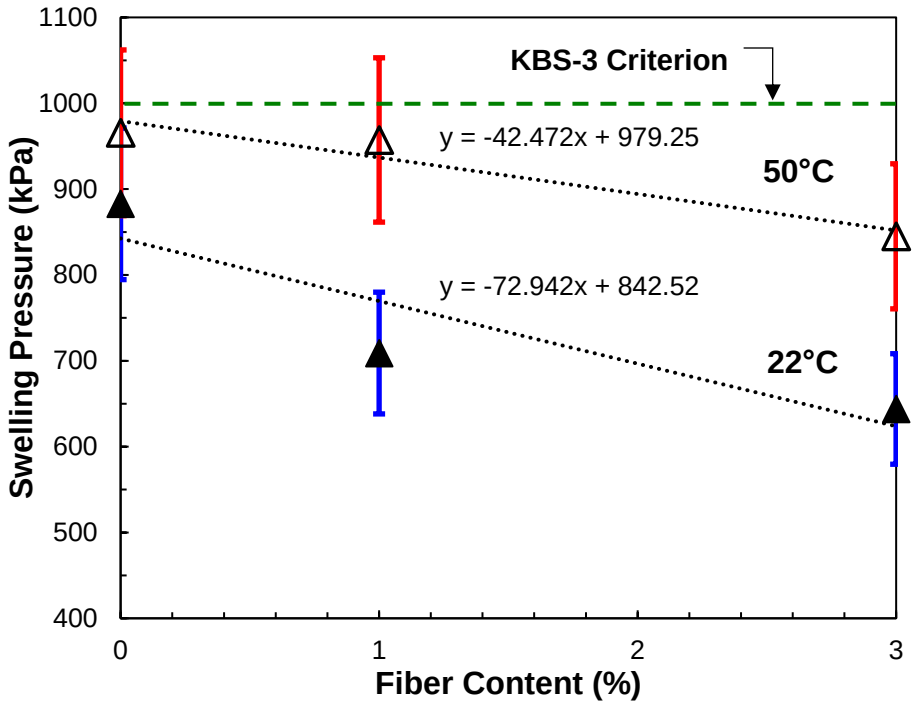

Figure 25. Swelling pressure vs. fiber content under room temperature (22°C) and elevated temperature (50°C).

The fiber-clustering network cannot be formed effectively brought by the notable spacing between the fibers, provided that only a minimal fiber content was added (Liu et al., 2021). However, by further increasing the fiber content, it was stated that a sufficient number of fibers could form a spatial network structure that induces an increasing bridging effect among the fibers and bentonite particles and results in a more significant swelling resistance; thus, reducing the swelling tendency of the bentonite due to increasing interfacial resistance among the fibers and the particles. Such findings were also indicated by other investigations (Viswanadham et al., 2009; Mukherjee & Mishra, 2019). In principle, the reduction in swelling pressure is caused by the interlocking of fibers and friction between the fibers and the bentonite particles in the bentonite mixture (Phanikumar & Singla, 2016).

3.4.3 EFFECT OF TEMPERATURE ELEVATION ON THE SWELLING PRESSURE

As seen in Figure 25, the temperature condition greatly affects the measured swelling pressure. Interestingly, the resulting swelling pressure for the elevated temperature data has shown an increase as compared to the ambient temperature data. For instance, the 0.0% fiber content group yielded a 9.4% increase in the swelling pressure from 22° to 50°C. Similarly, the measured swelling pressures between room and elevated temperatures at 1.0% and 3.0% fiber content differ by 35.0% and 31.2%, respectively.

According to Pusch et al. (1990), the temperature rise results in an increase in the osmotic pressure in the ionic or molecular system. This leads to an increase in the electric

double-layer repulsion and thickness within the Na-montmorillonite stacks, which entails an increase in the required pressure to maintain the constant volume of the system (i.e., swelling pressure). Moreover, it is energetically favorable for the clay to swell at higher temperatures due to the entropy gained by counterions that are liberated during swelling (Hansen et al., 2012).

Similar results showing the rise in swelling pressure along with the temperature for Na-bentonite have been documented by other researchers (Bag & Rabbani, 2017; Ye et al., 2013). However, in the case of Ca-bentonite, Kim et al. (2021) reported less swelling pressure values at higher temperatures. As stated by Pusch et al. (1990), the swelling behavior of the bentonite at elevated temperatures mainly depends on the type of predominant cation present in the exchange complex. It was also mentioned that with an increase in the swelling pressure for Na-bentonite and a decrease for Ca-bentonite at higher temperatures, this occurrence translates to two different phenomena: the increase in osmotic pressure for monovalent cations (e.g., Na^{+}) and lattice breakdown for divalent cations (e.g., Ca^{2+}).

It is noteworthy to mention that this research has addressed the behavior of the bentonite only until the 50°C elevated temperature. As a result, limited information can be drawn from this study. This elevated temperature was specifically chosen only for baseline assessment and prediction of the swelling and compressibility behavior of the bentonite. Therefore, it is suggested to conduct further studies with extreme temperatures (e.g., 150° to 200°C) to validate these phenomena and their impacts on the buffer material for appropriate nuclear repository design in the future.

3.4.4 ONE-WAY ANOVA

Statistical analysis such as the One-way Analysis of Variance (ANOVA) is performed to determine whether the means of two or more independent groups are significantly different or not. One-way ANOVA is considered an omnibus test statistic and cannot determine which specific groups were statistically significantly different from each other. This statistical analysis can only tell that at least two groups were statistically significantly different. Using the Microsoft Excel Analysis ToolPak Add-in, the one-way ANOVA was carried out under the 95% confidence level ($\alpha = 0.05$). The tables below present the results of the one-way ANOVA for the swelling pressure values. Here, the following legends are defined as:

- SS: sum of squares
- df: degrees of freedom
- MS: mean sum of squares
- F: F-statistic
- P-value: the probability of finding the observed results when the null hypothesis is true
- F crit: F critical value (value of the F-statistic at the threshold probability of mistakenly rejecting a true null hypothesis of Type I error)

In the following analyses, the null hypotheses are:

1. The addition of fibers has no statistically significant effect on the swelling pressure.
2. The elevated temperature has no statistically significant effect on the swelling pressure.

Table 5. One-way ANOVA results for the fiber effect on the 22°C dataset.

Source of Variation	SS	df	MS	F	P-value	F crit
Between Groups	111554.37	2	55777.19	2.2631	**0.1852**	5.1432
Within Groups	147877.57	6	24646.26			
Total	259431.94	8				

Table 6. One-way ANOVA results for the fiber effect on the 50°C dataset.

Source of Variation	SS	df	MS	F	P-value	F crit
Between Groups	13502.99	2	6751.49	0.3353	**0.7277**	5.1432
Within Groups	120810.29	6	20135.05			
Total	134313.27	8				

Table 7. One-way ANOVA results for the temperature effect on the 0.0% fiber dataset.

Source of Variation	SS	df	MS	F	P-value	F crit
Between Groups	10353.43	1	10353.43	0.4343	**0.5459**	7.7086
Within Groups	95367.10	4	23841.77			
Total	105720.53	5				

Table 8. One-way ANOVA results for the temperature effect on the 1.0% glass fiber dataset.

Source of Variation	SS	df	MS	F	P-value	F crit
Between Groups	92427.20	1	92427.20	5.2683	**0.0834**	7.7086
Within Groups	70175.84	4	17543.96			
Total	162603.04	5				

Table 9. One-way ANOVA results for the temperature effect on the 3.0% glass fiber dataset.

Source of Variation	SS	df	MS	F	P-value	F crit
Between Groups	105340.15	1	105340.15	4.0851	**0.1133**	7.7086
Within Groups	103144.92	4	25786.23			
Total	208485.07	5				

The first null hypothesis corresponds to the statistical analyses shown in Tables 5 and 6 while the second null hypothesis corresponds to the statistical analyses presented in Tables 7 to 9. With all the p-values greater than 0.05, the F-statistic was less than the F critical value. Hence, they fail to reject the null hypotheses offered. Therefore, it is concluded that there were no statistically significant differences between the group means as determined by the one-way ANOVA, stating that neither the fiber effect nor the temperature elevation has a statistically significant difference in the swelling pressure.

3.4.5 COMPRESSION (C_c) AND SWELLING INDICES (C_s)

The e-log p graph (Figure 26) shows the compression and decompression paths for 0.0%, 1.0%, and 3.0% fiber content under room and elevated temperatures. The obtained values of C_c for 0.0%, 1.0%, and 3.0% fiber content at 22° and 50°C are tabulated in Table 10 while the dataset for C_s are shown in Table 11. Figure 27 is provided to visualize the measured C_c and C_s values. In this plot, an increase in the fiber content would lead to a decrease in the compression and swelling indices. It is worth noting that the reduction in both indices is more pronounced at 3.0% fiber content. Given the low percent changes of C_c and C_s from 0.0% to 1.0% fiber content, it can be inferred that the 1.0% glass fiber content has a minor impact on the compressibility of the bentonite. On the other hand, given more significant reduction in these indices for the 3.0% fiber content, it is concluded that this amount of fiber degrades the compressibility behavior of the sample. These findings are consistent with the previous discussion on the effect of fiber inclusion on the swelling pressure.

Considering the effect of temperature elevation, it is also shown in Figure 27 that the temperature elevation leads to an increase in both C_c and C_s. The heat-induced increase in these indices results in the improvement of the compressibility characteristics of the bentonite mixture. As a result, the bentonite mixture would compress more under the same consolidation pressure when subjected to elevated temperature.

In summary, at higher temperature, the following parameters had increased: swelling pressure, C_c, and C_s. Therefore, the compressibility data are in good agreement with the swelling pressure data at room and elevated temperatures. With the trend

consistency, both the swelling and compressibility characteristics of the bentonite validate distinct behaviors under the influence of fiber reinforcement and temperature elevation.

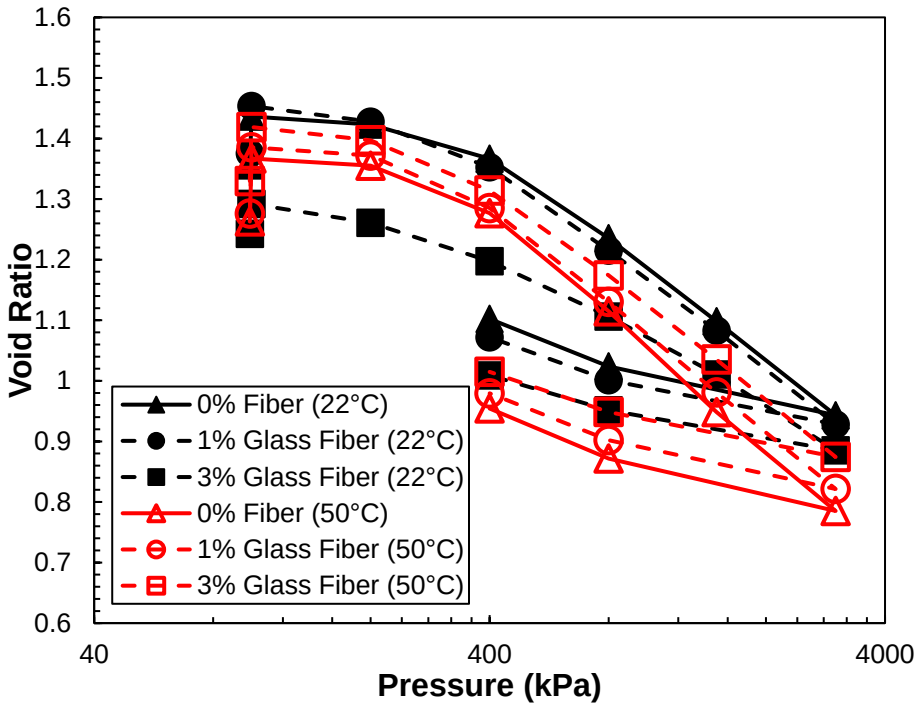

Figure 26. Void ratio vs. pressure to determine the compression index, C_c, and swelling index, C_s, for 0.0% fiber, 1.0% glass fiber, and 3.0% glass fiber under room temperature (22°C) and elevated temperature (50°C).

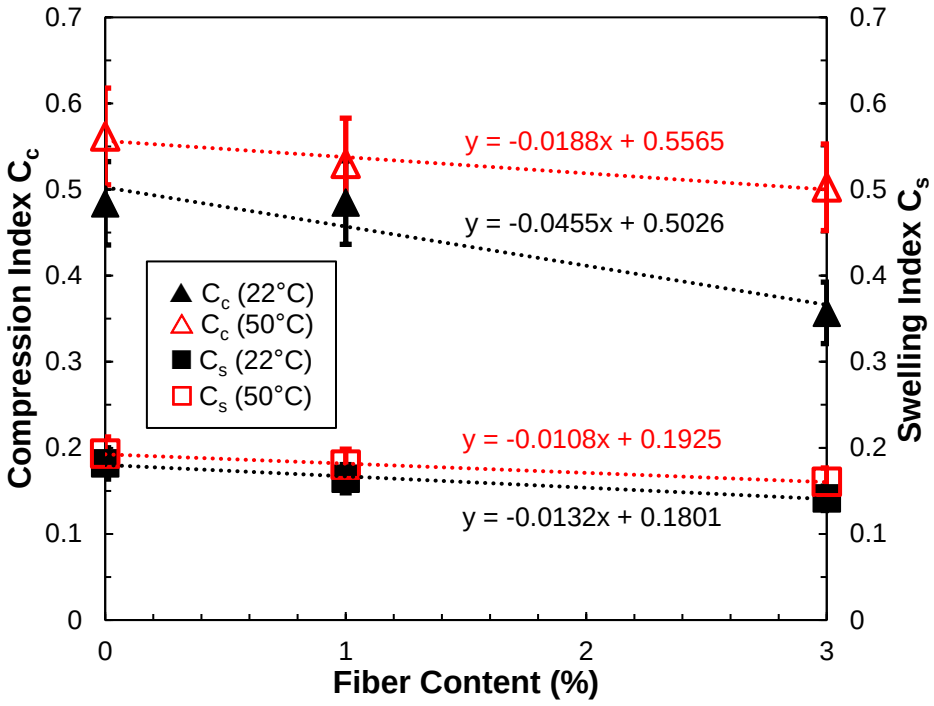

Figure 27. Compression and swelling indices (C_c and C_s) vs. fiber content under room temperature (22°C) and elevated temperature (50°C).

Table 10. Compression index (C_c) obtained from the consolidation tests.

Compression Index (C_c)		
Fiber Content	Temperature	
	22°C	50°C
0.0%	**0.484**	**0.562**
1.0%	**0.485**	**0.530**
3.0%	**0.357**	**0.503**

Table 11. Swelling index (C_s) obtained from the consolidation tests.

Swelling Index (C_s)		
Fiber Content	Temperature	
	22°C	50°C
0.0%	**0.182**	**0.193**
1.0%	**0.164**	**0.180**
3.0%	**0.141**	**0.161**

3.4.6 COEFFICIENT OF VOLUME COMPRESSIBILITY (m_v) AND COEFFICIENT OF CONSOLIDATION (c_v)

Figure 28a plots the coefficient of volume compressibility (m_v) at each consolidation pressure for all testing groups. At the lower range of applied vertical pressure, the m_v exhibits an increasing trend. At this instance, the void ratio is considerably high due to the sample's initial condition. As the consolidation pressure increases, the void ratio vastly decreases, translating to a greater reduction in the void ratio. While this happens, the m_v reaches its peak, and an inflection on the curve has been observed. From this point onwards, the m_v decreases as the consolidation pressure continues to increase. Dutta and Mishra (2017) reported the similar trend of m_v, showing the reliability of the research findings.

In order to compare the m_v values corresponding to each testing condition, a certain applied vertical pressure can be considered. For instance, at 800 kPa consolidation pressure, the measured m_v with respect to the fiber content under ambient (22°C) temperature are as follows: 1.48×10^4 (0.0%), 1.38×10^4 (1.0%), and 1.07×10^4 m^2/kN

(3.0%). On the other hand, the calculated m_v for each fiber content under elevated (50°C) temperature at the same consolidation pressure are the following: 1.95×10^4 (0.0%), 1.85×10^4 (1.0%), and 1.61×10^4 m^2/kN (3.0%). Clearly, for both temperature conditions, the reduction in m_v is evident along with the increase in fiber content. Meanwhile, for all fiber contents, the temperature elevation leads to a corresponding increase in m_v.

In this parameter, the key concept that governs in this situation is the thickness of the diffuse double layer. Given that the diffuse double layer thickness increases as the temperature increases, the sample undergoes a higher compression due to the increase in consolidation pressure, resulting in a higher m_v. The similar trend of m_v was also observed in the swelling and compressibility parameters, which validates the presented physical interpretation on the diffuse double layer.

Another compressibility parameter measured in this study is the coefficient of consolidation (c_v). The c_v at each consolidation pressure for all testing groups are visualized in Figure 28b. From the said plot, it was observed that the c_v follows a decreasing trend over the range of applied vertical pressure. In essence, the rate at which the specimen experiences consolidation diminishes as the vertical pressure increases. Vadlamudi and Mishra (2018) also stated that c_v is dependent on the rate at which water can expel out of the compacted sample for a given load increment. Similar decreasing trend of c_v was observed for higher bentonite content (Vadlamudi & Mishra, 2018) and essentially, this research reflects the same observation since the samples consist of mostly bentonite.

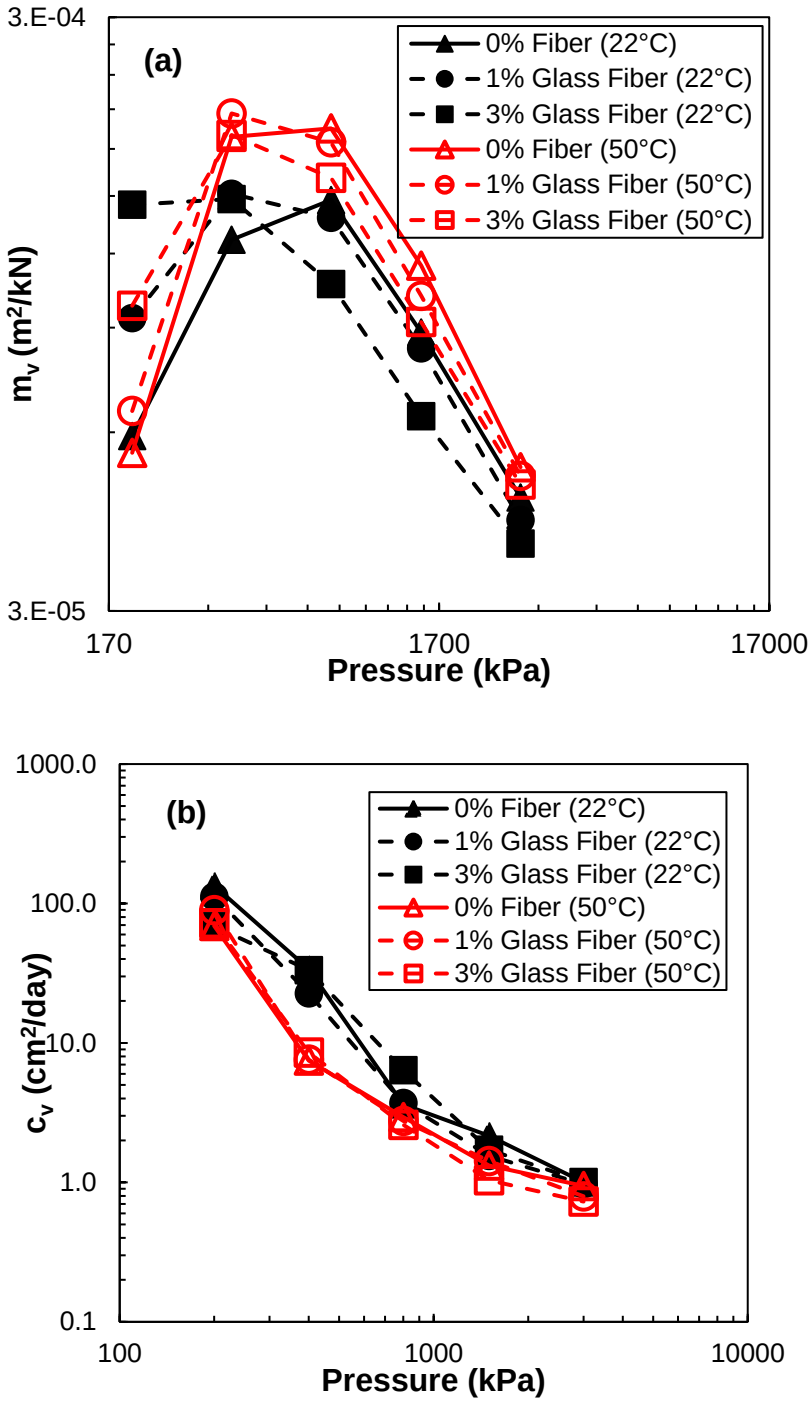

Figure 28. (a) Coefficient of volume compressibility, m_v, and (b) coefficient of consolidation, c_v, for 0.0% fiber, 1.0% glass fiber, and 3.0% glass fiber under room temperature (22°C) and elevated temperature (50°C).

At the 800 kPa vertical pressure, the following values of c_v in terms of fiber content for room (22°C) temperature are: 3.62 (0.0%), 3.72 (1.0%), and 6.38 cm^2/day (3.0%). Meanwhile, at the same vertical pressure, the calculated c_v under elevated (50°C) temperature for each fiber content are as follows: 2.94 (0.0%), 2.76 (1.0%), and 2.59 cm^2/day (3.0%). From these data, it can be inferred that the fiber content does not significantly affect the c_v since there was no distinct trend of the values observed regardless of the temperature condition. However, in terms of temperature elevation, a clear drop on the c_v has been observed from 22° to 50°C for each corresponding fiber content. As mentioned in the swelling pressure discussion, the increase in swelling pressure is caused by the increase in electric double-layer repulsion. According to Dutta and Mishra (2017), the clay plates move to a closer distance to each other due to an increase in the consolidation pressure. This occurrence leads to an increase in the repulsion of the electric double layer between these clay plates. When this phenomenon happens, the repulsion of the electric double layer slows down the movement of the clay plates; therefore, resulting in a decrease in c_v.

Physically speaking, when the bentonite particles are in contact with water, swelling occurs at that instance. Greater swelling results in a pathway blockage, leading to the reduction of flow rate. While the vertical stress is consequently increased, the voids are expected to collapse due to the tightness of the particles in the compacted mixture, resulting in lower c_v (Vadlamudi & Mishra, 2018). Given that higher swelling pressure is observed in the elevated temperature, the statement above is a possible physical manifestation of the significant drop in c_v for the 50°C.

3.4.7 HYDRAULIC CONDUCTIVITY (k)

Figure 29a shows the hydraulic conductivity at each consolidation pressure for all testing groups. All estimated hydraulic conductivities follow a decreasing trend with a corresponding increase in vertical pressure. It can also be seen that at the lower range of applied vertical pressure (i.e., 200 and 400 kPa), the hydraulic conductivity is higher for samples tested under room temperature than the elevated temperature. For instance, at 400 kPa, the hydraulic conductivity values for 22°C are the following: 4.1×10^{-4} (0.0%), 3.5×10^{-4} (1.0%), and 4.8×10^{-4} cm/day (3.0%). On the other hand, under 50°C temperature, the estimated hydraulic conductivity values are as follows: 1.4×10^{-4} (0.0%), 1.5×10^{-4} (1.0%), and 1.6×10^{-4} cm/day (3.0%). With these values, it is evident that the fiber content does not significantly affect the hydraulic conductivity of bentonite. However, a significant decrease in this parameter is observed when the temperature is increased. According to De Camillis et al. (2017), in situations where the diffuse double layer thickness is increasing, the swelling ability is increased while the permeability is decreased. This inverse relationship between swelling and permeability can be a guiding point for this analysis. Recalling the swelling pressure discussion, higher swelling is observed for elevated temperature. Hence, having lower hydraulic conductivity values for 50°C shows the consistency of this idea in regard to the swelling pressure of the bentonite. For higher vertical pressures, the estimated hydraulic conductivities are relatively similar to each of the presented dataset. This shows that for extremely higher range of pressure, neither the fiber content nor temperature elevation significantly affects the hydraulic conductivity of the bentonite.

Figure 29b presents the hydraulic conductivity vs. the measured void ratio. In this figure, all testing cases show an increasing hydraulic conductivity along with an increasing void ratio. Interestingly, with the void ratio values of less than 1.3, the estimated hydraulic conductivities are generally slightly higher for elevated temperatures as compared to the room temperature. Higher void ratio results to the hydraulic conductivity values being comparable, despite the fiber inclusion and temperature elevation. Limiting values for liner (1×10^{-7} cm/s or 8.6×10^{-3} cm/day) and buffer material (1×10^{-12} m/s or 8.6×10^{-6} cm/day) are proposed by Hauser et al. (2001) and SKB (2011), respectively. These recommended hydraulic conductivity values aid in limiting the advective transport for containment and retardation. As seen in Figure 29b, all testing cases qualify as landfill liner material and therefore can be recommended for usage. However, for the nuclear waste repository, these testing groups may be capable of acting as a buffer material if subjected to a stress of at least 2000 kPa, in terms of hydraulic conductivity.

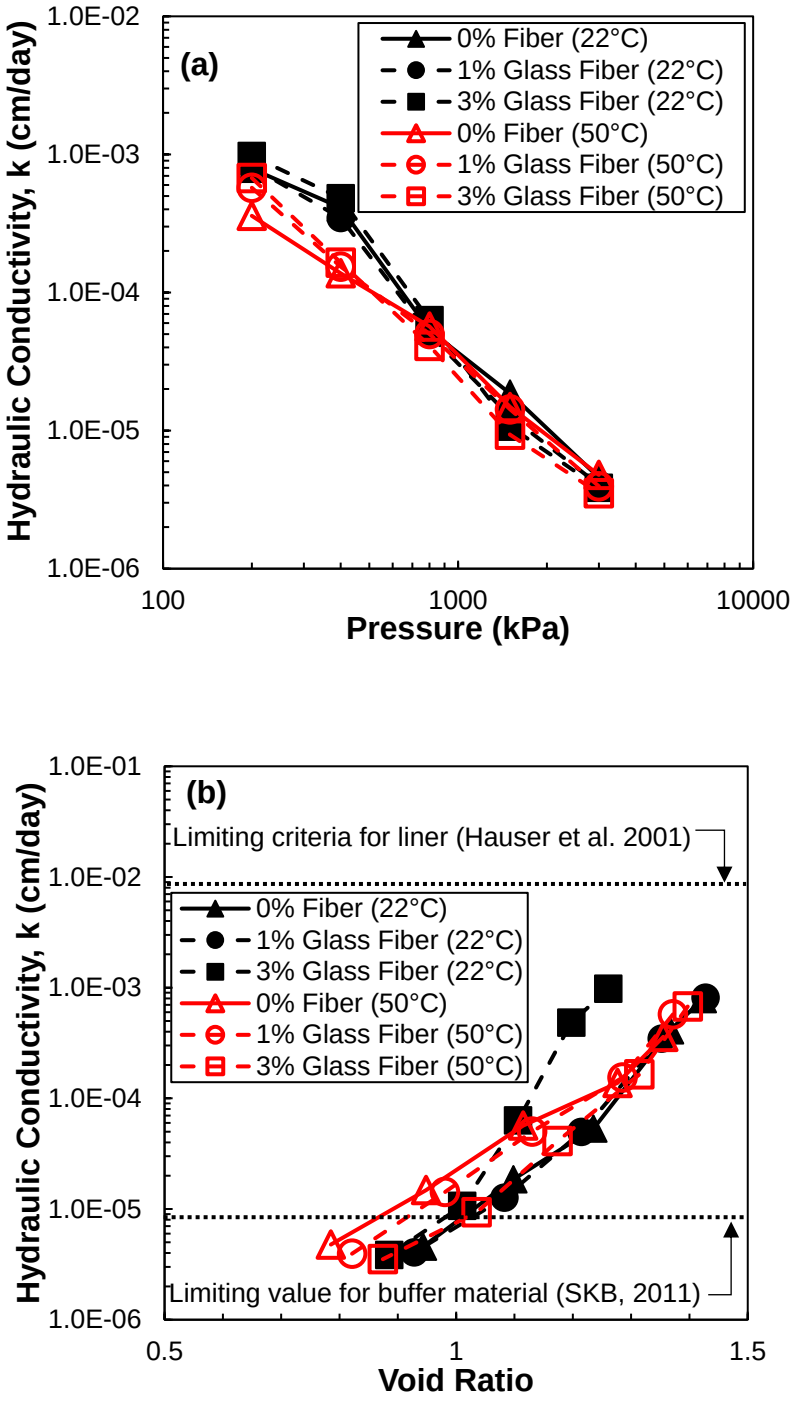

Figure 29. Hydraulic conductivity vs. (a) pressure and (b) void ratio for 0.0% fiber, 1.0% glass fiber, and 3.0% glass fiber under room temperature (22°C) and elevated temperature

(50°C). Hauser et al. (2001) proposed a limiting value of the hydraulic conductivity for liner and SKB (2011) for buffer material.

Lastly, it is noteworthy to mention that all of the hydraulic conductivity values are pure estimations only based on the aforementioned derived equation. Therefore, it is highly suggested to perform appropriate hydraulic conductivity tests to obtain the actual laboratory data for further analysis, verification, and recommendation on various engineering applications.

3.5 SUMMARY

Bentonite is used in several engineering applications such as grouting, barrier material for landfills, and buffer material for the nuclear waste repository. Although it has exceptional properties like high swelling capacity and low permeability, temperature elevation may severely affect these characteristics and may lead to the presence of desiccation cracking. To address this concern, inorganic microfibers such as glass fiber, which are known to be capable of mitigating such a situation, are proposed as a reinforcement material for compacted bentonite. In this chapter, the swelling and compressibility behavior of unreinforced and inorganic microfiber-reinforced bentonite under room (22°C) and elevated (50°C) temperatures were investigated.

Through the one-dimensional consolidation tests, the following parameters were obtained for each testing condition: swelling pressure, C_c, C_s, m_v, c_v, and hydraulic

conductivity. Based on the experimental data and their respective analyses, the following conclusions can be drawn:

1. Under ambient temperature conditions, the recorded swelling pressure values for 0.0%, 1.0%, and 3.0% fiber content are the following: 883, 709, and 644 kPa, respectively. On the other hand, under elevated temperature conditions, the measured swelling pressure values for the same set of fiber content are as follows: 966, 957, and 845 kPa, respectively. Due to the fiber reinforcement, a reduction in swelling pressure was observed. As the fiber content in the bentonite mixture increases, the resulting swelling pressure consistently decreases.
2. Given the values mentioned above, the application of temperature elevation contributes to a significant rise in the swelling pressure for all testing conditions with respect to the fiber content.
3. Compressibility characteristics such as C_c and C_s are affected by both fiber content and temperature elevation. Based on the values of the indices, the fiber inclusion reduces both C_c and C_s, signifying the degradation in the compressibility behavior of the bentonite. However, the temperature elevation gives an increase to both indices, suggesting the improvement of the compressibility characteristics of the bentonite.
4. With the similar trends in the swelling pressure, C_c, and C_s, the data consistency affirms the distinct behaviors of the swelling and compressibility of the bentonite under the influence of fiber reinforcement and temperature elevation.
5. Other compressibility parameters discussed in this paper are the m_v and c_v. At a certain consolidation pressure, the fiber inclusion results in a lower m_v while the

temperature elevation leads to a higher m_v. These observed trends in terms of fiber content and temperature elevation are consistent with that of the swelling pressure, C_c, and C_s.

6. On the other hand, no distinct trend in the c_v with respect to the fiber content was found, concluding that the fiber content does not significantly affect the said compressibility parameter. Nevertheless, the temperature elevation causes a reduction in the calculated c_v values.
7. For the lower range of pressure values, the estimated hydraulic conductivity values are smaller only for elevated temperature conditions and fiber inclusion does not significantly affect this parameter. For the higher range of pressure values, all testing results show similar values and suggest that neither fiber inclusion nor temperature elevation affects the hydraulic conductivity. Lastly, these are all estimated values and are subject to further verification after obtaining experimental hydraulic conductivity data.

CHAPTER 4. EVALUATION OF SHEARING BEHAVIOR OF INORGANIC MICROFIBER-REINFORCED BENTONITE

This chapter of the thesis is subject for journal submission.

4.1 OBJECTIVES

In this chapter, the shearing behavior of the glass fiber-reinforced bentonite was investigated by conducting a series of direct simple shear tests on the bentonite samples. From this laboratory experiment, shear strength parameters such as cohesion and friction angle were evaluated for both peak and residual strengths. Further analysis of other parameters such as the normalized shear stress and stress paths were also considered in this section. Lastly, the Modified Cam Clay Model was used to know the sample's behavior under the critical state by considering the effect of fiber reinforcement on the yield surface. Through this task, the applicability of the glass fiber-reinforced bentonite can be confirmed to be used as an engineering barrier material in terms of the shear strength aspect.

4.2 MATERIALS

The experimental study employs the same materials mentioned in the previous chapter: granular Na-bentonite (BENSEAL®, Houston, Texas) and glass fibers (158B Type 30™, Toledo, Ohio) in 12-mm lengths. The cut microfibers were reinforced to the bentonite samples in 1.0%, 2.0%, and 3.0% by weight.

4.3 METHODOLOGY

4.3.1 SPECIMEN PREPARATION

As stated in the previous chapter, a similar procedure for specimen preparation was done for this chapter. The glass fibers were cut in 12-mm lengths before being mixed with Na-bentonite and DI water. It is important to note that this fiber length is appropriate in terms of the geometrical limitation of the specimen size and does not cause a lack of representativeness within the bentonite sample.

During the mixing part, the sample preparation assembly can be set up simultaneously. This assembly is specific for the direct simple shear test. Initially, the bottom end cap is attached to the bottom jig plate and affixed by a bolt. An 89-mm long membrane is placed on the bottom end cap and is extended down until the metal groove is covered. To keep this setup fixed, multiple O-rings were attached, covering the membrane and touching the entire height of the bottom end cap. Next is securing the 63.5-mm diameter steel rings in place. A total of 14 steel rings were stacked together, in addition to the top and bottom silver rings. The 3 notches at the silver rings were fastened with alignment screws to stack the steel rings. These stacked rings were placed on top of the O-rings, and the membrane inside the rings. The top end of the membrane was stretched over the assembled rings, surrounding the outside surface of the rings. This sample assembly is shown in Figure 30.

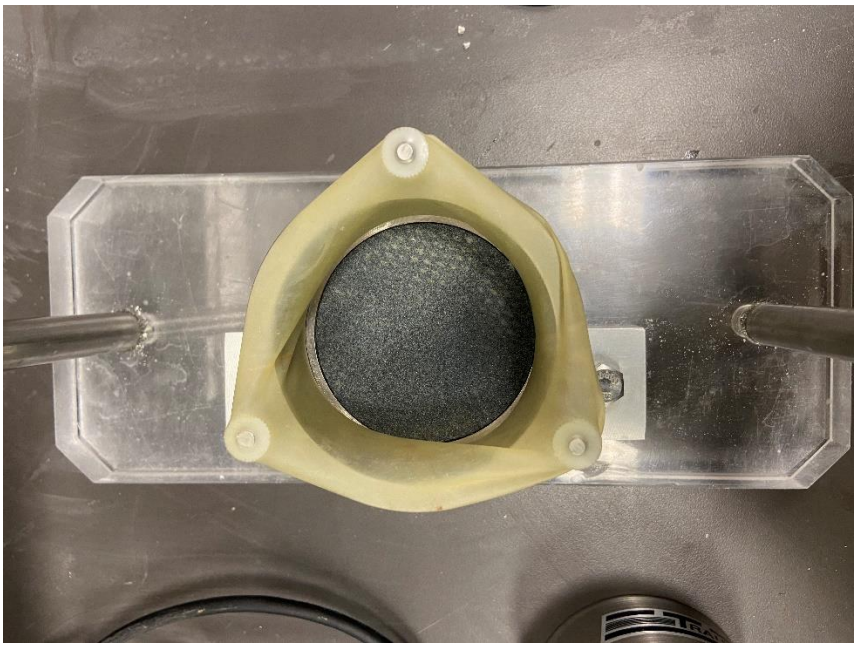

Figure 30. Specimen assembly with the bottom end cap, steel rings, and membrane installed in the bottom jig plate.

After manually mixing the bentonite, glass fibers (1.0%, 2.0% or 3.0% by weight), and DI water (35.0% moisture content) in a similar manner discussed previously, the mixture was placed in the membrane with steel rings. The sample was placed in 3 different layers as the compaction was performed. It is important to note that the compaction process for this test was done in the sample assembly. Although the compaction was not done in the compaction mold, it still followed the same compaction process indicated in the previous chapter. For direct simple shear tests, it is important to maintain a similar density across all samples to ensure the comparability of results. To obtain the dry density of each sample, the weight of the sample was recorded after it had occupied the entire volume of the steel rings. The resulting dry density of the samples is 1341 kg/m^3. Once the weight

was measured, the top end cap was placed on top of the specimen and the membrane outside the steel rings was pulled up to surround the entire height of the top end cap. Another O-ring was placed to the membrane and metal groove of the top end cap to secure the sample assembly. Lastly, the top jig plate was placed above the top end cap to ensure its alignment when the whole sample assembly is transferred to the direct simple shear device. The entire sample setup ready for installation in the direct simple shear device is presented in Figure 31.

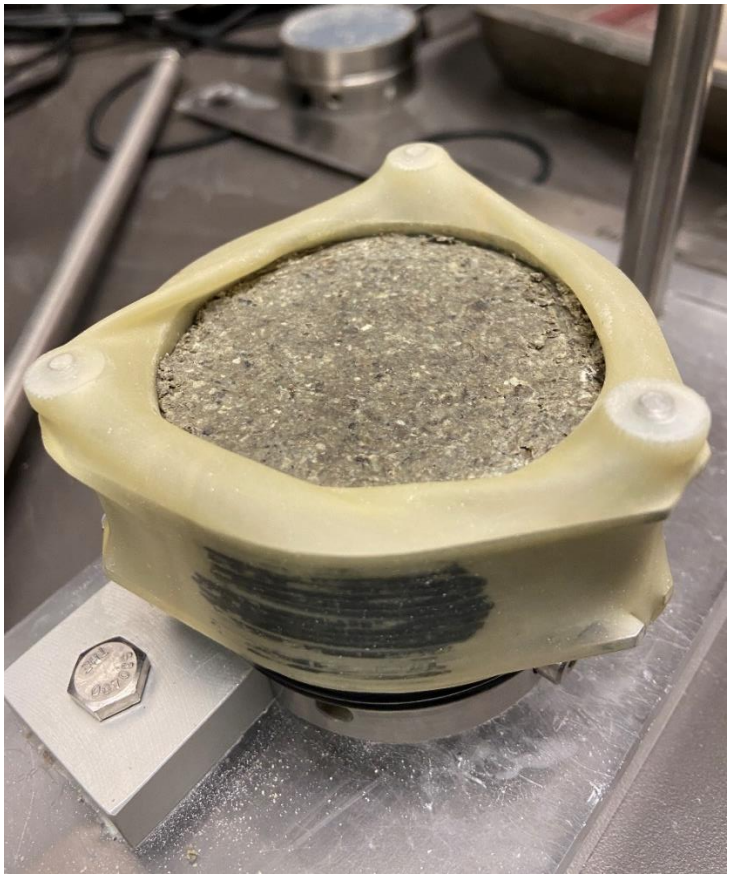

Figure 31. A prepared soil specimen prior to installation in the direct simple shear device.

4.3.2 DIRECT SIMPLE SHEAR TEST

In this chapter, the direct simple shear tests performed follows the ASTM D6528-17, Standard Test Method for Consolidated Undrained Direct Simple Shear Testing of Fine Grain Soils. Figure 32 shows the sample assembly installed in the direct simple shear device while Figure 33 illustrates the device setup for this test. For this purpose, GeoTAC DigiShear DSS System of Trautwein (Houston, Texas) was used to conduct the direct simple shear test.

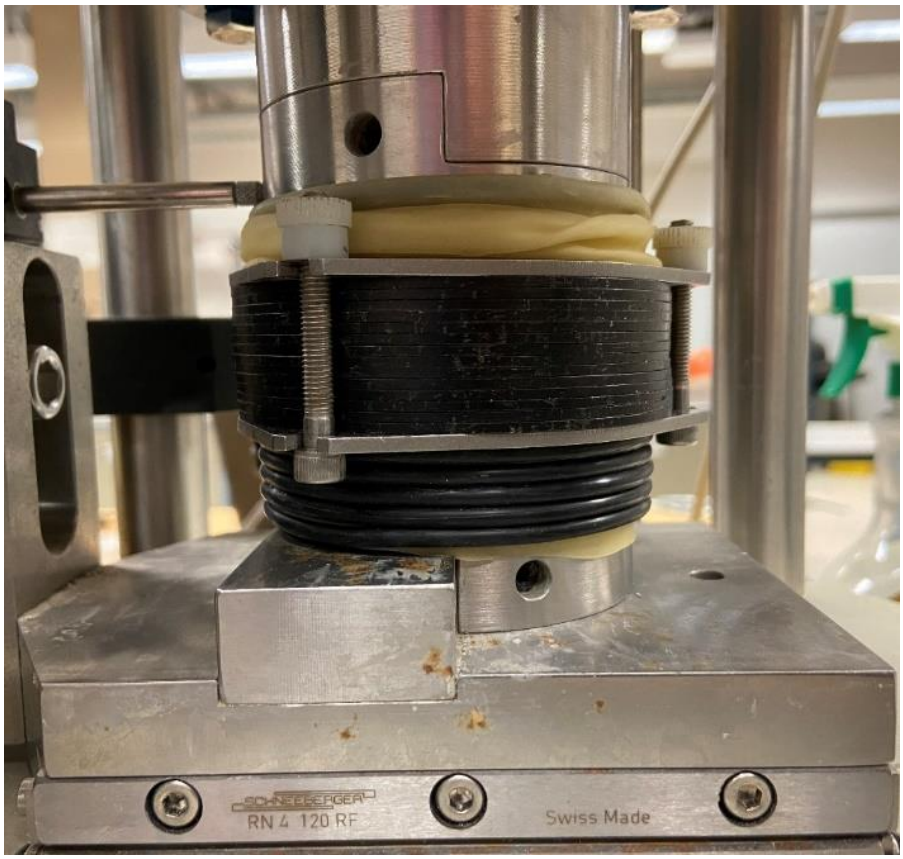

Figure 32. Sample assembly installed in the direct simple shear device.

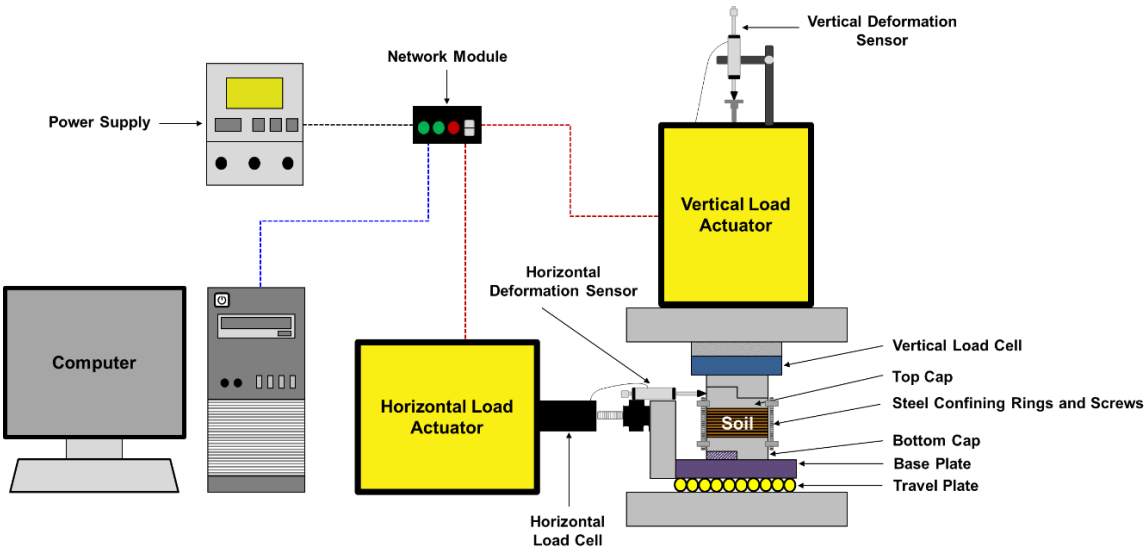

Figure 33. Direct simple shear test setup consisting of the horizontal and vertical actuators and load cells, network module, computer, and power supply.

The experimental program for direct simple shear tests consists of two main parts: the consolidation and shearing stages. Initially, the consolidation stage commenced when normal stress was applied. Depending on the vertical pressure of interest for each test run, the sample was subjected to different normal stresses: 50, 100, and 200 kPa. For a duration of 100 min, the deformation readings were measured every 30 s to ensure data accuracy. This consolidation period was set for all samples as it was observed that there was no further volume change beyond this time period.

Subsequently, the shearing stage started by keeping the applied normal stress from the end of the consolidation stage. A constant shearing rate of 1 mm/min was adapted from Fakharian & Evgin (1995) and Abbaspour et al. (2020). Shearing was carried out until a shear strain level of 25% was achieved. The induced shear stress was measured along with

its corresponding shear strain. In this test, two types of shear stress are deemed noteworthy: the maximum and residual shear stresses. From the shear stress vs. shear strain graph, the maximum shear stress signifies the peak strength behavior of the soil. On the other hand, the residual shear stress is the measured shear stress at the 25% strain level. At this strain level, large shear displacement is already observed. Furthermore, horizontal and vertical displacements were also recorded for the entire duration of the shearing stage. After the direct simple shear test was concluded, the soil samples typically show a similar manner of shearing, as presented in Figure 34. The direct simple shear test was done in triplicates per testing group to ensure data accuracy and the shear stress vs. shear strain data were averaged.

Figure 34. Soil sample after finishing the direct simple shear test (scale: 16 × 13 mm).

4.3.3 DETERMINATION OF SHEAR STRENGTH PARAMETERS

The two most notable shear strength parameters obtained from this test are cohesion (c) and friction angle (ϕ). With the shear stress (τ) values at peak and residual strength behaviors, these are plotted with respect to the applied normal stresses. Using the Mohr-Coulomb criterion on the experimental results, the equation of the best fit line is obtained, and this should follow the form:

$$\tau = c + \sigma \tan \phi \tag{9}$$

Two different best fit lines are generated: one for the peak strength and the other one for the large shear displacement. Essentially, the cohesion and friction angle for each strength behavior are calculated.

4.3.4 DERIVATION OF THE STRESS PATH

From the Mohr-Coulomb criterion, stress path is defined as the line connecting points of successive stress state experienced by soil specimen during the progress of a test. The following derivation of stress path is suggested by Lambe (1964).

$$p = \frac{\sigma_1 + \sigma_3}{2} \tag{10}$$

$$q = \frac{\sigma_1 - \sigma_3}{2} \tag{11}$$

where σ_1 is the major principal stress, σ_3 is the minor principal stress, p is the mean total stress, and q is the deviatoric stress.

The concept of deviatoric stress is similar to the shear stress in the Mohr's circle, and therefore, it can be said that these two parameters are equal. Rearranging Eq. (11), replacing q by τ, and σ_3 being known (i.e., 50, 100, 200 kPa), σ_1 can then be back-calculated.

$$\sigma_1 = 2\tau + \sigma_3 \tag{12}$$

Plugging this into Eq. (10), then the value of p is determined. To plot the stress path in the $p - q$ space, each point of measured shear stress (τ or q) from the direct simple shear test should correspond to the back-calculated mean total stress (p).

4.3.5 DERIVATION OF THE MODIFIED CAM CLAY MODEL PARAMETERS

In the previous chapter for one-dimensional consolidation, the soil only undergoes vertical deformation. Since lateral deformation is restricted due to the boundary conditions of the said experiment, the horizontal stress is considered the at-rest earth pressure, of which its coefficient is denoted as K_0. Extending the previous concepts of p and q in the one-dimensional condition, Eqs. (10) and (11) are transformed into:

$$p = (1 - K_0)\sigma_v \tag{13}$$

$$q = \frac{(1 + 2K_0)\sigma_v}{3} \tag{14}$$

$$K_0 = 1 - \sin\phi \tag{15}$$

where σ_v is the applied vertical stress from the one-dimensional consolidation test.

Aside from the $p - q$ space, the $v - \ln p$ space completes the information about the Critical State Soil Mechanics (Modified Cam Clay Model). The $v - \ln p$ is a derived from the void ratio vs. pressure in the logarithmic scale obtained from the one-dimensional consolidation test. The void ratio (e) is replaced by the specific volume (v), using the following equation:

$$v = 1 + e \tag{16}$$

The following procedure to calculate the parameters for the Modified Cam Clay Model is based on Dev et al. (2013).

1. With the one-dimensional consolidation test results, C_c and C_s can be obtained. Meanwhile, ϕ is provided by the direct simple shear test.
2. From the $v - \ln p$ graph, N_0 is taken as the specific volume at the 1 kPa unit pressure of the K_0 line.
3. The following calculations are made:

$$\lambda = \frac{C_c}{2.303} \tag{17}$$

$$\kappa = \frac{C_s}{2.303} \tag{18}$$

$$M = \frac{6 \sin \phi}{3 - \sin \phi} \tag{19}$$

where λ is the compression index in the Critical State Soil Mechanics, κ is the swelling index in the same area, and M is the slope of the Critical State Line (CSL). It is noteworthy that the ϕ at the critical state is assumed to be the friction angle at

the residual strength (i.e., 25% strain level), similar concept with the assumption made by Mukherjee & Mishra (2021).

4. The stress ratio (η_{K_0}) is computed using Eqs. (13) and (14):

$$\eta_{K_0} = \frac{3(1 - K_0)}{1 + 2K_0} \tag{20}$$

5. Given that the important parameters (N_0, λ, κ, M, and η_{K_0}) are solved, the specific volume at the 1 kPa unit pressure of the Normal Compression Line (NCL), or N, can be obtained. Since triaxial test was not performed, the NCL cannot be directly obtained. Thus, Eq. (21) shows the transformed equation for the case of one-dimensional consolidation.

$$N = N_0 + (\lambda - \kappa) \ln\left(\frac{M^2 + \eta_{K_0}^2}{M^2}\right) \tag{21}$$

6. Then, the specific volume at the 1 kPa unit pressure of the CSL, referred to as Γ, can be determined using Eq. (22).

$$\Gamma = N - (\lambda - \kappa) \ln 2 \tag{22}$$

7. Lastly, for the $p - q$ space, the equation of the yield surface is as follows:

$$q = Mp\sqrt{\frac{p_c}{p} - 1} \tag{23}$$

where p_c is the preconsolidation pressure determined from the one-dimensional consolidation test, and p is the normal stress.

4.4 RESULTS AND DISCUSSION

4.4.1 SHEAR STRESS

The consolidation phase of the direct simple shear test was performed so that the sample is stabilized with the specified normal stress applied. After 100 min, no further volume change of the sample was observed. For this purpose, Figures 35a to 35d present the deformation vs. time graphs for 0.0%, 1.0%, 2.0%, and 3.0% glass fiber with respect to the normal stresses 50, 100, and 200 kPa.

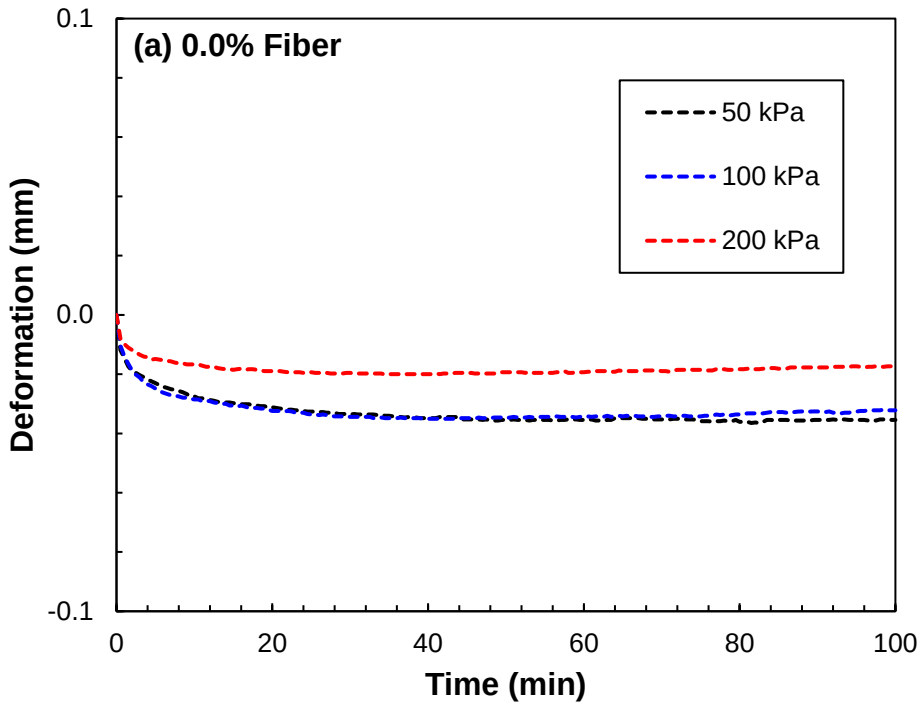

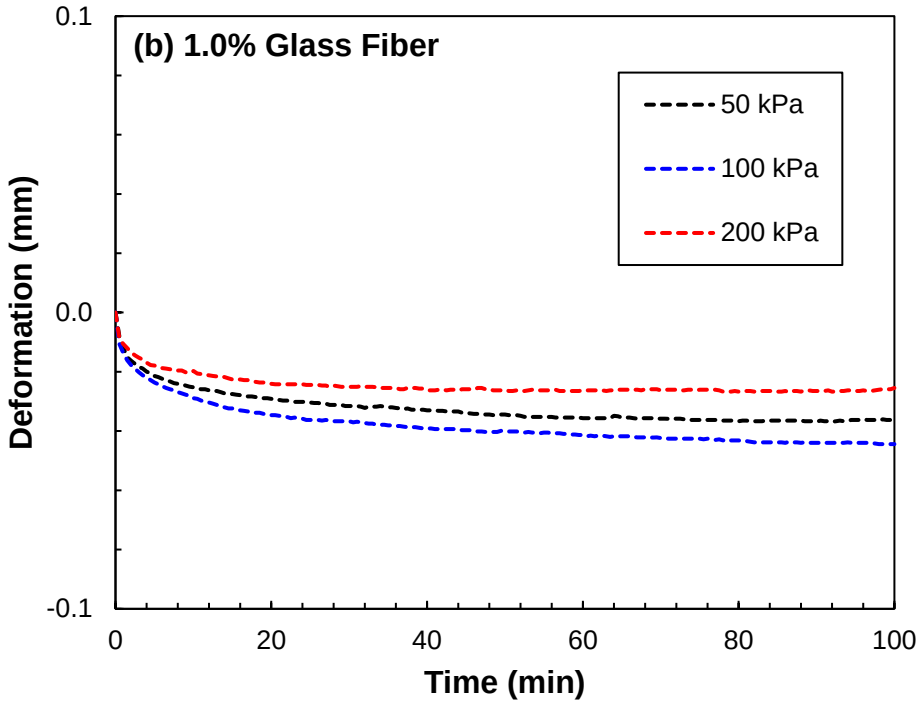
(b) 1.0% Glass Fiber
50 kPa
100 kPa
200 kPa
Deformation (mm)
0.1
0.0
-0.1
0
20
40
60
80
100
Time (min)

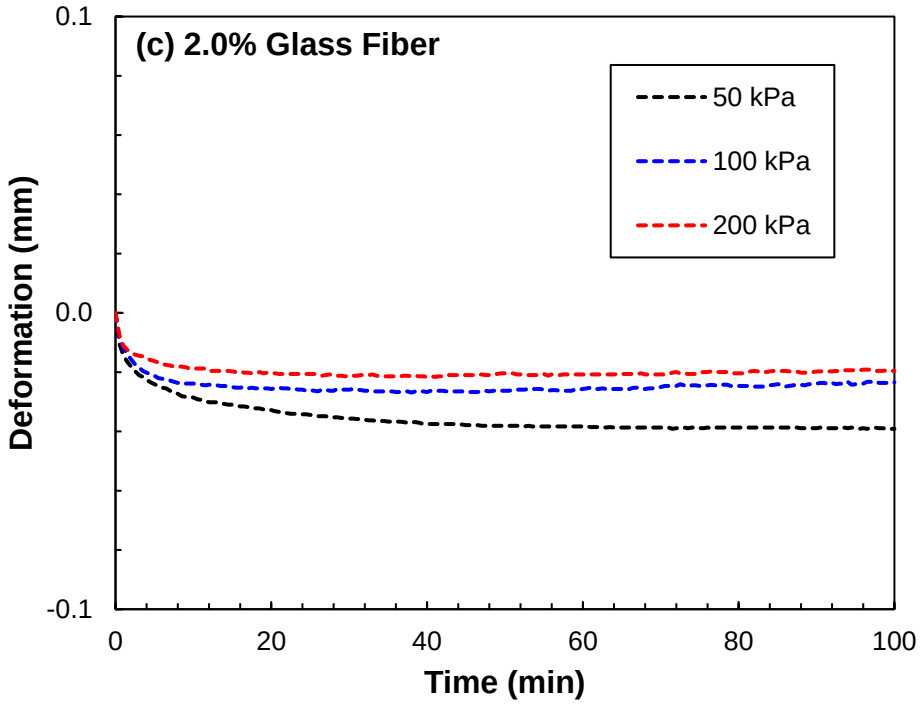
(c) 2.0% Glass Fiber
50 kPa
100 kPa
200 kPa
Deformation (mm)
0.1
0.0
-0.1
0
20
40
60
80
100
Time (min)

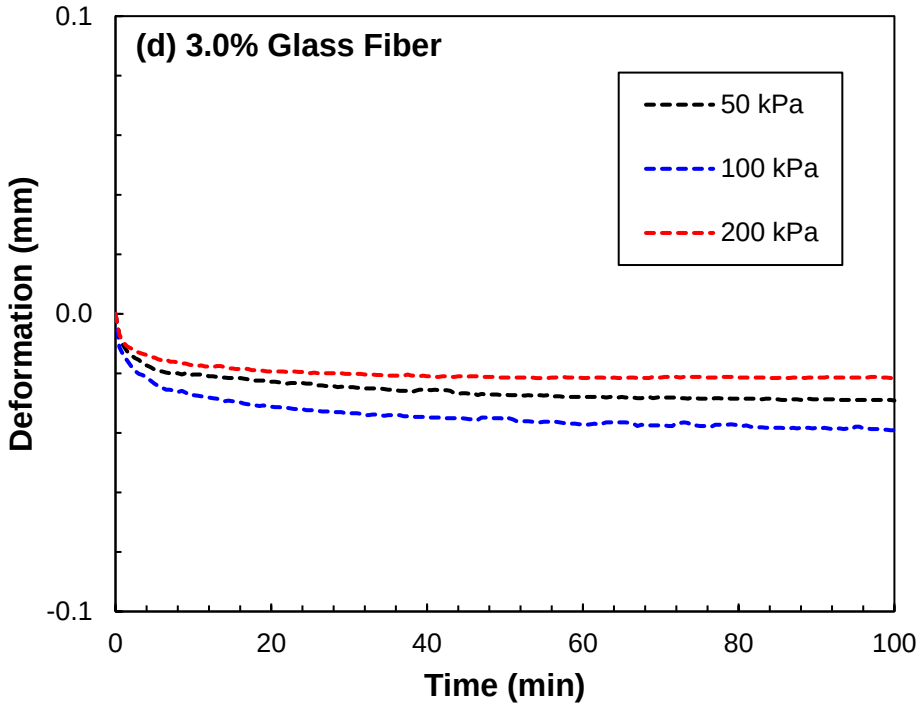

Figure 35. Deformation vs. time graphs for (a) 0.0%, (b) 1.0% glass fiber, (c) 2.0% glass fiber, and (d) 3.0% glass fiber during the consolidation phase.

During the shearing stage, the stress-strain relationships were monitored for the entire period. Illustrated in Figures 36a to 36d are the shear stress vs. shear strain graphs for each sample in varying fiber contents. It was observed that when the sample is subjected to higher normal stress, the resulting shear stress is also higher.

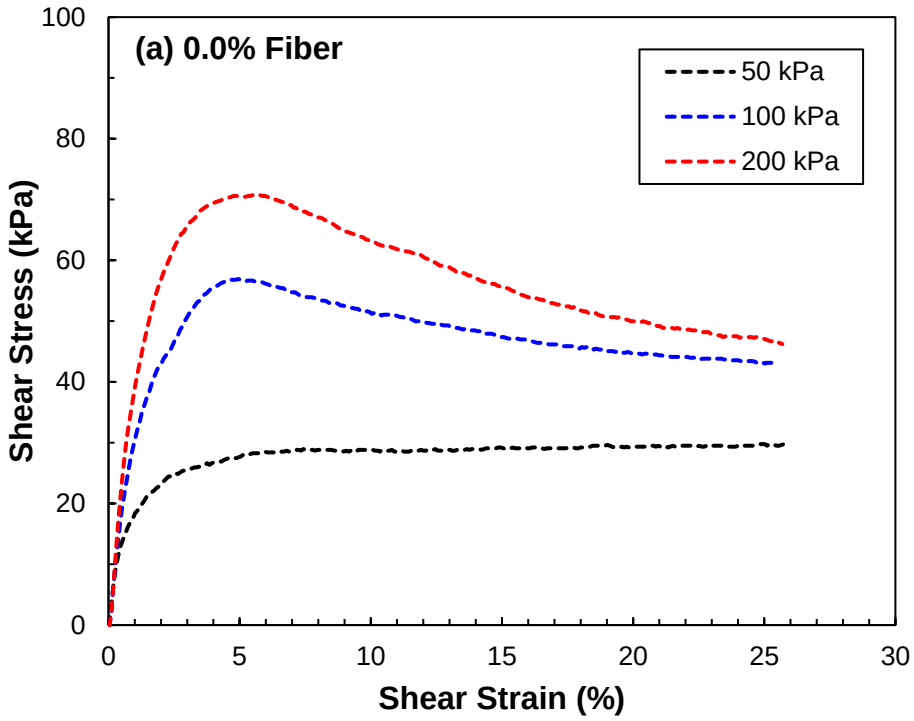
(a) 0.0% Fiber
50 kPa
100 kPa
200 kPa
Shear Stress (kPa)
Shear Strain (%)
0
20
40
60
80
100
0
5
10
15
20
25
30

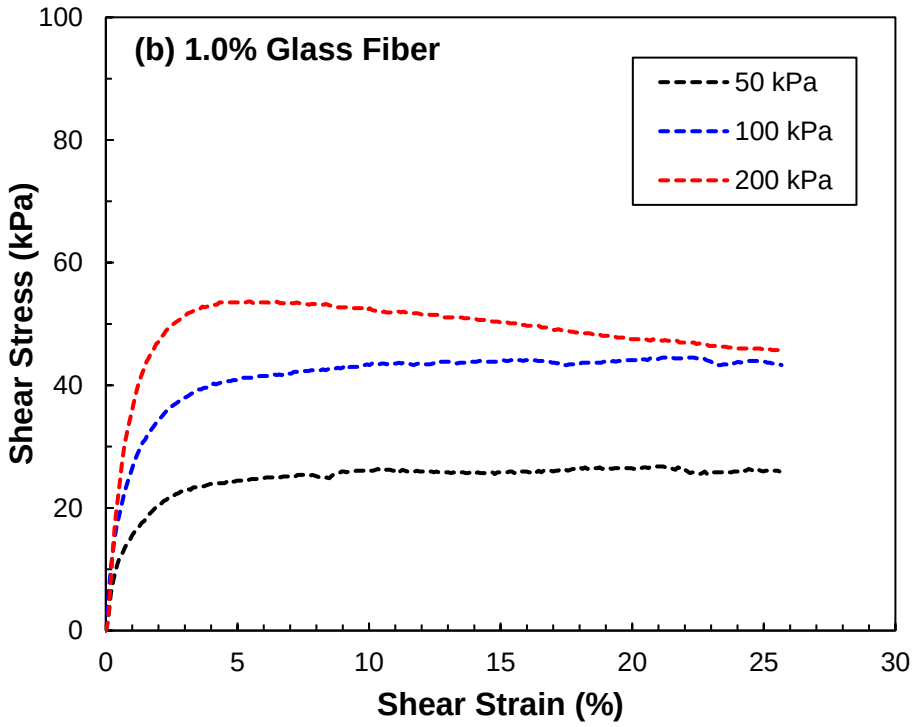
(b) 1.0% Glass Fiber
50 kPa
100 kPa
200 kPa
Shear Stress (kPa)
Shear Strain (%)
0
20
40
60
80
100
0
5
10
15
20
25
30

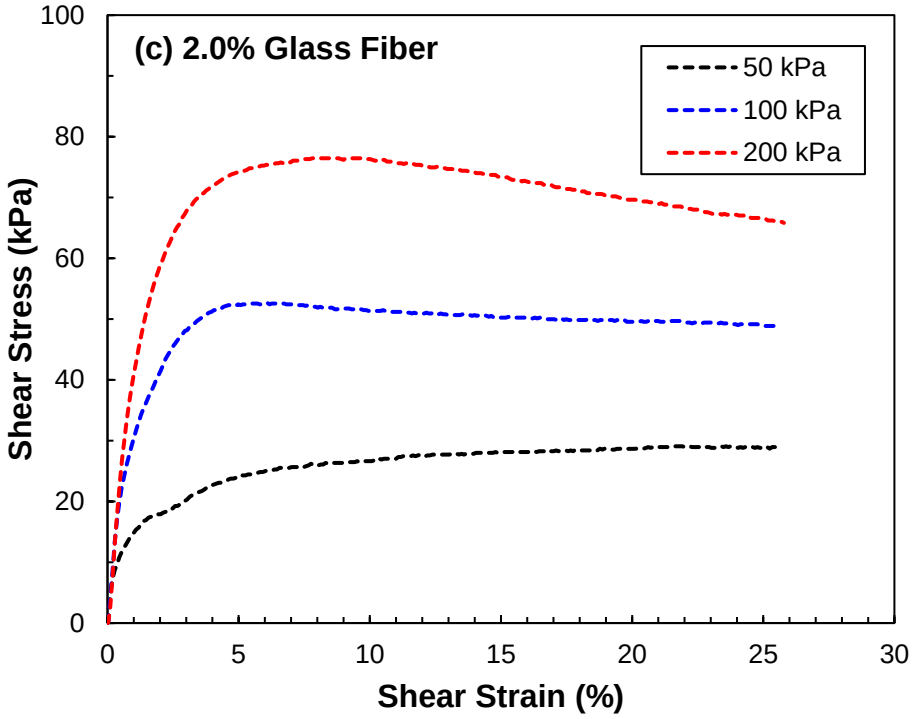
(c) 2.0% Glass Fiber
50 kPa
100 kPa
200 kPa
Shear Stress (kPa)
Shear Strain (%)
0
20
40
60
80
100
0
5
10
15
20
25
30

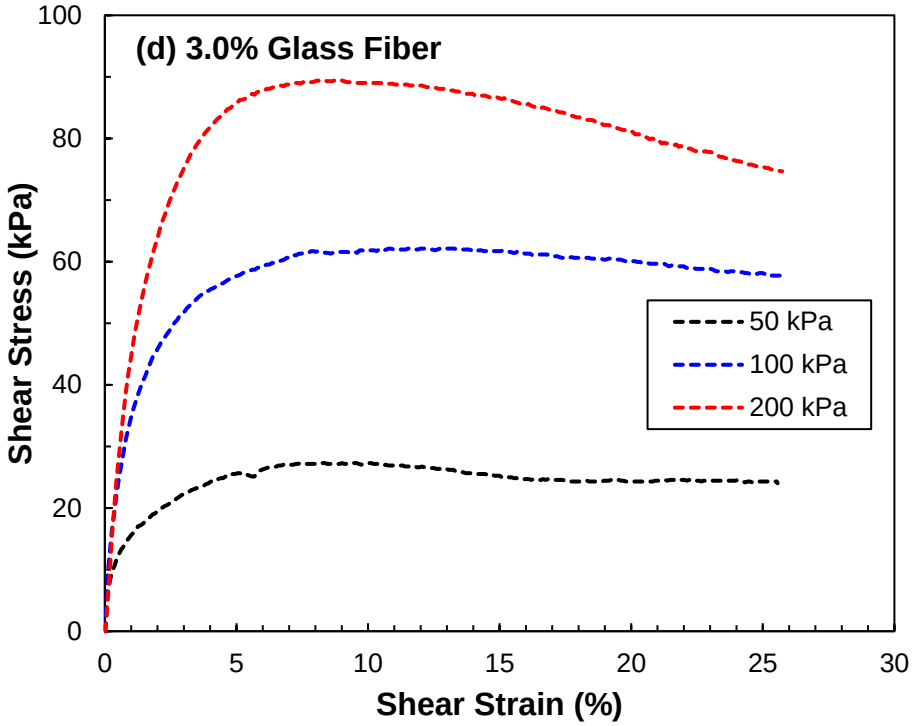
(d) 3.0% Glass Fiber
50 kPa
100 kPa
200 kPa
Shear Stress (kPa)
Shear Strain (%)
0
20
40
60
80
100
0
5
10
15
20
25
30

Figure 36. Shear stress vs. shear strain graphs for (a) 0.0%, (b) 1.0% glass fiber, (c) 2.0% glass fiber, and (d) 3.0% glass fiber during the shearing phase.

Interestingly, the 0.0% fiber samples showed a strain hardening at the 50 kPa normal stress until it approached to a constant shear stress. However, the 100 kPa and 200 kPa were showing a strain softening behavior after their peak shear stress. On the other hand, all 200 kPa tests for the reinforced conditions (1.0%, 2.0%, and 3.0%) resulted to a strain softening after the peak. The rest of the 50 kPa and 100 kPa data showed a strain hardening as it attains constant reading until the end of the shearing stage. The prolonged curve after the peak shows that the material has become more ductile and has undergone further plastic deformation, particularly at higher stress levels. The bridging effect of the fibers between the particles has been evident on the shear stress vs. shear strain curves for fiber-reinforced samples, especially after the peak value has been attained.

To better compare the effect of fiber reinforcement on the shear stress, Figures 37a to 37c were plotted to show the differences in the shearing behavior of unreinforced and reinforced samples for each confining stress. For the 50 kPa confining stress, all testing groups showed similar behavior of strain hardening and magnitudes of shear stress. For the 100 kPa and 200 kPa confining stresses, the 0% fiber illustrated a sharp post-peak decline on the shear stress. However, the reinforced samples for 1.0%, 2.0%, and 3.0% under the same high confining stresses showed sustained shear stress curves with gentler slopes, exhibiting the bridging effect of the fibers as mentioned earlier.

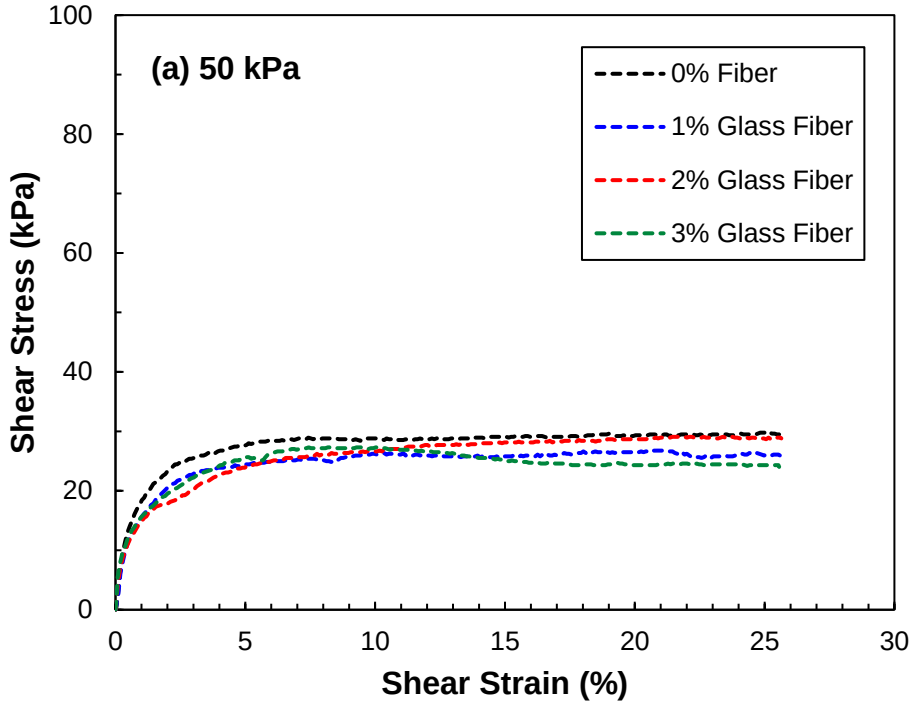
(a) 50 kPa
0% Fiber
1% Glass Fiber
2% Glass Fiber
3% Glass Fiber
Shear Stress (kPa)
Shear Strain (%)
0
20
40
60
80
100
0
5
10
15
20
25
30

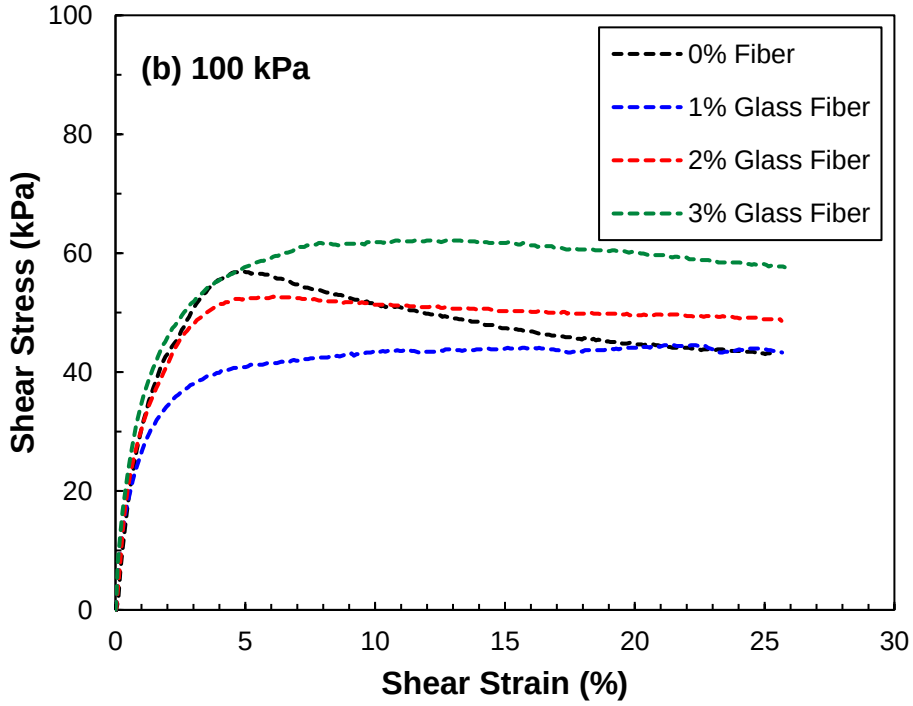
(b) 100 kPa
0% Fiber
1% Glass Fiber
2% Glass Fiber
3% Glass Fiber
Shear Stress (kPa)
Shear Strain (%)
0
20
40
60
80
100
0
5
10
15
20
25
30

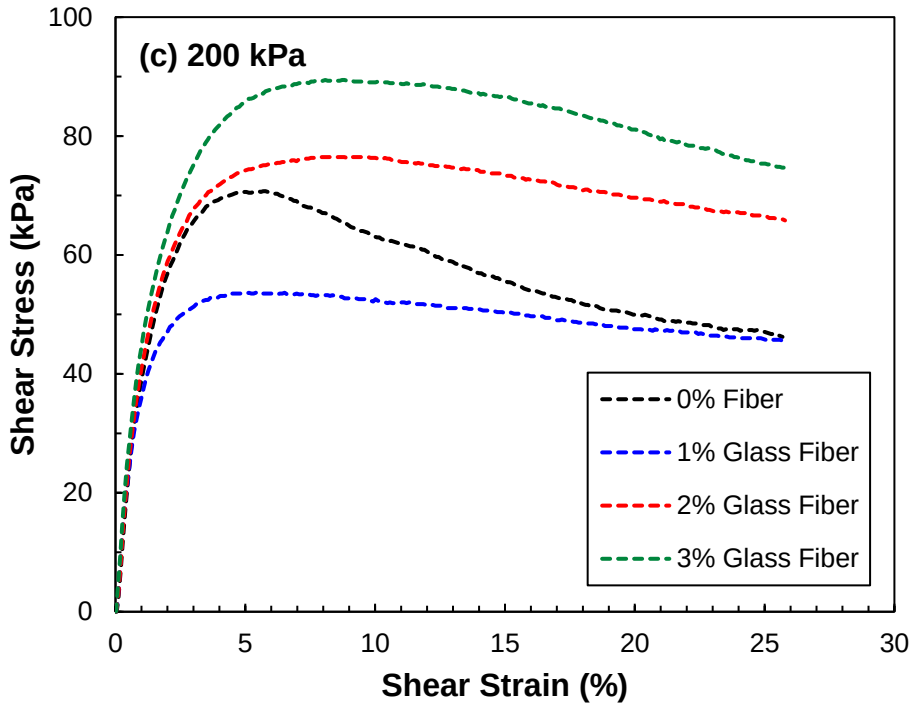

Figure 37. Shear stress vs. shear strain graphs for (a) 50 kPa, (b) 100 kPa, and (c) 200 kPa for different fiber contents during the shearing phase.

Another set of parameters that were measured in the entire duration of shearing is the displacement, specifically vertical and horizontal displacements, as shown in Figures 38a to 38d. Based on these measurements, the small vertical displacement change relative to the horizontal displacement confirmed the undrained condition of the test performed.

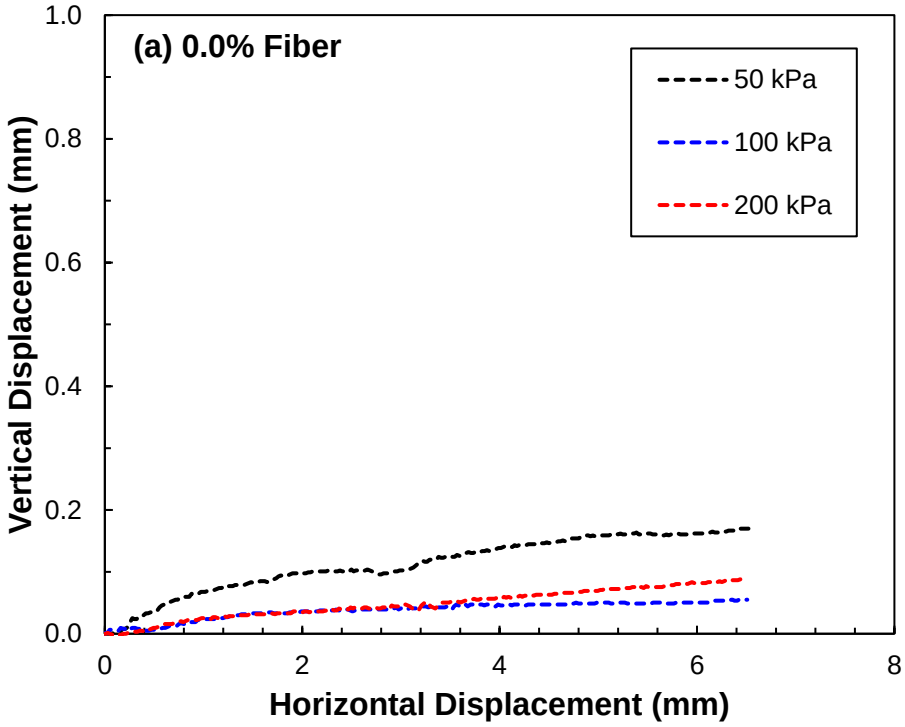
(a) 0.0% Fiber
50 kPa
100 kPa
200 kPa
Vertical Displacement (mm)
Horizontal Displacement (mm)
0.0
0.2
0.4
0.6
0.8
1.0
0
2
4
6
8

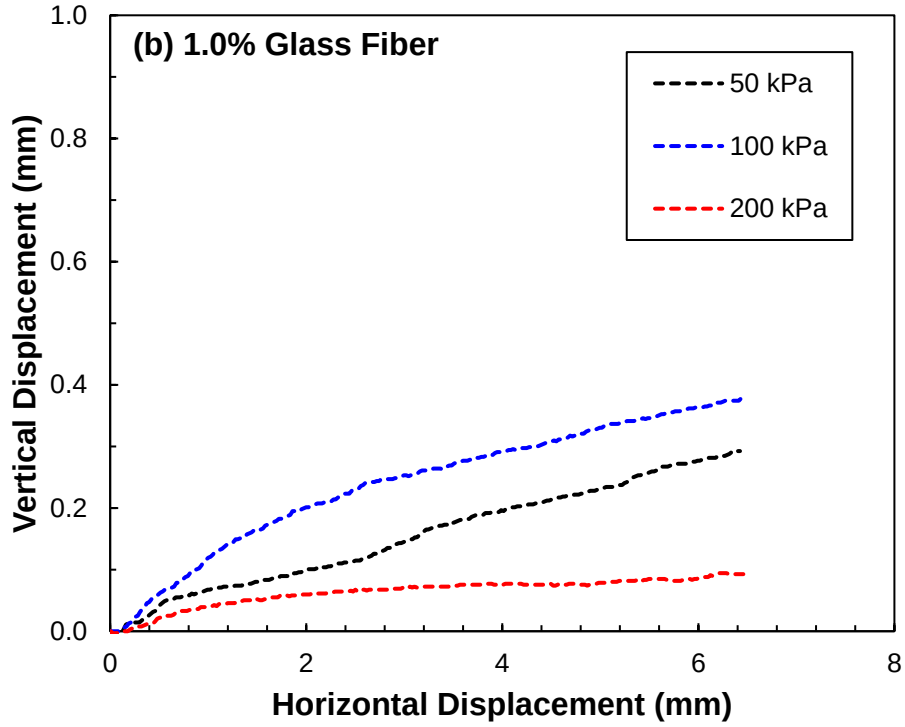
(b) 1.0% Glass Fiber
50 kPa
100 kPa
200 kPa
Vertical Displacement (mm)
Horizontal Displacement (mm)
0.0
0.2
0.4
0.6
0.8
1.0
0
2
4
6
8

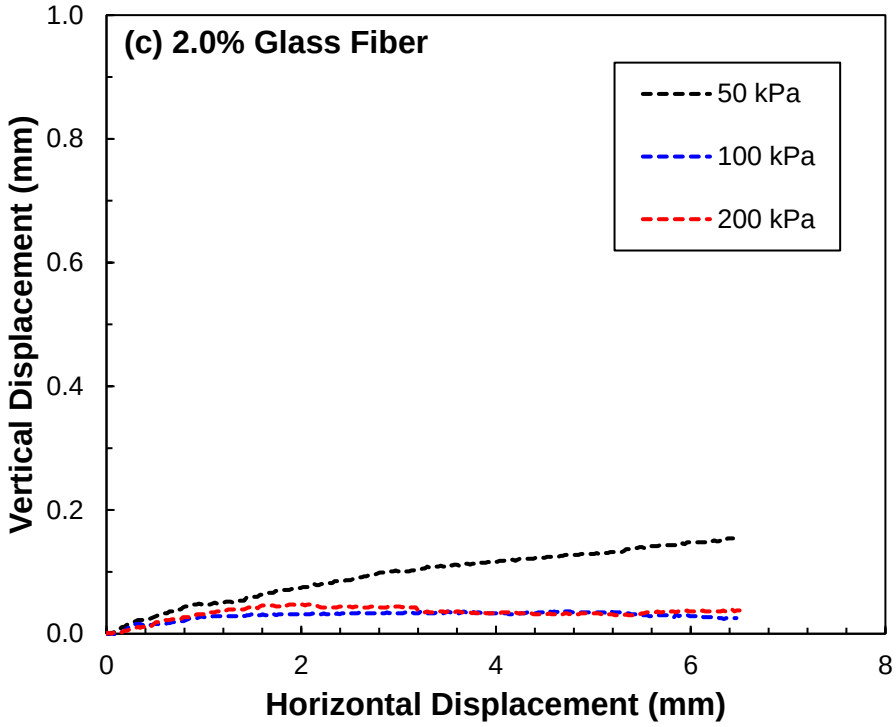
(c) 2.0% Glass Fiber
50 kPa
100 kPa
200 kPa
Vertical Displacement (mm)
Horizontal Displacement (mm)
0.0
0.2
0.4
0.6
0.8
1.0
0
2
4
6
8

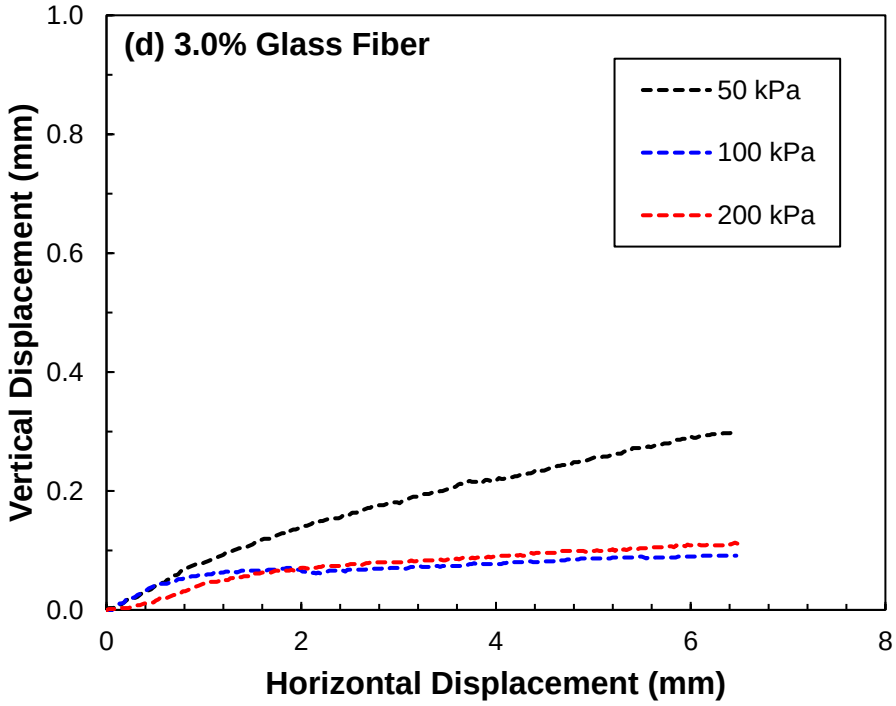
(d) 3.0% Glass Fiber
50 kPa
100 kPa
200 kPa
Vertical Displacement (mm)
Horizontal Displacement (mm)
0.0
0.2
0.4
0.6
0.8
1.0
0
2
4
6
8

Figure 38. Vertical displacement vs. horizontal displacement for (a) 0.0%, (b) 1.0% glass fiber, (c) 2.0% glass fiber, and (d) 3.0% glass fiber in various normal stresses.

As discussed previously, the shear stresses corresponding to their peak and residual strength behaviors were measured and tabulated in Table 12. By plotting these shear stress values along with the normal stresses, the shear strength parameters, such as cohesion and friction angle, can be determined. Figures 39a to 39d show the shear stress vs. normal stress as well as the equations of the best-fit lines for both peak and residual strengths. Based on these, the aforementioned shear strength parameters were tabulated in Table 13 and visualized in Figures 40a and 40b.

Table 12. Shear stress values obtained from the direct simple shear tests.

Shear Stress			
Fiber Content	Normal Stress (kPa)	Peak Strength (kPa)	Residual Strength (kPa)
0.0%	50	**29.76**	**29.76**
	100	**56.94**	**43.14**
	200	**70.72**	**46.97**
1.0%	50	**26.76**	**26.08**
	100	**44.65**	**43.83**
	200	**53.66**	**45.74**
2.0%	50	**29.08**	**28.95**
	100	**52.70**	**48.88**
	200	**76.46**	**66.49**
3.0%	50	**27.31**	**24.30**
	100	**62.12**	**58.03**
	200	**89.43**	**75.37**

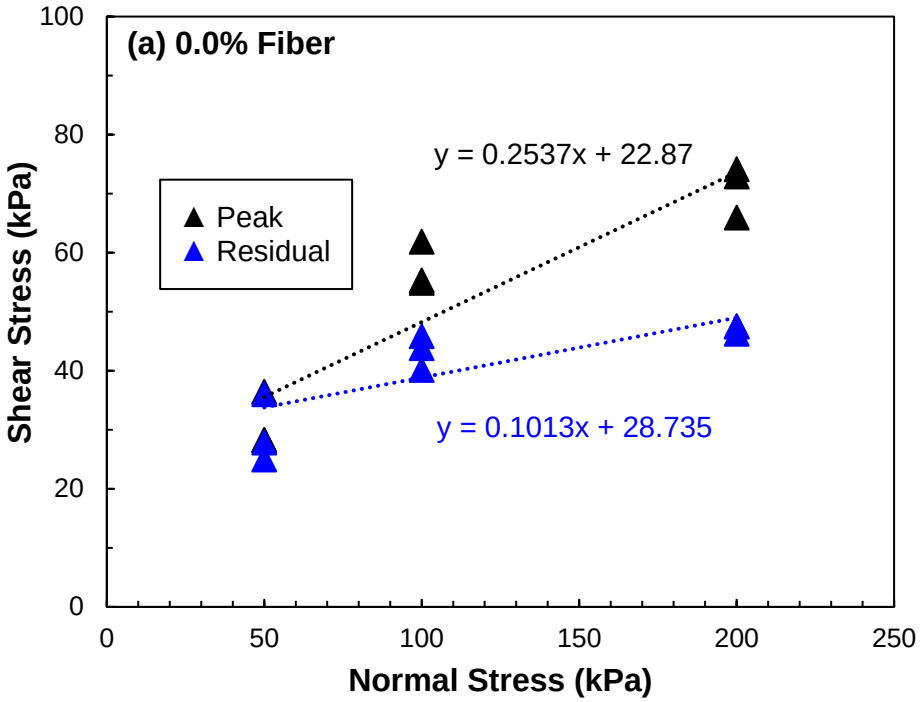
(a) 0.0% Fiber
y = 0.2537x + 22.87
y = 0.1013x + 28.735
Peak
Residual
Shear Stress (kPa)
Normal Stress (kPa)
0
20
40
60
80
100
0
50
100
150
200
250

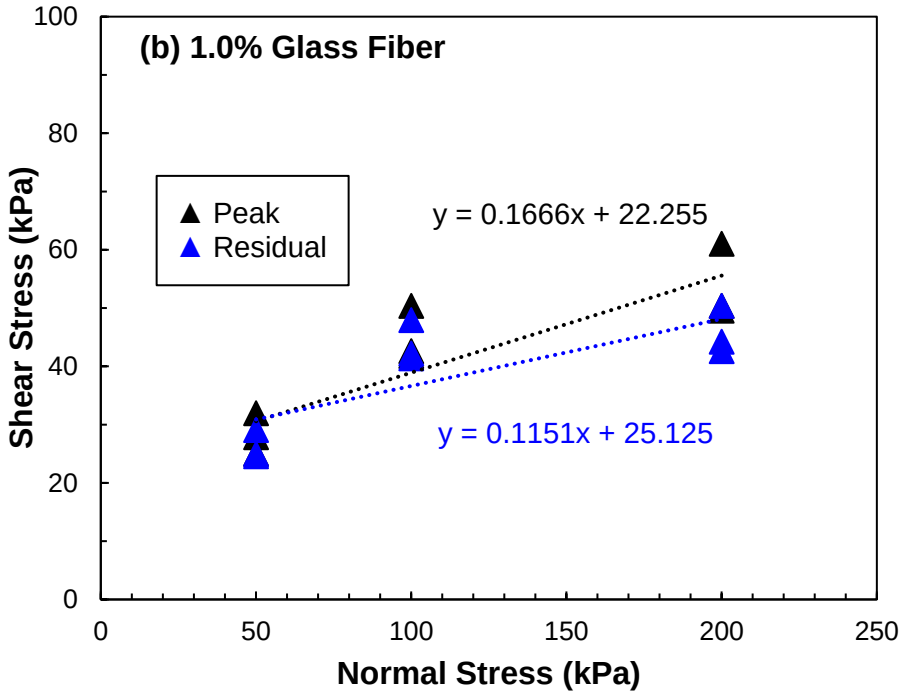
(b) 1.0% Glass Fiber
y = 0.1666x + 22.255
y = 0.1151x + 25.125
Peak
Residual
Shear Stress (kPa)
Normal Stress (kPa)
0
20
40
60
80
100
0
50
100
150
200
250

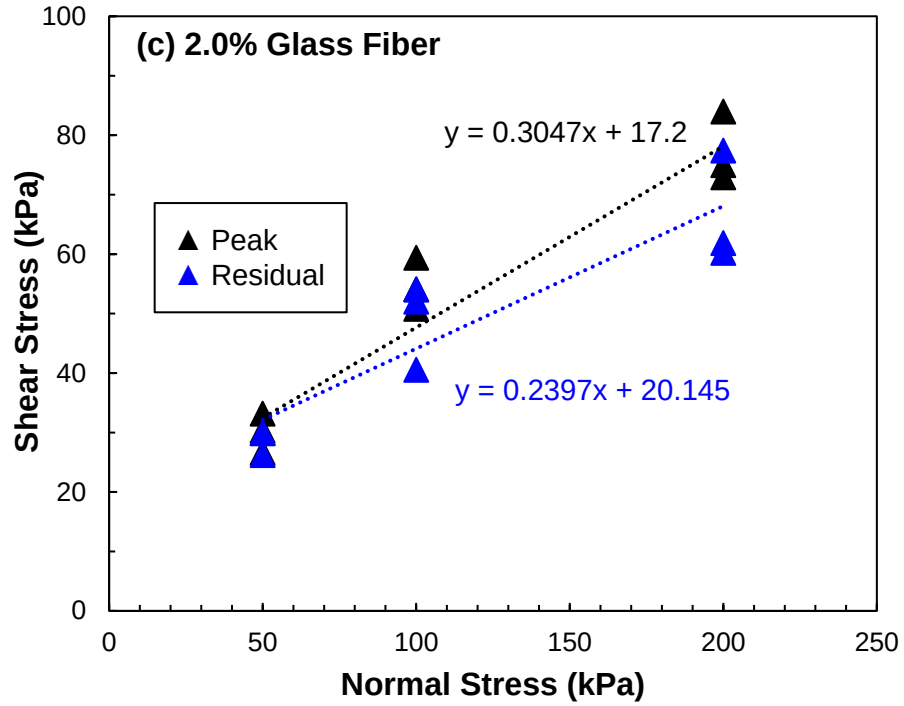

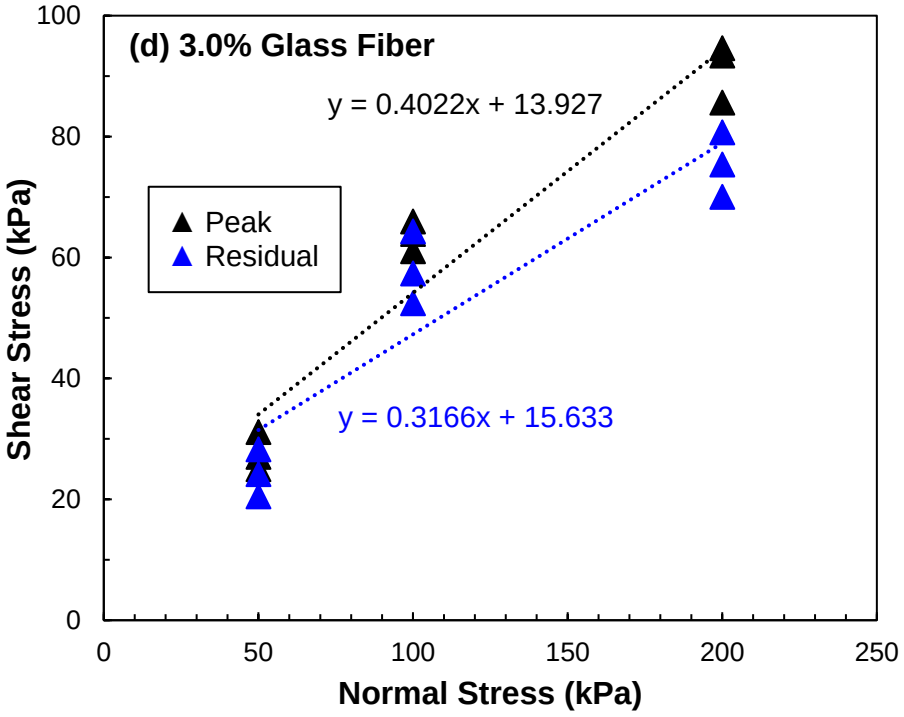

Figure 39. Shear stress vs. normal stress for (a) 0.0%, (b) 1.0% glass fiber, (c) 2.0% glass fiber, and (d) 3.0% glass fiber showing both peak and residual strengths.

Table 13. Shear strength parameters obtained from the direct simple shear tests.

Shear Strength Parameters				
Fiber Content	**Peak Strength**		**Residual Strength**	
	Cohesion (kPa)	Friction Angle	Cohesion (kPa)	Friction Angle
0.0%	**22.87**	**14°**	**28.74**	**6°**
1.0%	**22.26**	**9°**	**25.13**	**7°**
2.0%	**17.20**	**17°**	**20.15**	**13°**
3.0%	**13.93**	**22°**	**15.63**	**18°**

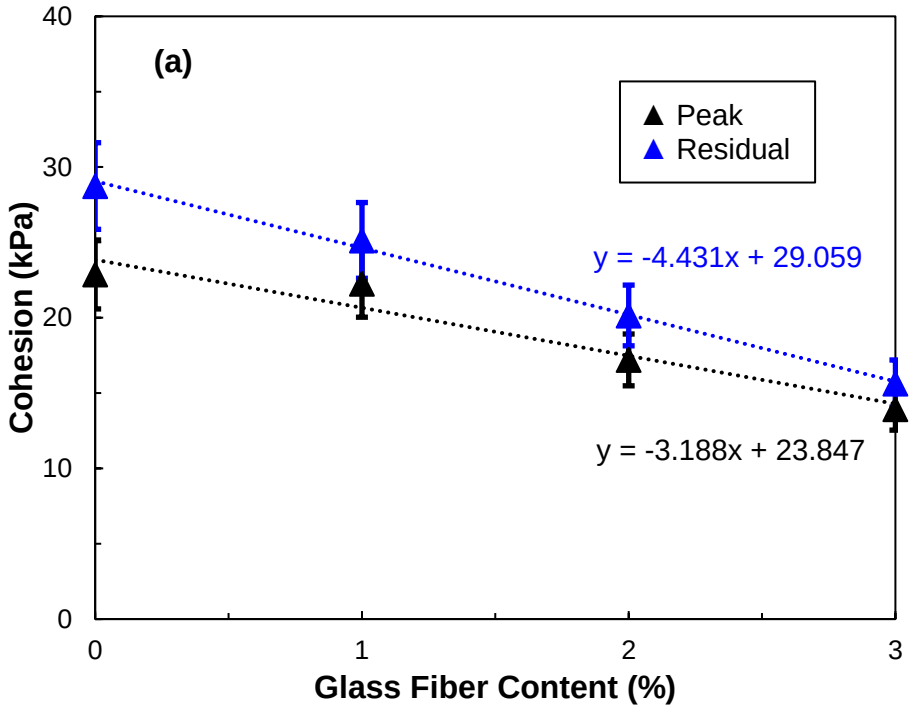

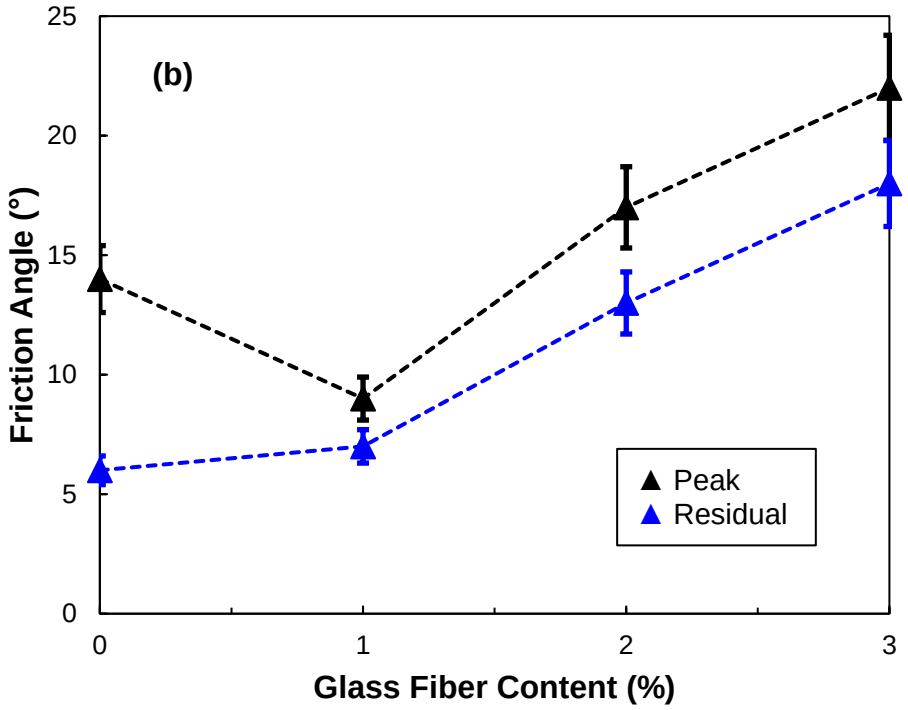

Figure 40. Shear strength parameters (a) cohesion and (b) friction angle vs. glass fiber content for both peak and residual strengths.

4.4.2 EFFECT OF FIBER CONTENT ON THE PEAK STRENGTH

As seen in Figure 40a, the cohesion values under the peak strength followed a decreasing trend with a corresponding increase in fiber content. From 0.0% to 1.0% fiber content, a negligible effect on the cohesion was observed. However, adding 2.0% fiber content translated to a 24.8% decrease from the unreinforced case. Furthermore, the 3.0% fiber content resulted in 39.1% reduction on its cohesion. The significant decrease on the cohesion of the sample under peak strength due to the fiber reinforcement denotes that the clay particle-to-particle interaction has been diminished with the presence of fibers; thus, reducing the cohesion of the specimen.

On the other hand, the friction angle showed a different trend for peak strength. From 0.0% to 1.0% fiber content, it was reduced by 5° for the internal friction angle. This was followed by an increase of 3° and 8° with respect to the unreinforced case, for 2.0% and 3.0% fiber content, respectively. Interestingly, the decrease in friction angle at the 1.0% fiber content was unexpected. However, the succeeding increase in friction angle for higher fiber contents (2.0% and 3.0%) shows that the interlocking of the fibers and the tensile forces generated by these significantly helped in producing greater friction between particle to particle.

4.4.3 EFFECT OF FIBER CONTENT ON THE RESIDUAL STRENGTH

The residual strength signifies the shearing behavior of the soil at large shear strains. At 25% strain level, the shear stresses were obtained to calculate the cohesion and friction angle for residual strength. The cohesion values showed a decrease of 12.6%, 29.9%, and 45.6% from the unreinforced bentonite to the 1.0%, 2.0%, and 3.0% fiber content, respectively. When comparing the cohesion values between peak and residual states, it was evident that the cohesion is higher at the residual state than at the peak state. According to Abbaspour et al. (2020), this occurrence can be attributed to the dilating behavior of the fiber-reinforced samples under large shear strains and the mobilization of tensile stress caused by the fibers. The certain confinement due to the tensile stress could then be represented through apparent cohesion.

On the other hand, the internal friction angle consistently increased by 1°, 7°, and 12° upon the addition of 1.0%, 2.0%, and 3.0% fiber content respectively. Bojnourdi et al. (2020) stated that the improvement of the friction angle under residual state shows the

bridging effect of fibers holding the shearing planes. Lastly, the increase in the friction angle confirms Maher & Woods (1990) idea that at the large shear displacements, the fiber's tensile resistance in the rigidity of the soil composite system is mobilized.

4.4.4 NORMALIZED SHEAR STRESS

Figures 41a to 41d illustrate the normalized shear stress vs. shear strain with respect to their normal stresses. The pre-shearing vertical pressure was used to normalize the shear stress values. As seen in the following figure, for 0.0% fiber, the 50 kPa dataset showed the highest magnitude of normalized shear stress, followed by 100 kPa and 200 kPa readings. However, as the fiber content increases, the 50 kPa dataset consistently gives a closer normalized shear stress relative to 100 kPa. It is noteworthy to mention that in the 2.0% fiber, an inflection point was observed between 50 kPa and 100 kPa datasets. Furthermore, when 3.0% fiber was considered, the 50 kPa dataset was already between the 100 kPa and 200 kPa readings. Essentially, at lower pressure range (i.e., 50 kPa), the fiber influences the shear stress in such a way that it gradually decreases the measured shear stress relative to the confining pressure. According to Mirzababaei et al. (2017), at higher normal stresses, the soil grains are closer to each other, resulting in a greater cumulative contact area of the soil-soil grains than that of the soil-fiber in the system. This could lead to a limited effect of the fiber reinforcement to increase the normalized shear stress (also referred to as the shear stress ratio) of the soil as compared to lower normal stresses.

Another notable observation here is that only at the higher-pressure range (i.e., 100 kPa and 200 kPa), the trend of the peak and residual normalized shear stresses follows the

similar trend for the friction angle of each respective strength behavior. For example, in the case of peak strength, the friction angle decreases from 0.0% to 1.0% fiber, and increases from thereon. This was also observed for the peak normalized shear stress values only for 100 kPa and 200 kPa datasets. On the other hand, the same situation was observed for the residual strength. With this, it can be said that the trend consistencies between friction angle and normalized shear stress at the higher-pressure range validate the effect of fiber reinforcement at these certain conditions.

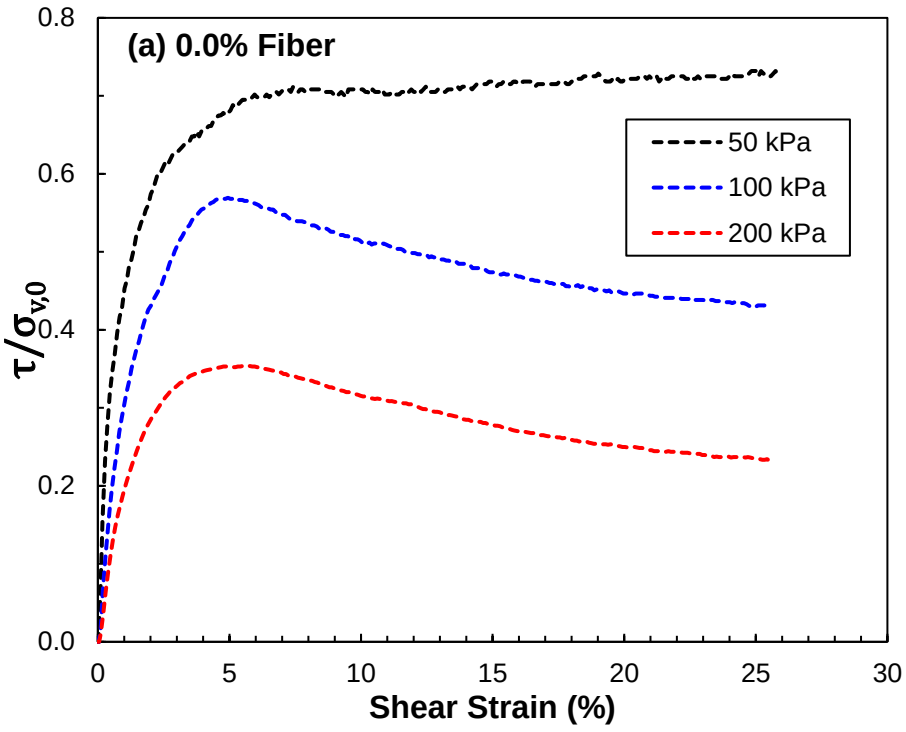

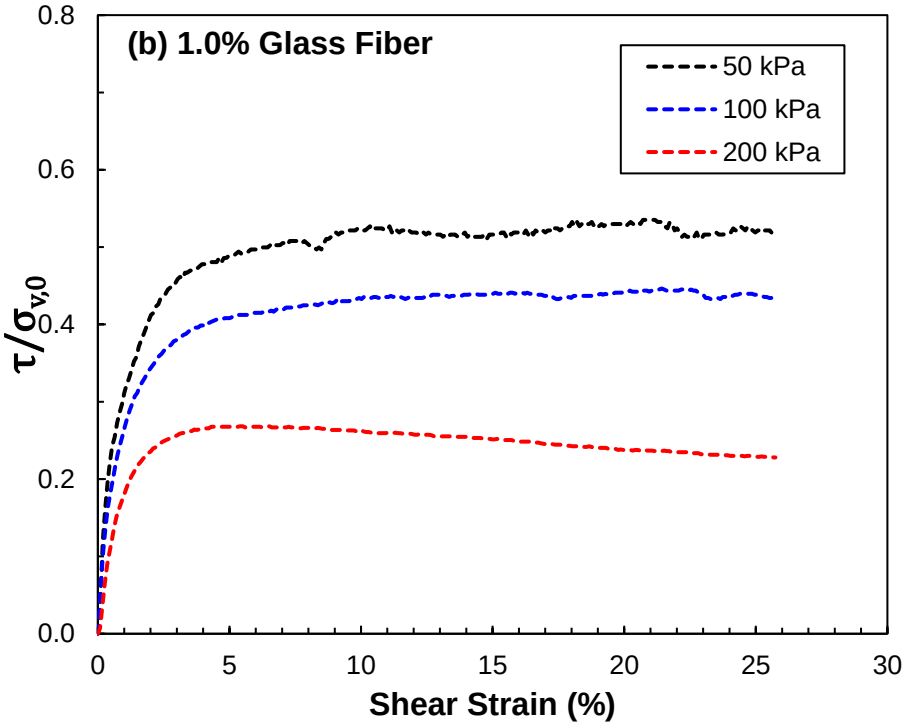
(b) 1.0% Glass Fiber
50 kPa
100 kPa
200 kPa
τ/σv,0
0.0
0.2
0.4
0.6
0.8
0
5
10
15
20
25
30
Shear Strain (%)

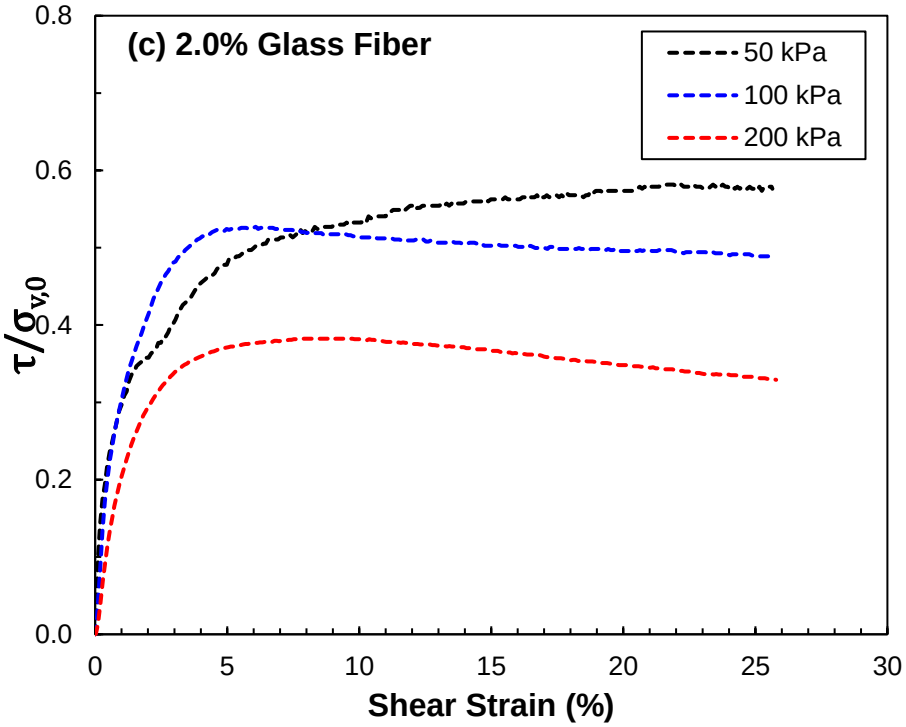
(c) 2.0% Glass Fiber
50 kPa
100 kPa
200 kPa
τ/σv,0
0.0
0.2
0.4
0.6
0.8
0
5
10
15
20
25
30
Shear Strain (%)

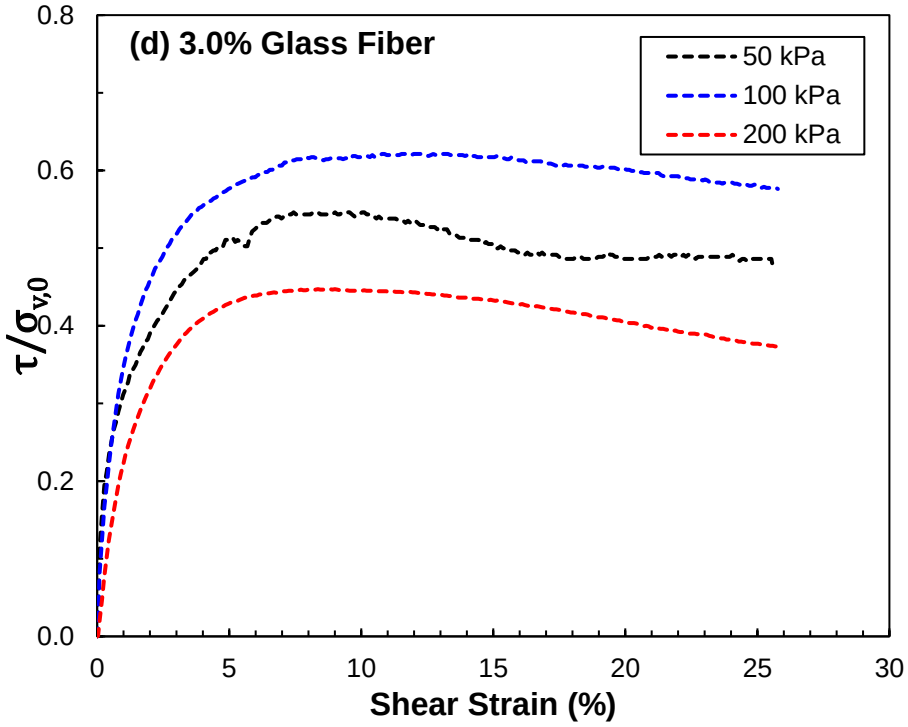

Figure 41. Normalized shear stress vs. shear strain for (a) 0.0%, (b) 1.0% glass fiber, (c) 2.0% glass fiber, and (d) 3.0% glass fiber in different normal stresses.

4.4.5 STRESS PATHS

The total stress paths of the 4 direct simple shear tests given in Figure 42 are plotted in the $p - q$ space. Given that this test was done in consolidated-undrained condition, the expected stress paths followed a similar slope. It was found that the stress paths for 50 kPa, 100 kPa, and 200 kPa under the aforementioned drainage condition are not significantly affected by the fiber content in the soil sample. However, it is important to note that these stress paths are solely obtained from the derivation previously discussed. If such accurate

stress paths are deemed necessary, it is advised to perform triaxial tests to better interpret the stress paths as well as measure the pore pressure generated throughout the tests.

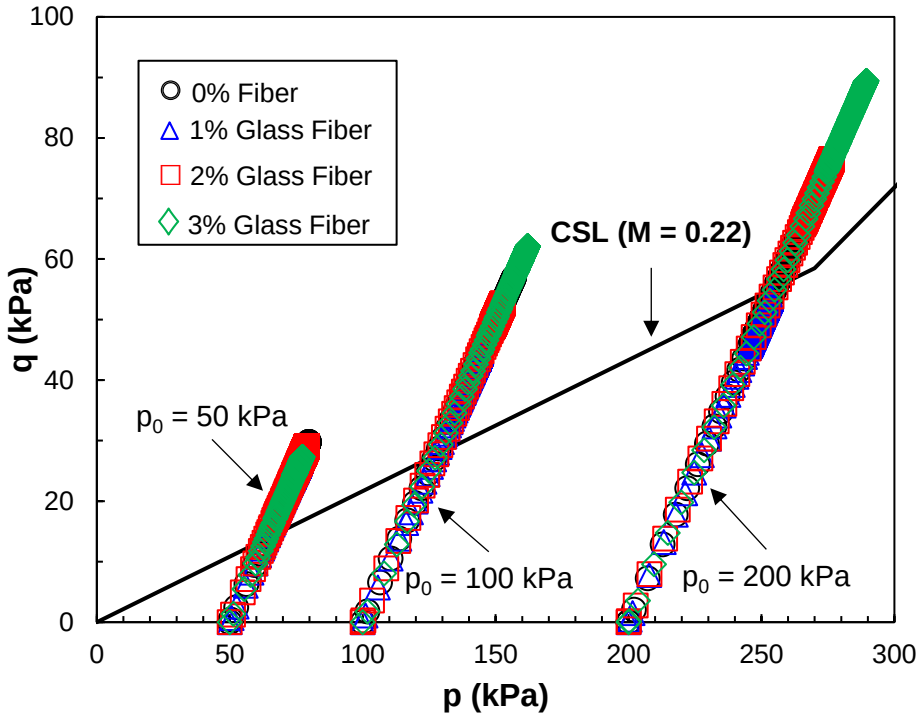

Figure 42. Stress paths in the $p - q$ space with respect to the applied normal stress.

4.4.6 MODIFIED CAM CLAY MODEL

The Modified Cam Clay Model is represented by three different axes: specific volume v, normal stress p, and deviatoric stress q. These three axes can form two different spaces, namely: $v - \ln p$ and $p - q$. The following subsections shall discuss the combined findings from the one-dimensional consolidation and direct simple shear tests in both spaces.

4.4.7 SPECIFIC VOLUME VS. PRESSURE ($v - \ln p$)

In the $v - \ln p$ space, λ is the slope of the virgin consolidation line while κ is the slope of the swelling line. Figure 43 shows the specific volume vs. pressure obtained from the one-dimensional consolidation data for different fiber contents at 22°C. In addition to that, Table 14 is provided to summarize the λ and κ values for each corresponding fiber content.

With respect to the fiber content, the λ followed a decreasing trend, emphasized at the 1.0% to 3.0% fiber content data, giving a 26.2% decrease. Similarly, the κ showed a decreasing trend in terms of fiber content. For the fiber contents 1.0% and 3.0%, the κ was reduced by 10.1% and 22.8%, respectively.

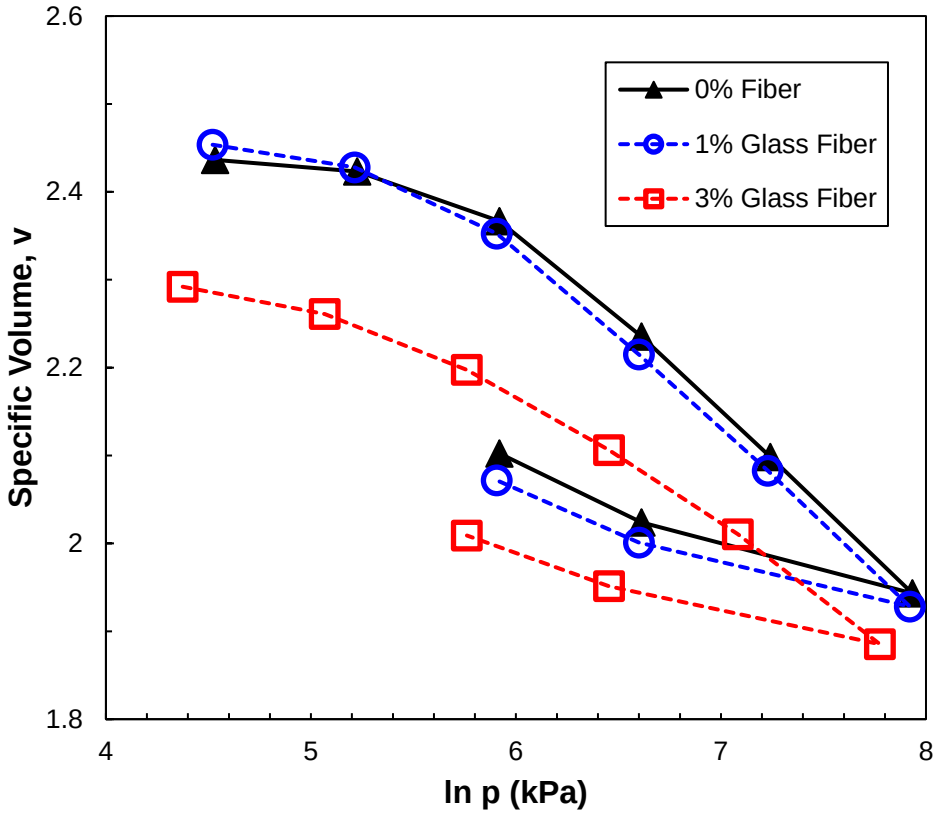

Figure 43. Specific volume vs. pressure in the natural logarithmic scale ($v - \ln p$ space) calculated from the one-dimensional consolidation data.

Table 14. Modified Cam Clay Model parameters derived from the one-dimensional consolidation data.

Modified Cam Clay Model		
Fiber Content	λ	κ
0.0%	**0.210**	**0.079**
1.0%	**0.211**	**0.071**
3.0%	**0.155**	**0.061**

4.4.8 TOTAL STRESS VS. DEVIATORIC STRESS ($p - q$)

In the $p - q$ space, the yield surface can be drawn to reflect the elastic boundary and the start of plastic deformation with respect to the applied stresses (Budhu, 2011). To be consistent with the one-dimensional consolidation and direct simple shear test results, only the yield surfaces for 0.0%, 1.0% glass fiber, and 3.0% glass fiber datasets were plotted in Figure 44, as well as the calculated slope of the CSL (M = 0.22). Inside the yield surface, this area signifies the elastic zone of the sample, whereas anywhere beyond the yield surface under the CSL denotes its plastic zone. Once the stress state reaches the CSL, the sample is said to fail. Therefore, any point of stress located above the CSL is considered non-existent. For illustration purposes, portions above the CSL are also drawn to visually compare the yield surfaces.

The figure revealed that at 1.0% glass fiber content, insignificant change in the yield surface was observed. At the higher-pressure range, it appeared that there was a slight surface reduction from 0.0% to 1.0% glass fiber content. This is mainly due to the difference in the calculated preconsolidation pressure for both cases. Nonetheless, the general shape of the yield surfaces for both conditions is still similar. However, by the addition of 3.0% glass fiber, the yield surface significantly expanded. As a result, it can be stated that the presence of glass fiber specifically at 3.0% fiber content improved the specimen's elastic zone. The expansion of the material's elastic zone is beneficial for the EBS since it will require higher stresses before the bentonite experiences plastic deformation. When plastic deformation on the buffer material happens, it may possibly cause irregularities in the canister arrangement and damage the canister itself, spreading the radionuclides throughout the whole gallery of the geological repository.

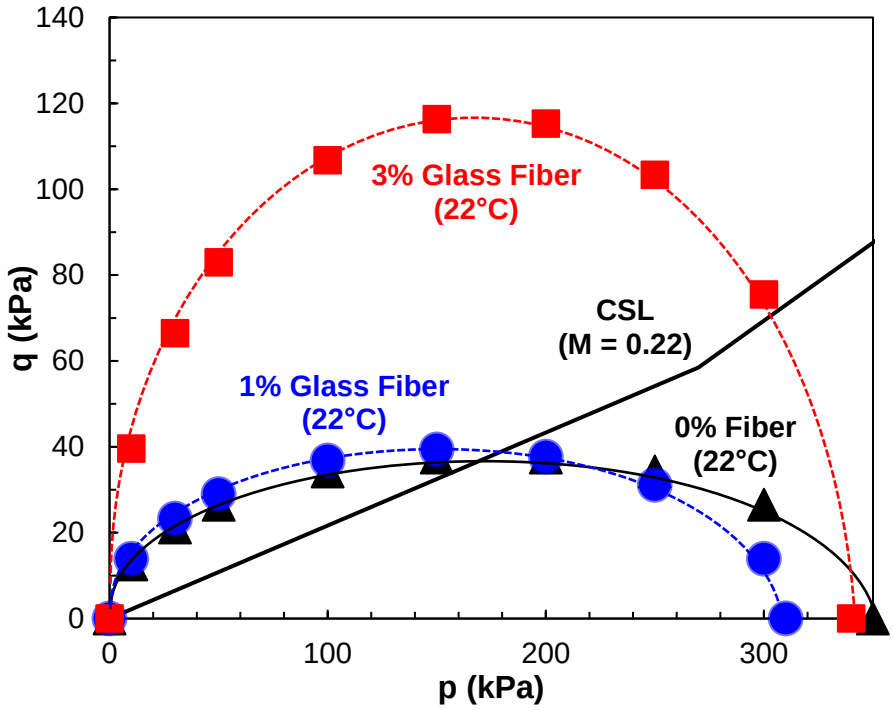

Figure 44. Mean total stress vs. deviatoric stress in the $p - q$ space (yield surfaces) calculated from the one-dimensional consolidation data.

4.5 SUMMARY

This part of the research was undertaken to provide information on the shearing behavior of the glass fiber-reinforced bentonite. Through the direct simple shear tests, the shear strength parameters (cohesion and friction angle) for both peak and residual states were obtained. Additionally, the Modified Cam Clay Model was employed to predict the specimen's behavior under the critical state as well as the effect of fiber reinforcement. Based on the experimental data and their respective analyses, the following conclusions can be drawn:

1. At both peak and residual states, the cohesion consistently reduced as the fiber content was increased. Higher cohesion was observed at the residual behavior than the peak behavior.
2. In the case of peak strength, the friction angle decreased from 0.0% to 1.0% fiber content, then vastly increased for 2.0% and 3.0% fiber content. Meanwhile, the friction angle continuously increased with increasing fiber content for the residual strength.
3. Normalized shear stress presented a notable trend at the 50 kPa dataset, where the higher fiber content gives closer normalized shear stress relative to 100 kPa. Therefore, the fiber reinforcement showed a significant effect on the measured shear stress in a decreasing manner relative to the lower confining pressure.
4. Individual stress paths for 50 kPa, 100 kPa, and 200 kPa followed the same trend, regardless of the fiber content. It is said that the amount of fiber reinforcement does not affect the stress paths of the sample.
5. Modified Cam Clay Model parameters λ and κ showed a decreasing trend in terms of fiber content. These parameters followed similar observed trends from the swelling pressure and compressibility characteristics.
6. In the $p - q$ space, yield surfaces were plotted based on the direct simple shear test results. Insignificant change in the yield surface was observed from 0.0% to 1.0% fiber content. However, surface expansion was evident due to the addition of 3.0% glass fiber. Therefore, the presence of glass fiber at 3.0% fiber content improved the specimen's elastic zone.

CHAPTER 5. CONCLUSIONS AND RECOMMENDATIONS

5.1 CONCLUSIONS

Bentonite may be applied to various engineering interventions. Such examples of these are grouting, barrier material for landfills, and buffer material for a nuclear waste repository. With the application of elevated temperature, its high swelling capacity and low permeability may be affected, resulting in the presence of desiccated cracks. In an attempt to address this concern, inorganic microfibers (e.g., glass fibers) are proposed as a reinforcement to the compacted bentonite to mitigate this problem. In this study, analyses of the swelling and compressibility behavior of unreinforced and inorganic microfiber-reinforced bentonite under ambient (22°C) and elevated (50°C) temperatures were carried out with the use of the one-dimensional consolidation test. Furthermore, the effect of the fiber reinforcement on the shearing behavior of bentonite was determined through the direct simple shear test. Lastly, the specimen's behavior under the critical state was predicted using the Modified Cam Clay Model. The following conclusions were drawn from the objectives of this research:

1. Lower swelling pressures were observed upon the inclusion of fiber reinforcement. With the limited fiber contents investigated, it was known that as the fiber content in the bentonite mixture increases, the resulting swelling pressure consistently decreases.
2. Temperature elevation leads to a rise (at most by 35%) in the swelling pressure for all fiber contents.

3. The fiber inclusion causes a significant reduction in the C_c and C_s, showing the degradation of the bentonite's compressibility characteristics. On the other hand, the application of elevated temperature leads to an increase in both parameters, signifying the improvement of the compressibility behavior of the bentonite.
4. The trend consistency in the swelling pressure, C_c, and C_s, affirms the distinct behaviors of the swelling and compressibility of the bentonite under the influence of fiber reinforcement and temperature elevation.
5. Within a specific consolidation pressure, the addition of fiber reinforcement leads to a lower m_v while the application of elevated temperature results in a higher m_v. Similar trends with respect to the fiber content and temperature elevation are deemed consistent with that of the swelling pressure, C_c, and C_s.
6. Meanwhile, c_v does not present a distinct trend in terms of fiber content. This shows that the fiber content does not have a significant effect on the mentioned parameter. Nonetheless, the temperature elevation results in lower c_v values.
7. For lower range of pressure values, the estimated hydraulic conductivity values are smaller only for the elevated temperature while fiber reinforcement does not significantly affect this parameter. For higher range of pressure values, all testing results present similar values, suggesting that neither fiber inclusion nor temperature elevation significantly affects the hydraulic conductivity.
8. The cohesion consistently decreased as the fiber content was increased at both peak and critical states. Higher cohesion was observed at the critical behavior than the peak behavior.

9. For the peak strength, the friction angle decreased from 0.0% to 1.0% fiber content, then significantly increased for 2.0% and 3.0% fiber content. However, for the residual strength, the friction angle continuously increased with increasing fiber content.
10. Normalized shear stress showed a remarkable trend at the 50 kPa dataset, where the higher fiber content gives a closer normalized shear stress relative to 100 kPa. Thus, the fiber reinforcement caused a significant effect on the measured shear stress at a decreasing manner relative to the lower confining pressure.
11. The stress paths for 50 kPa, 100 kPa, and 200 kPa followed the similar trend, irrespective of the fiber content. Given these results, the amount of fiber reinforcement does not affect the stress paths of the sample.
12. Modified Cam Clay Model parameters λ and κ showed reduced values in terms of fiber content. These parameters showed consistent trends from that of the swelling pressure and compressibility characteristics.
13. From 0.0% to 1.0% fiber content, no significant change in the yield surface was observed. Meanwhile, with the inclusion of 3.0% glass fiber, a significant surface expansion was evident. Therefore, the presence of glass fiber at 3.0% fiber content improved the specimen's elastic zone.

5.2 RECOMMENDATIONS

With the results and conclusions drawn from this research, the following recommendations for related future studies are hereby enumerated:

1. If there is no time constraint when this study was conducted, the researchers are encouraged to explore varying fiber contents, fiber lengths, and fiber types to check the effect of such on the swelling, compressibility, and shearing behaviors of the bentonite. Using basalt and graphite microfibers can also be considered as these are the common types of fiber used for enhancing engineering properties.
2. Several studies have reported different findings depending on the dry density of the bentonite. Therefore, different dry densities (i.e., high and low dry density bentonite) are suggested for future consideration.
3. Due to the equipment limitation, elevated temperature conditions were not imposed on the direct simple shear tests. For the sake of consistency, it is highly recommended to perform direct simple shear tests with applied temperature. This would enable to identify the temperature effect on the bentonite's shearing behavior.
4. Since the main objective of this study is to observe the swelling, compressibility, and shearing behaviors of the bentonite, both one-dimensional consolidation and direct simple shear tests were performed. However, this approach has a limitation in terms of data analysis. Therefore, it is highly recommended to conduct triaxial tests and analyze the data for easier acquisition of such parameters.

5. Comparison of the Modified Cam Clay Model results calculated from the combined data of one-dimensional consolidation and direct simple shear tests vs. the triaxial test would be a great research venture.
6. In the actual condition of the nuclear waste upon disposal, the canister emits high heat, generating up to 200°C and above. To properly model the real-life scenario in the nuclear waste repository, subjecting the bentonite to higher temperatures is one of the key recommendations this study conveys.
7. Lastly, it is highly suggested to measure other engineering properties such as hydraulic conductivity, thermal conductivity, soil-water characteristic curve, etc. Specifically, this study could only offer estimated values of the hydraulic conductivity. Therefore, these values are still subject for further verification after obtaining the experimental data.

REFERENCES

Abbaspour, M., Narani, S. S., Aflaki, E., Nejad, F. M., & Hosseini, S. M. M. M. (2020). Strength and swelling properties of a waste tire textile fiber-reinforced expansive soil. *Geosynthetics International*, *27*(5), 476–489. https://doi.org/10.1680/jgein.20.00010

Abdou, M. I., Al-sabagh, A. M., & Dardir, M. M. (2013). Evaluation of Egyptian bentonite and nano-bentonite as drilling mud. *Egyptian Journal of Petroleum*, *22*(1), 53–59. https://doi.org/10.1016/J.EJPE.2012.07.002

Afolabi, R. O., Orodu, O. D., & Efeovbokhan, V. E. (2017). Properties and application of Nigerian bentonite clay deposits for drilling mud formulation: Recent advances and future prospects. In *Applied Clay Science* (Vol. 143, pp. 39–49). Elsevier Ltd. https://doi.org/10.1016/j.clay.2017.03.009

ASTM D698-12. (2021). *Standard Test Methods for Laboratory Compaction Characteristics of Soil Using Standard Effort (12,400 ft-lbf/ft3 (600 kN-m/m3))*. https://doi.org/10.1520/D0698-12R21

ASTM D2435-11. (2020). *Standard Test Methods for One-Dimensional Consolidation Properties of Soils Using Incremental Loading*. https://doi.org/10.1520/D2435_D2435M-11R20

ASTM D4546-21. (2021). *Standard Test Methods for One-Dimensional Swell or Collapse of Soils*. https://doi.org/10.1520/D4546-21

ASTM D6528-17. (2017). *Standard Test Method for Consolidated Undrained Direct Simple Shear Testing of Fine Grain Soils 1*. https://doi.org/10.1520/D6528-17

Australian Department of Industry, I. and S. (2015, December). *National Radioactive Waste Management Project*. https://slideplayer.com/slide/9360803/

Azeez, G. O., Dada, E. O., Lawal, I. A., & Arinkoola, A. O. (2018). Modification of Nigerian Bentonite for Utilization in Oil Well Drilling Operations. *LAUTECH Journal of Engineering and Technology*, *12*(1), 74–84.

Bag, R., & Rabbani, A. (2017). Effect of temperature on swelling pressure and compressibility characteristics of soil. *Applied Clay Science*, *136*, 1–7. https://doi.org/10.1016/j.clay.2016.10.043

Baroid Industrial Drilling Products. (2011). *BENSEAL Sealing and Plugging Agent*. https://www.baroididp.com/en/products/benseal

Bian, X., Cui, Y. J., & Li, X. Z. (2019). Voids effect on the swelling behaviour of compacted bentonite. *Geotechnique*, *69*(7), 593–605. https://doi.org/10.1680/jgeot.17.P.283

Bojnourdi, S., Narani, S. S., Abbaspour, M., Ebadi, T., & Mir Mohammad Hosseini, S. M. (2020). Hydro-mechanical properties of unreinforced and fiber-reinforced used motor oil (UMO)-contaminated sand-bentonite mixtures. *Engineering Geology*, *279*. https://doi.org/10.1016/j.enggeo.2020.105886

Bryan, S. M. (2015, February 13). *Things to know about the WIPP leak, one year on*. Albuquerque Journal. https://www.abqjournal.com/541230/things-to-know-about-the-wipp-leak-one-year-on.html

Budhu, M. (2011). *Soil Mechanics and Foundations* (3rd ed.). John Wiley & Sons.

Cai, Y., Shi, B., Ng, C. W. W., & Tang, C. sheng. (2006). Effect of polypropylene fibre and lime admixture on engineering properties of clayey soil. *Engineering Geology*, *87*(3–4), 230–240. https://doi.org/10.1016/j.enggeo.2006.07.007

Canadian Nuclear Safety Commission. (2021, May 4). *Low- and intermediate-level radioactive waste*. http://nuclearsafety.gc.ca/eng/waste/low-and-intermediate-waste/index.cfm

Casagrande, M. D. T., Coop, M. R., & Consoli, N. C. (2006). Behavior of a Fiber-Reinforced Bentonite at Large Shear Displacements. *Journal of Geotechnical and Geoenvironmental Engineering*, *132*(11), 1505–1508. https://doi.org/10.1061/(ASCE)1090-0241(2006)132:11(1505)

Chaduvula, U., Viswanadham, B. V. S., & Kodikara, J. (2017). A study on desiccation cracking behavior of polyester fiber-reinforced expansive clay. *Applied Clay Science*, *142*, 163–172. https://doi.org/10.1016/j.clay.2017.02.008

Das, B., & Sobhan, K. (2012). *Principles of Geotechnical Engineering* (8th ed.). Global Engineering.

de Camillis, M., di Emidio, G., Bezuijen, A., Verastegui Flores, D., van Stappen, J., & Cnudde, V. (2017). Effect of wet-dry cycles on polymer treated bentonite in seawater: swelling ability, hydraulic conductivity and crack analysis. *Applied Clay Science*, *142*, 52–59. https://doi.org/10.1016/J.CLAY.2016.11.011

Dev, K. L., Pillai, R. J., & Robinson, R. G. (2013). Estimation of Critical State Parameters from One-dimensional Consolidation and Triaxial Compression Tests. *Indian Geotechnical Journal*, *43*(3), 229–237. https://doi.org/10.1007/s40098-013-0063-5

Dohrmann, R., Kaufhold, S., & Lundqvist, B. (2013). The Role of Clays for Safe Storage of Nuclear Waste. In *Developments in Clay Science* (1st ed., Vol. 5, Issue C). Elsevier Inc. https://doi.org/10.1016/B978-0-08-098259-5.00024-X

Dutta, J., & Mishra, A. K. (2017). *Consolidation Behavior of Compacted Bentonites in the Presence of Heavy Metals*. https://doi.org/10.1061/(ASCE)

Fakharian, K., & Evgin, E. (1995). *International Conferences on Recent Advances in Geotechnical Earthquake Engineering and Soil Dynamics* (Vol. 4). https://scholarsmine.mst.edu/icrageesd/03icrageesd/session01/4

Grimsel Test Site. (2022). *Full-scale Engineered Barriers Experiment FEBEXe - Introduction*. https://grimsel.com/gts-projects/febexe/febexe-introduction

Halecky, N. E. (2010). *Drift Natural Convection and Seepage at the Yucca Mountain Repository*. https://escholarship.org/uc/item/6s7831c6

Hansen, E. L., Hemmen, H., Fonseca, D. M., Coutant, C., Knudsen, K. D., Plivelic, T. S., Bonn, D., & Fossum, J. O. (2012). Swelling transition of a clay induced by heating. *Scientific Reports*, *2*, 1–4. https://doi.org/10.1038/srep00618

Hauser, V. L., Weand, B. L., & Gill, M. D. (2001). Natural Covers for Landfills and Buried Waste. *Journal of Environmental Engineering*, *127*(9), 768–775. https://doi.org/10.1061/(ASCE)0733-9372(2001)127:9(768)

He, Y., Hu, G., Wu, D. yu, Zhu, K. fei, & Zhang, K. neng. (2022). Contaminant migration and the retention behavior of a laterite–bentonite mixture engineered barrier in a landfill. *Journal of Environmental Management*, *304*. https://doi.org/10.1016/j.jenvman.2021.114338

Hsu, J. (2021, March 9). *Nuclear Power Looks to Regain Its Footing 10 Years after Fukushima*. Scientific American. https://www.scientificamerican.com/article/nuclear-power-looks-to-regain-its-footing-10-years-after-fukushima/

International Atomic Energy Agency. (2020, September). *What is the Clean Energy Transition and How Does Nuclear Power Fit In?* https://www.iaea.org/bulletin/what-is-the-clean-energy-transition-and-how-does-nuclear-power-fit-in

Ishikawa, T. (2014). Heat-Resistant Inorganic Fibers. *13th International Ceramics Congress - Part C*, *89*, 129–138. https://doi.org/10.4028/www.scientific.net/ast.89.129

Jani-Friend, I. (2021, September 20). *Explainer: Australia's nuclear-powered submarine deal is fueling anger in the country. Here's why*. CNN. https://www.cnn.com/2021/09/18/australia/nuclear-energy-climate-aukus-submarines-intl-cmd/index.html

Joshi, S. v., Drzal, L. T., Mohanty, A. K., & Arora, S. (2004). Are natural fiber composites environmentally superior to glass fiber reinforced composites? *Composites Part A: Applied Science and Manufacturing*, *35*(3), 371–376. https://doi.org/10.1016/j.compositesa.2003.09.016

Kim, M., Lee, S., Cheon, E., Kim, M., & Yoon, S. (2021). Thermochemical changes on swelling pressure of compacted bentonite. *Annals of Nuclear Energy*, *151*. https://doi.org/10.1016/J.ANUCENE.2020.107882

Kumar, S., & Yong, W. L. (2002). Effect of bentonite on compacted clay landfill barriers. *Soil and Sediment Contamination*, *11*(1), 71–89. https://doi.org/10.1080/20025891106709

Lambe, T. W. (1964). Methods of Estimating Settlement. *Journal of the Soil Mechanics and Foundations Division*, *90*(5), 43–67. https://doi.org/10.1061/JSFEAQ.0000662

Lambe, T. W., & Whitman, R. v. (1969). *Soil Mechanics*. John Wiley & Sons.

Lawrence Berkeley National Laboratory. (2022a). *DECOVALEX - DEvelopment of COupled Models and their VALidation Against EXperiments in Nuclear Waste Isolation*. https://eesa.lbl.gov/projects/decovalex/

Lawrence Berkeley National Laboratory. (2022b). *The Yucca Mountain Project*. https://eesa.lbl.gov/projects/yucca-mountain-project/

Liu, X., Cai, G., Congress, S. S. C., & Liu, L. (2021). Thermomechanical Analysis of Fiber–Bentonite-Based Mixtures as Buffer Material in an Engineered Nuclear Barrier. *Journal of Materials in Civil Engineering*, *33*(2), 04020464. https://doi.org/10.1061/(asce)mt.1943-5533.0003515

Liu, X., Cai, G., Liu, L., Liu, S., & Puppala, A. J. (2019). Thermo-hydro-mechanical properties of bentonite-sand-graphite-polypropylene fiber mixtures as buffer materials for a high-level radioactive waste repository. *International Journal of Heat and Mass Transfer*, *141*, 981–994. https://doi.org/10.1016/j.ijheatmasstransfer.2019.07.015

Maher, M. H., & Woods, R. D. (1990). Dynamic Response of Sand Reinforced with Randomly Distributed Fibers. *J. Geotech. Engrg*, *7*, 116.

Mirzababaei, M., Arulrajah, A., Horpibulsuk, S., & Aldava, M. (2017). Shear strength of a fibre-reinforced clay at large shear displacement when subjected to different stress histories. *Geotextiles and Geomembranes*, *45*(5), 422–429. https://doi.org/10.1016/j.geotexmem.2017.06.002

Mukherjee, K., & Mishra, A. K. (2019). Hydro-Mechanical Properties of Sand-Bentonite-Glass Fiber Composite for Landfill Application. *KSCE Journal of Civil Engineering*, *23*(11), 4631–4640. https://doi.org/10.1007/s12205-019-2015-9

Mukherjee, K., & Mishra, A. K. (2021). Recycled waste tire fiber as a sustainable reinforcement in compacted sand–bentonite mixture for landfill application. *Journal of Cleaner Production*, *329*. https://doi.org/10.1016/j.jclepro.2021.129691

Narani, S. S., Abbaspour, M., Mir Mohammad Hosseini, S. M., Aflaki, E., & Moghadas Nejad, F. (2020). Sustainable reuse of Waste Tire Textile Fibers (WTTFs) as

reinforcement materials for expansive soils: With a special focus on landfill liners/covers. *Journal of Cleaner Production*, *247*. https://doi.org/10.1016/J.JCLEPRO.2019.119151

Organisation for Economic Co-operation and Development. (2003). *Engineered Barrier Systems and the Safety of Deep Geological Repositories: State-of-the-art Report*. OECD Publishing.

Owens Corning. (2022). *158B Type 30™ Single-End Roving*. https://www.owenscorning.com/composites

Phanikumar, B. R., & Singla, R. (2016). Swell-consolidation characteristics of fibre-reinforced expansive soils. *Soils and Foundations*, *56*(1), 138–143. https://doi.org/10.1016/j.sandf.2016.01.011

Pusch, R., Kärnland, O., & Hökmark, H. (1990). *GMM - A general microstructural model for qualitative and quantitative studies of smectite clays*.

Roscoe, K. H., & Burland, J. B. (1970). On the generalized stress-strain behavior of "wet" clay. *Journal of Terramechanics*, *7*(2), 107–108. https://doi.org/10.1016/0022-4898(70)90160-6

Sánchez, M., Gens, A., Villar, M. V., & Olivella, S. (2016). A Fully Coupled THM Double Porosity Formulation for Unsaturated Soils. *International Journal of Geomechanics*.

Schanz, T., & Tripathy, S. (2009). Swelling pressure of a divalent-rich bentonite: Diffuse double-layer theory revisited. *Water Resources Research*, *45*(2). https://doi.org/10.1029/2007WR006495

Sellin, P., & Leupin, O. X. (2014). The use of clay as an engineered barrier in radioactive-waste management - A review. *Clays and Clay Minerals*, *61*(6), 477–498. https://doi.org/10.1346/CCMN.2013.0610601

Shirasb, A., Hamidi, A., & Ahmadi, M. M. (2020). Consolidation characteristics of a thermally cured sand–bentonite mixture. *SN Applied Sciences*, *2*(6). https://doi.org/10.1007/s42452-020-2932-8

SKB. (2011). *Svensk Kärnbränslehantering AB Long-term safety for the final repository for spent nuclear fuel at Forsmark Main report of the SR-Site project Volume I*. www.skb.se

Soltani, A., Deng, A., & Taheri, A. (2018). Swell–compression characteristics of a fiber–reinforced expansive soil. *Geotextiles and Geomembranes*, *46*(2), 183–189. https://doi.org/10.1016/j.geotexmem.2017.11.009

Sridharan, A., & Prakash, K. (1985). Improved Rectangular Hyperbola Method for the Determination of Coefficient of Consolidation. *Geotechnical Testing Journal*, *8*(1), 37. https://doi.org/10.1520/GTJ10855J

Sun, H., Scaringi, G., Mašín, D., & Najser, J. (2021). An experimental investigation on the swelling behavior of compacted B75 bentonite. *Engineering Geology*, 106452. https://doi.org/10.1016/j.enggeo.2021.106452

Takayama, Y., Tachibana, S., Iizuka, A., Kawai, K., & Kobayashi, I. (2017). Constitutive modeling for compacted bentonite buffer materials as unsaturated and saturated porous media. *Soils and Foundations*, *57*(1), 80–91. https://doi.org/10.1016/j.sandf.2017.01.006

U.S. Department of Energy. (2021, March 31). *3 Reasons Why Nuclear is Clean and Sustainable*. https://www.energy.gov/ne/articles/3-reasons-why-nuclear-clean-and-sustainable

U.S. Energy Information Administration. (2021). *What is the United States' share of world energy consumption?* https://www.eia.gov/tools/faqs/faq.php?id=87&t=1

U.S. Energy Information Administration. (2022, July 12). *Nuclear explained*. https://www.eia.gov/energyexplained/nuclear/data-and-statistics.php

U.S. Environmental Protection Agency. (2022a, February 5). *Global Greenhouse Gas Emissions Data*. https://www.epa.gov/ghgemissions/global-greenhouse-gas-emissions-data

U.S. Environmental Protection Agency. (2022b, May 16). *Overview of Greenhouse Gases*. https://www.epa.gov/ghgemissions/overview-greenhouse-gases

U.S. Environmental Protection Agency. (2022c, May 20). *What are the characteristics of Yucca Mountain?* https://www.epa.gov/radiation/what-are-characteristics-yucca-mountain

U.S. Environmental Protection Agency. (2022d, September 30). *What is the Yucca Mountain repository?* https://www.epa.gov/radiation/what-yucca-mountain-repository

U.S. Government Accountability Office. (2009). *Nuclear Waste Management - Key Attributes, Challenges, and Costs for the Yucca Mountain Repository and Two Potential Alternatives*.

U.S. Nuclear Regulatory Commission. (2020a, March 12). *High-Level Waste*. https://www.nrc.gov/waste/high-level-waste.html

U.S. Nuclear Regulatory Commission. (2020b, March 12). *Low-Level Waste*. https://www.nrc.gov/waste/low-level-waste.html

Vadlamudi, S., & Mishra, A. K. (2018). Consolidation Characteristics of Sand–Bentonite Mixtures and the Influence of Sand Particle Size. *Journal of Hazardous, Toxic, and Radioactive Waste*, *22*(4), 06018001. https://doi.org/10.1061/(asce)hz.2153-5515.0000409

van Olphen, H. (1977). *An Introduction to Clay Colloid Chemistry: For Clay Technologists, Geologists and Soil Scientists* (2nd ed.). Wiley-Interscience. https://doi.org/10.1002/jps.2600530238

Villar, M. V., Iglesias, R. J., & García-Siñeriz, J. L. (2020). State of the in situ Febex test (GTS, Switzerland) after 18 years: A heterogeneous bentonite barrier. *Environmental Geotechnics*, *7*(2), 147–159. https://doi.org/10.1680/JENGE.17.00093

Villar, M. V., & Lloret, A. (2008). Influence of dry density and water content on the swelling of a compacted bentonite. *Applied Clay Science*, *39*(1–2), 38–49. https://doi.org/10.1016/j.clay.2007.04.007

Villar, M. v, Martín, P. L., Bárcena, I., García-Siñeriz, J. L., Gómez-Espina, R., & Lloret, A. (2012). *Long-term experimental evidences of saturation of compacted bentonite under repository conditions*. https://doi.org/10.1016/j.enggeo.2012.08.004

Viswanadham, B. V. S., Phanikumar, B. R., & Mukherjee, R. v. (2009). Swelling behaviour of a geofiber-reinforced expansive soil. *Geotextiles and Geomembranes*, *27*(1), 73–76. https://doi.org/10.1016/j.geotexmem.2008.06.002

World Nuclear Association. (2021, May). *Storage and Disposal of Radioactive Waste*. https://world-nuclear.org/information-library/nuclear-fuel-cycle/nuclear-waste/storage-and-disposal-of-radioactive-waste.aspx

World Nuclear Association. (2022a). *Nuclear Energy and Climate Change*. https://world-nuclear.org/nuclear-essentials/how-can-nuclear-combat-climate-change.aspx

World Nuclear Association. (2022b, January). *Radioactive Waste Management*. https://world-nuclear.org/information-library/nuclear-fuel-cycle/nuclear-wastes/radioactive-waste-management.aspx

Yang, T., Knutsson, S., & Liu, X. (2016). Swelling Properties and Permeability of Expandable Clays of Potential use for Nuclear Waste Disposal. In *Journal of Earth Sciences and Geotechnical Engineering* (Vol. 6, Issue 2). online) Scienpress Ltd.

Ye, W. M., Wan, M., Chen, B., Chen, Y. G., Cui, Y. J., & Wang, J. (2013). Temperature effects on the swelling pressure and saturated hydraulic conductivity of the compacted GMZ01 bentonite. *Environmental Earth Sciences*, *68*(1), 281–288. https://doi.org/10.1007/S12665-012-1738-4/FIGURES/10

Yetimoglu, T., Inanir, M., & Inanir, O. E. (2005). A study on bearing capacity of randomly distributed fiber-reinforced sand fills overlying soft clay. *Geotextiles and Geomembranes*, *23*(2), 174–183. https://doi.org/10.1016/j.geotexmem.2004.09.004